Solution-Processing of Chalcogenide Nanoparticles and Thin Films for Photovoltaic Applications

Àlex Carreté

Solution-Processing of Chalcogenide Nanoparticles and Thin Films for Photovoltaic Applications

---

Thesis by

Àlex Carreté

In Partial Fulfillment of the Requirements for the Degree of Doctor of Philosophy

Supervisor

Prof. Dr. Andreu Cabot

Tutor

Prof. Dr. Albert Cornet

Doctoral Program in Nanoscience

Department of Electronics

University of Barcelona

II

Als meus pares, la meva germana i l'Àuria.

Contents

Abstract

Thin film solar cells based on direct band gap semiconductors have attracted much research during last decades. Thin film technologies are currently commercial and display record power conversion efficiencies up to 20% at the laboratory scale. However, typical direct band gap semiconductors, CdTe and $CuIn_{1-x}Ga_xS_2$ (CIGS), content scarce and/or toxic elements such as In, Ga or Cd. An alternative to these materials is Cu_2ZnSnS_4 (CZTS), formed by abundant and non toxic elements. CZTS is a quaternary p-type semiconductor which presents great absorption coefficient (> 10^4 cm^{-1}), has similar crystalline structure and optical properties to CIGS, and a suitable and tunable band gap (1.00-1.5 eV) by varying the S/Se ratio.

An interesting strategy to develop thin film solar cells is the solution processing. Solution based approaches are especially interesting for their potential low production costs and their easy scalability. Among different solution processing techniques, the spraying of nanocrystals or metal salts is an especially interesting approach. The easy scalability of spraying techniques to prepare large-area panels in a non vacuum atmosphere, which is translated in a significant reduction of the production costs, renders the spraying very attractive for industrial implantation. A pulsed spray deposition system, which was custom made and operates in open air, is here used to produce CIGS and CZTS films from colloidal CIGS and CZTS NPs.

This work is divided in 5 chapters. The 1st chapter is an introduction to the photovoltaic (PV) technology and in particular to thin film PV technology, with special focus to chalcopyrite CIGS and kesterite CZTS. In the 2nd chapter I review the work done towards solving one of the major challenges associated to NP-based PV technologies: the complexity to transform NPs into highly crystalline thin films by sintering processes. The 3rd chapter describes the experimental procedures used to prepare all the required materials and thin films and to fabricate solar cells. This chapter also describes the techniques used to characterize the morphological, compositional, structural and optoelectronical properties of the materials and films. Chapter 4 and 5 describe the work done regarding CIGS and CZTS

technologies, respectively. Both chapters describe: NP colloidal synthesis, ligand exchange strategies to remove organic carbon surrounding the NP, subsequent thin film deposition techniques used, thermal treatments performed and final hetero-junction formation and device completion. Chapter 5 also describes a scale up method to produce large quantities of NPs using a continuous flow reactor.

In summary, the goal of this thesis is to establish a non vacuum technology to produce CIGS and CZTS PV devices prepared by solution process of the absorber. Additionally, drawbacks involved in the solution processing of NP-based films, such as elimination of organic carbon present in NP and film crystallization are addressed.

Resum en Català

Avui en dia, la major part de la industria fotovoltaica està basada en el silici. Aquesta és una tecnologia provada i robusta, però, a causa de l'alt cost dels wafers de silici, el seu potencial de reducció de costos sembla limitat. Així, s'ha desenvolupat una segona generació de cel.les solars, formada per capes primes de semiconductors inorgànics, que gràcies al consum reduït de material semiconductor permet la fabricació de cel·les solars de baix cost. Els dispositius fotovoltaics de capa prima en base semiconductors de band gap directe han atret molta investigació en les últimes dècades. Les tecnologies de capa prima són actualment comercials i presenten eficiencies records de fins a 20%, a escala de laboratori. No obstant això, els semiconductors de banda prohibida directa, CdTe i CIGS, contenen elements tòxics i poc abundants, com In, Ga o Cd. Una excel.lent alternativa a aquests materials és el CZTS, ja que està format per elements no tòxics i abundants. El CZTS és un semiconductor quaternari de tipus p que presenta un gran coeficient d'absorció (> 10^4 cm^{-1}), mostra una estructura crital.lina i propietats òptiques similars al CIGS, i un band gap adequat i variable (1,00-1,5 eV) variant la relació S/Se, el que el converteix en un absorbidor adequat en cel.les solars de capa prima. Aquesta tesi explica el treball fet en la preparació i caracterització de capes primes de CIGS i CZTS mitjançant tècniques de processat en solució, utilitzant tintes de nanoparticules preparades prèviament mitjançant síntesis col·loïdal.

La síntesi col.loidal de nanopartícules requereix l'ús de lligands orgànics per controlar el seu creixement i facilitar la seva dispersabilitat. Aquests lligands orgànics són generalment cadenes hidrocarbonades alifàtiques, que tenen caràcter d'aïllant elèctric. La presència d'aquests lligands orgànics deteriora fortament les propietats electròniques de les capes obtingudes, i afecta el rendiment fotovoltaic del dispositiu. A més, la presència de carboni orgànic, el qual envolta el nanocristall, bloqueja el creixement de gra i consequentment cristalització via tractament tèrmic de capes primes nanoparticulades de CIGS i CZTS, pas estrictament necessari per obtenir dispositius amb comportament fotovoltaic. Per resoldre aquest problema, les cadenes llargues d'hidrocarburs es bescanvien per lligands inorgànics.

L'eficàcia de l'estratègia d'intercanvi de lligand per reduir el carboni orgànic present en els nanocristalls de CIGS i CZTS i la consequent millora de la cristalització es investigada.

D'altra banda, també està reportat que el creixement del gra en CIGS i CZTS pot ser afavorit gracies al dopatge amb Sb i Bi. Nanopartícules CIGS i CZTS poden ser dopats mitjançant la introducció de Sb o Bi mitjançant intercanvi de lligands de les cadenes alifàtiques llargues, usades per produir nanopartícules coloidals, per solucions inorgàniques de $SbCl_3$ o $BiCl_3$. Un intercanvi de lligand típic es realitza barrejant una solució de nanopartícules estabilitzades amb cloroform amb una solució d'agent lligand amb formamida, en una relació 2:1. La solució s'agita per obtenir una bifase, on les nanopartícules intercanviades es dirigeixen a la fase de formamida i els orgànics restants són arrossegats a la fase cloroform. La solució es netejada amb cloroform diverses vegades per eliminar tots els compostos orgànics units a les nanopartícules. Un cop purificada, es precipita per centrifugació i s'estabilitza amb un solvent polar com dimethyl formamide o dimethyl sulfoxide, per al seu posterior ús.

Tecnologies de buit i no buit s'utilitzen per produir pel.lícules primes de CIGS i CZTS. Els mètodes de deposició al buit com ara la deposició de polvorització catódica o co-evaporació, requereixen altes pressions de buit i altes temperatures per produir capes de CIGS i CZTS, el que es traduït en un alt cost de producció. El processat de solucions de nanopartícules representa múltiples avantatges, com el baix cost, major escalabilitat i alta taxa de producció. Entre les diferents tècniques de processament en solució, la polvorització per spray de nanopartícules o sals metàl.liques, ha estat utilitzada per diversos grups com una nova tècnica de deposició principalment per la seva simplicitat. Un sistema automatitzat de spray s'usa per a produir les pel.lícules de nanopartícules de CIGS i CZTS. L'ús del solvent apropiat per preparar la solució precursora, així com l'ajust dels diferents paràmetres de polvorització tals com la temperatura del substrat, el temps d'impuls de polvorització i el temps entre cada pols de polvorització, controlats per ordinador, permeten establir les condicions a obtenir la morfologia de la pel.lícula prima adequat i l'espessor desitjat. La configuració del sistema de polvorització consisteix en un spray controlat per ordinador utilitzant nitrogen com a gas portador i una placa calenta de temperatura controlada. La fàcil

escabilitat de tècniques de polvorització per preparar plafons de gran superfície en una atmosfera de no buit (o inert), significa una reducció significativa dels costos de producció, fa que la polvorització pre spray sigui una tècnica molt atractiva per a la implantació industrial.

Aquesta tesi presenta el treball realitzat en l'obtenció i caracteritzacio de cel·les solars de CIGS i CZTS. En la tesi es detallen les següents etapes:

1. Obtenció d'una solució de nanoparticules de CIGS i CZTS mitjançant síntesi col·loïdal. Les nanoparticules s'han caracteritzat mitjançant: Transmission electron microscopy, X-ray diffraction, Raman spectroscopy i scanning electron microscopy – energy dispersive X-ray spectroscopy.

2. Preparació de la tinta de CIGS i CZTS mitjançant les nanoparticules de CIGS i CZTS previament preparades. S'ha establert la composició de la tinta amb la qual obtenim capes sense defectes superficials i lliures d'esquerdes. La tinta es composa de les nanoparticules, el dispersant adequat.

3. Preparació de capes primes de CZTS i CIGS usant tècniques de processat en solució.

4. Seguidament, s'han establert els paràmetres per realitzar el correcte tractament tèrmic per tal d'obtenir un material cristal·lí. Hem determinat la temperatura, temps i condicions de tractament tèrmic. En aquesta etapa s'estableixen les condicions experimentals per tal d'obtenir capes de CIGS i CZTS de forma reproduïble i amb les propietats adequades per a muntar un dispositiu fotovoltaic. Les tecniques de X-ray diffraction, Raman spectroscopy i scanning electron microscopy – energy dispersive X-ray spectroscopy han estat usades per caracteritzar les capes.

5. Finalment un cop establertes les condicions per obtenir capes primes amb les propietats òptimes per al funcionament d'una cel.la fotovoltaica, es procedeix al montatge de la mateixa i a la mesura dels paràmetres fotovoltaics aixi com la seva eficiencia mitjançant simulador solar.

1 Introduction

1.1 Photovoltaic Technology

Humans have always used energy to obtain food, water and shelter. Finding, controlling and using energy has enabled mankind to progress and improve their quality of life. Therefore, energy is considered an indicator of social development and progress.

Energy sources are divided into two types, renewable and non-renewable. Non-renewable energy is mainly supplied by carbon-based fossil fuels: coal, oil and natural gas. Carbon-based fuels are finite energy sources and are associated to environmental degradation. Its use produces CO_2, CO, SO_2 and NO_x emissions, which have a negative effect on the environment. As an example, the global warming is caused by the rapidly increasing emissions of greenhouse gases such as CO_2. Also, SO_2 and NO_x are responsible for acid rain, which contaminate water and soil. Nuclear energy is also considered a non renewable energy source as uranium reserves are also finite. In addition, there is still no solution to safely store nuclear waste, which remains dangerous to life for thousands of years. On the other hand, renewable energies suppose an inexhaustible energy source as they can be regenerated naturally once consumed. Renewable energy sources include: hydropower, wind, geothermal, biomass and solar energy. Currently, most of the energy consumed is supplied by carbon-based fuels and only 10% of the total is supplied by renewable energies (figure 1). Nevertheless, if humanity is not able to exploit energy sources more efficiently, would be impossible to fulfill energy demand in the near future.

Among the main renewable energy sources, solar energy is considered a main candidate to partially replace conventional energy sources. An inexhaustible energy flow from the sun is available in most parts of the planet. This energy flow is so intense that only a few percent of the world's area would be needed to collect sunlight to fulfil electricity world demand Covering 0.16 % of the land of the earth with 10% efficient PV systems would produce 20 TW of power, which doubles fossil energy world consumption. [1,2]

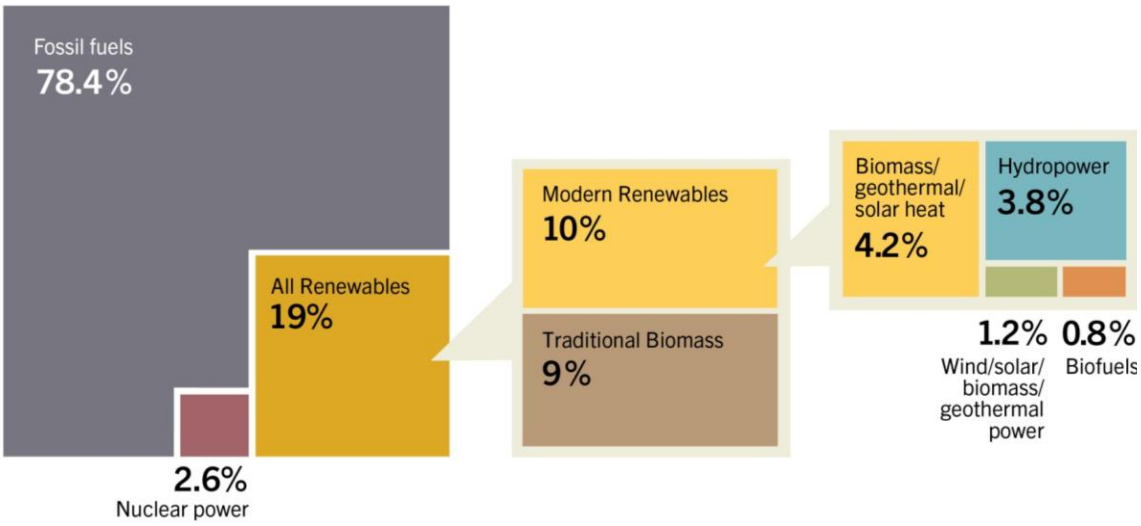

Figure 1. Estimated renewable enery share of global final enery consumption 2012 (Renewables 2014 global status report).

Solar energy has been the fastest growing energy sector in the last few years. The world's cumulative installed PV capacity has been increased from 4 to 139 GW since 2004. By regions, China has installed the largest PV plant connected to the grid with 11.8 GW in 2013, leading the world PV market last year. However, Europe and particularly Germany, is still the leading region in terms of cumulative installed capacity, with 81.5 GW. [3] During the next years, the PV market is expected to grow in south East-Asian regions, and South-America along with India.

1.1.1 Thin film Photovoltaic Technology

Silicon has been and still is the main material used in the PV industry. [4,5] However, because of its indirect band gap and related low absorption coefficient, thicknesses on the order of 100 μm are required to adequately absorb the sun light. Therefore, large grained and a high purity Si is needed to reduce recombination of the generated charge carriers, and thus to have long enough carrier lifetimes and diffusion lengths to generate photocurrent. These requirements are translated in high production costs. To overcome the inherent problems of Si, alternative thin film technologies based on direct band gap semiconductors have been developed in the last thirty years. [6] Second generation thin film devices are based on p-n heterojunctions of direct band gap absorber materials. As a result, they present very

high light absorption coefficients and require much thinner films to collect the same amount of light. Therefore, ultra-high purity materials are no mandatory and a certain degree of crystalline imperfections are accepted. In addition, a wide range of vacuum and non vacuum procedures can be used to produce thin films, which can be deposited in different types of substrates as glass or flexible metallic sheets. Those advantages lead to an easy and flexible module production and a drastical reduction of the production costs. However its efficiency is still slightly lower when compared with silicon. Figure 2 illustrates the evolution of the different PV technologies in terms of efficiency.

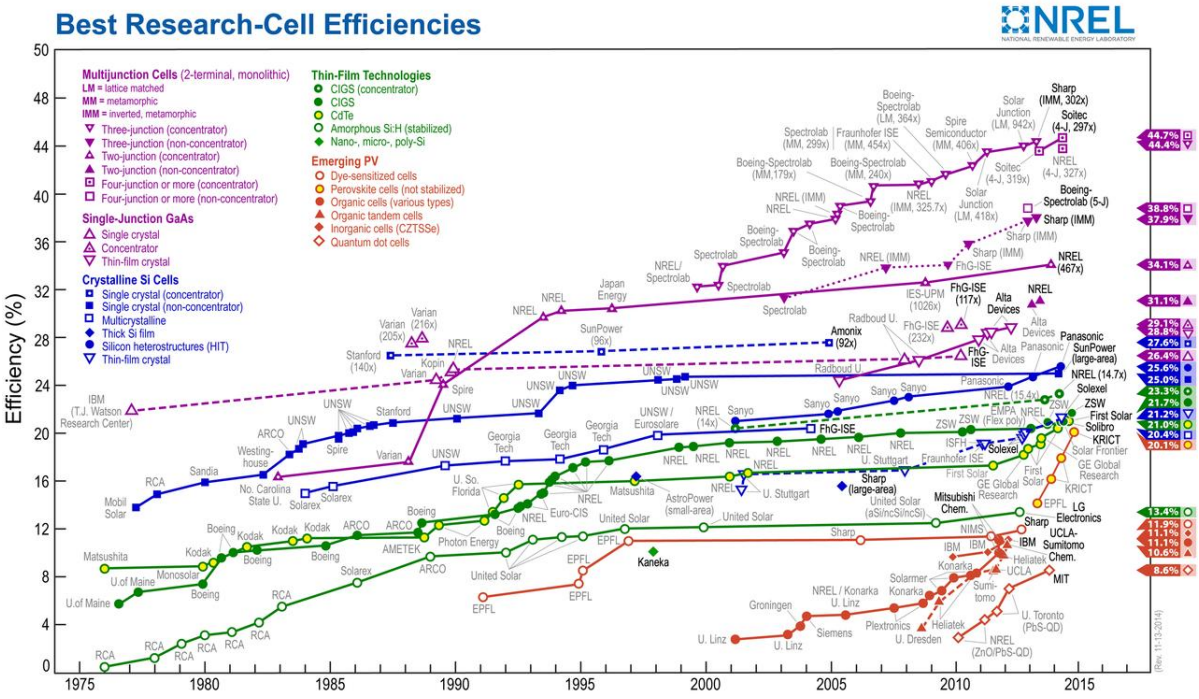

Figure 2. Efficiency evolution of best laboratory research cells by technology type.

CdTe and CIGS p-type semiconductors have been devised as the most promising absorber materials for thin film solar cells, presenting record laboratory scale efficiencies up to 19.6 and 20.5% respectively. [7,8,9] However these materials use toxic, expensive and scarce elements such as Cd, Te and Ga, which is against the idea to produce clean energy, using clean materials and processes. In recent years, alternative chalcogenide, Cu_2ZnSnS_4 (CZTS), made of abundant and non-toxic elements have attracted a great interest to replace CIGS and CdTe, made of abundant and non toxic elements.

1.1.2 Principle of Operation of Photovoltaic Solar Cells

PV technology is based on semiconductor devices, which convert solar irradiance into electricity. Charge carriers are generated in the material by absorbing photons, separated in the p-n junction and driven towards the contacts. Figure 3 depicts a p-n junction scheme.

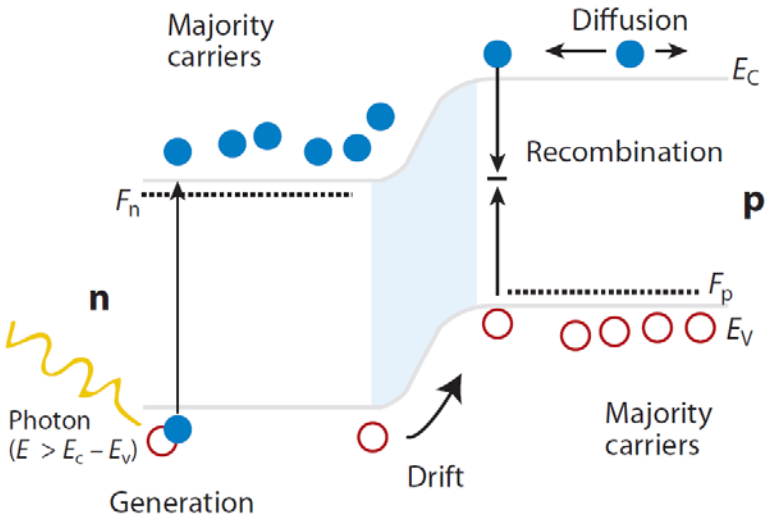

Figure 3. P-N junction scheme. A photon strikes the semiconductor creating free electrons (blue circles) and holes (red circles), which diffuse across the junction. [10]

The absorption of photons by the semiconductor is the first step to generate electricity. A photon can be absorbed, reflected or transmitted through the cell. Only if the photon is absorbed by the semiconductor, an electron is excited from the valence to the conduction band. For this, the energy of the photon should be equal or larger than the materials band gap. If the energy of the photon is larger, the excess of energy is lost as thermal energy.

In the second step the photo-generated electron-hole pairs are separated. Inorganic solar cells operate upon the establishment of an electric potential difference between the n and p-type regions. The generated electric field in the p-n junction acts as a driving force for the separation of photo-generated electron-hole pairs. The electric field favours the migration of the created electrons from the p region to the n region, and opposes its migration from the n region to the p region. This causes the movement of minority charge carriers across the

junction. As a result, electrical potential difference will be developed between its two ends and electrical current will flow through the solar cell. [7,11,12]

The solar cell conversion efficiency, describes the relation of the solar energy converted into electricity. The efficiency is defined as:

$$\eta = \frac{V_{oc} \times J_{sc} \times FF}{P_L}$$

The open circuit voltage (V_{oc}) is the potential difference obtained when the resistance of the load is infinite. The short circuit current (J_{sc}) is the electrical current flowing in the circuit when the load resistance is zero. The fill factor (FF) is the ratio between the theoretical maximal obtainable power and the measured maximum power. Finally, P_L is the power of the simulated light, used to make the measurement. Figure 4 shows a typical solar cell I-V curve, with the main 3 PV characteristic parameters: V_{oc}, J_{sc} and FF.

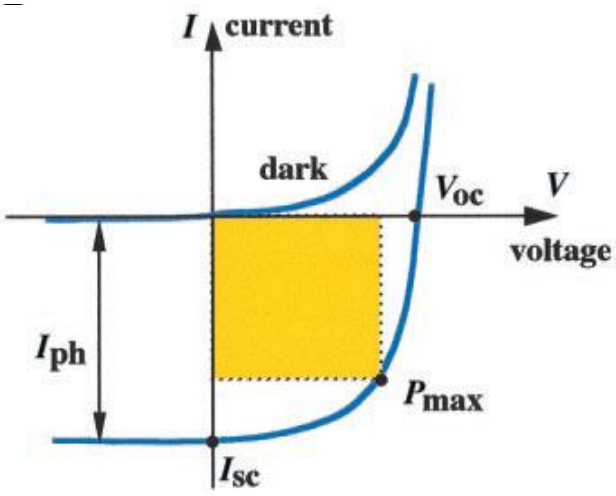

Figure 4. Shematic of a typical solar cell I-V curve, depicting PV parameters: V_{oc}, J_{sc}, FF and P_{max} which corresponds to the electrical power at the maximum power point. [4]

1.2 Thin Film Solar Cell Structure

The usual configuration of CIGS and CZTS thin film solar cells is the substrate architecture. The main advantage of the substrate configuration is the possibility to grow the absorber at

high temperature without damaging the p-n junction. The subsequent film formation is easily achieved by different processes at low temperature. A review of the principal elements in CIGS and CZTS solar cells is given as follows:

Substrate: The best-studied substrate is soda lime glass (SLG). It was originally used because of its low cost and thermal stability. Moreover, the substrate should not be damaged while exposed to the different aggressive processing environments. Particularly, to Se or S vapors at high temperature during the absorber formation and in the chemical bath used for buffer deposition. In addition, it should not release impurities that may deteriorate the electronic properties of the cell. However, it is known that Na diffusion from the substrate promotes grain growth of the absorber layer and passivates grain boundaries (GBs) which is beneficial for a good PV performance. [13]

Back contact: An 800 nm Mo layer is typically used as back contact. Mo has suitable electrical properties and relatively inert nature. However, when the Mo back contact is under a reactive environment, such as the S/Se rich atmosphere needed to obtain large grained chalcogenide absorber layers, a very thin layer of $Mo(S/Se)_2$ on top of the Mo film is created. [14] The $Mo(S/Se)_2$ layer provides a better energy band alignment, forming the necessary ohmic contact with low resistance needed to improve the electrical contact. [15] Additionally, the $Mo(S/Se)_2$ film improves the adherence. [16]

Absorber layer: This is the layer where incident light is absorbed resulting in the excitation of electrons. The absorber formation is based on delivery of the constituting elements by vacuum or non vacuum techniques, followed by high temperature treatment resulting in crystalline material. CIGS and CZTS are used in this work as p-type absorbers.

Buffer layer: CdS is the most common n-type semiconductor used to create the electronic hetero-junction in CIGS and CZTS solar cells. CdS has a bandgap Eg = 2.47 eV. It is important to prepare the CdS layer without pinholes and as thin as possible to reduce light absorption within the window (10-60 nm). Pinholes in CdS lead to regions in which the photo generated current can return to the junction instead of going to the external circuit. This limits the open circuit voltage and the performance of the solar cell. Thus the accurate control of

thickness and uniformity of the CdS layer is a critical challenge to produce good quality solar cells. In high efficiency CIGS and CZTS solar cells, the CdS layer is formed by chemical bath deposition (CBD) onto the absorber surface. [17,18]

Transparent conductive front contact: Finally a front contact is deposited on top of the CdS film, by low temperature deposition processes. The TCO has to comply electrical and optical requirements. From electrical point of view it has to be sufficiently conductive in order to reduce efficiency losses and provide ohmic contact to the buffer layer, in order to collect the charge of the whole device. From optical point of view it must be highly transparent to allow maximum illumination of the active layers. CIGS and CZTS cells usually use an aluminum-doped ZnO (AZO) layer as TCO. Indium doped tin oxide (ITO) or Sn_2O:F are also used.

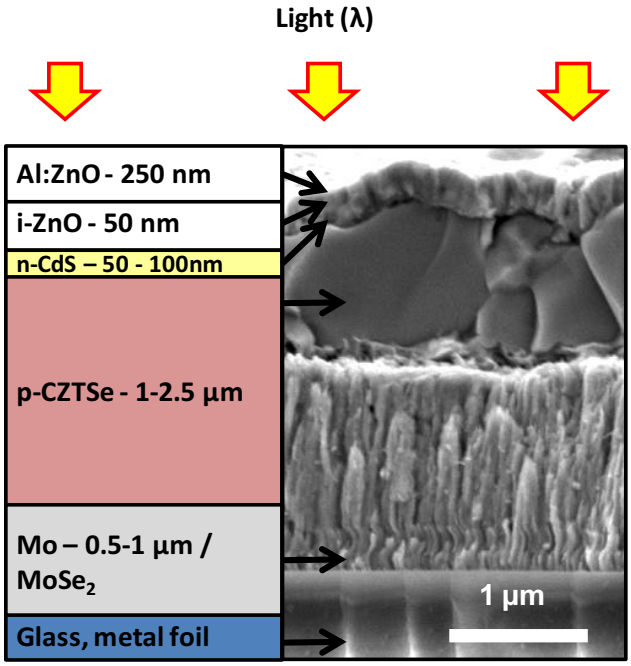

Figure 5. Cross- section SEM image of a $Cu_2ZnSnSe_4$ (CZTSe) solar cell, composed of a Mo back contact, CZTSe absorber, CdS buffer and TCO.

1.2.1 CIGS Solar Cells

CIGS is a suitable PV material to be used in p-n hetero-junctions thin film solar cells. This is due to its high absorption coefficient and its direct and tuneable band gap. Moreover, the material stability, the long operational lifetimes and the structural tolerance to significant

stoichometric variations make CIGS an interesting material for industrial implementation. 20 % power performance efficiencies have been reported for CIGS thin film solar cells, in which the absorber layer is prepared by vacuum processing techniques. Nevertheless, these techniques are not exactly low cost due to the complex processing and the low material yield. In this regard, non-vacuum deposition techniques or non-vacuum processed materials are essential to reduce the production costs.

CIGS band gap can be shifted by replacing In by Ga, in the range from 1 ($CuInSe_2$) to 1.7 eV ($CuGaSe_2$). [19] An intermediate quaternary composition with a ratio [Ga]/[In+Ga]=0.3 leads to an optimal band gap (1.4eV), with the best match with the incident solar light spectrum. [20]

In terms of crystal structure, CIS and CIGS, I-III-VI_2 semiconductors, are known as chalcopyrites. The ABX_2 chalcopyrite derives from the zinc-blende crystal structure, in which both cations, A and B, are tetrahedrically coordinated with 4 anions, X. [21] However, sometimes, near stoichometry CIGS is present in other stable phases such as sphalerite, in which Cu and In cations are randomly located, forming a cubic unit cell (figure 6). [22]

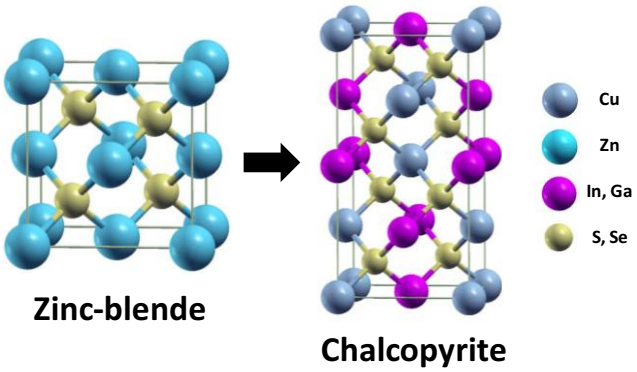

Figure 6. Chalcopyrite crystal structure derived from zinc-blende structure. [23]

Within CIGS, acceptor defects have lower formation energy than donor defects, what explains the p-type conductivity of CIGS. [24] Copper vacancies (V_{Cu}) and indium-copper antisites (In_{Cu}), are the main acceptor and donor defects present in chalcopyrite CIGS. High PV quality CIGS films are prepared with a deliberated Cu poor surface, forming a stable ordered vacancy or ordered defect compound (OVC/ODC). The OVC surface is n-type doped;

with which a buried pn-junction is formed with the p-type CIGS bulk film. The created inverted surface minimizes the recombination at the CIGS/CdS interface. [25]

1.2.2 CZTS solar cells

CZTS is a quaternary chalcogenide semiconductor which shows p-type conductivity, an absorption coefficient larger than $1x10^{-4}$ cm^{-1} and a 1.45 eV band gap. Also, is free of scarce and toxic elements and presents similar structural, electrical and optical properties to CIGS, which makes it a good candidate to replace conventional CIGS thin film solar cells. In 1997, the first CZTS solar cell efficiency was reported, with a V_{oc} of 400 mv and a 0.66 % PV efficiency. [26] However, not until more recently, CZTS has been recognized to be a suitable material in thin film solar cells. Recent material improvements lead to increased efficiencies, up to 12.6 % at the laboratory scale. [17]

In order to maximize the device efficiency, the optimization of the chalcogenide band gap is needed. [27] The CZTS band gap can be adjusted by partially replacing S by Se in the range from 1 eV (CZTS) to 1.5 eV (CZTSe). [28,29,30] The band gap can be also tuned by partially replacing Sn by Ge. [31]

CZTS and CZTSe have been reported to crystallize in kesterite or stannite structure. The difference between kesterite and stannite lies in a different distribution in the cation sub-lattice. [32] First-principle calculations by Chen et al. suggested that kesterite should be more stable than the stannite structure. [23] Ternary compounds, I-III-VI_2, adopt chalcopyrite structure, in which group VI atoms are surrounded by two group I and two III atoms, thus obeying the octet rule. As seen in figure 7, when the group III cation is replaced by II and IV pairs in ternary chalcogenides, chalcopyrite I-III-VI_2 mutates exclusively into the kesterite I_2-II-IV-VI_4 configuration. Moreover, CZTS, ZnS and Cu_2SnS_3 and its corresponding selenides, have similar lattice constant making them indistinguishable by diffraction methods. Raman spectroscopy is a powerful characterization technique which is able to identify secondary phases, such as Cu_xS, ZnS, Sn_xS, Cu_2SnS_3, and Cu_3SnS_4. [33] Consequently, Raman spectroscopy is usually combined with X-ray diffraction (XRD) measurements in order to identify the presence of binary and ternary phases along with the quaternary kesterite. [34,35]

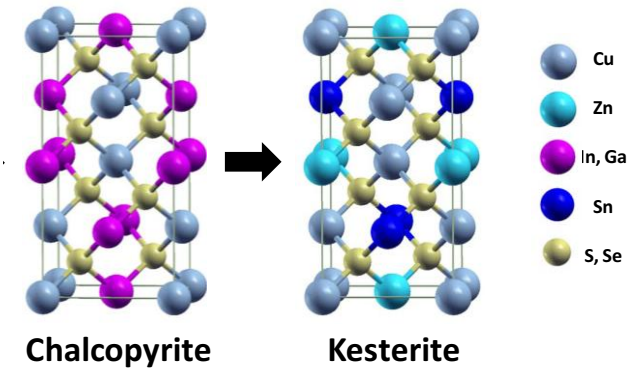

Figure 7. Kesterite crystal structure derived from Chalcopyrite. [23]

CZTS presents different kinds of intrinsic defects that appear during its growth. Those defects are vacancies of Cu, Zn, Sn and S, antisite defects and interstitial defects of Cu, Zn and Sn. The formation energy of acceptor defects is lower than the donor defects ones, which makes CZTS an intrinsic p-type semiconductor. P-type conductivity is consequence of the CuZn antisite defect, confirming that CZTS absorber layers should be Cu poor and Zn rich to obtain high efficiency solar cells. [36]

1.3 Solution Processed Chalcogenide Thin Film Solar Cell

As consequence to the similarity between CIGS and CZTS materials, the know-how of CIGS PV production had been transferred for the research and further industrial implementation of CZTS based solar cells. Consequently, over the past few years, vacuum technologies to produce high quality CZTS PV devices, such as thermal evaporation or sputtering have been widely investigated. [37,38,39,40] Those technologies are associated to the sequential deposition of individual metal layer followed by an annealing step in S or Se rich atmosphere. Vacuum deposition technologies are energy intensive technologies as a result of the required high vacuum and high temperature processes. Therefore, the research community has been searching alternative non-vacuum technologies capable to produce large scale CZTS PV devices by simpler and cheaper processes. [41] However most non-vacuum processes also require high temperature annealing steps to prepare highly pure and crystalline CZTS thin film. [42] Thermal treatments around 500℃ induce chemical and physical

reactions to remove non-desired secondary phase, favors the densification and induce grain growth.

Non-vacuum technologies can be divided into two main groups: Electro-deposition and ink based approaches. On the one hand, electro-deposition is a widely studied and industrially established technology. [43,44] Additionally, wide research on chalcogenide electro-deposition have lead to high efficiency PV solar cells, 7%. [45,46] The main drawback of this technology is the difficulty to deposit multi-component materials, due to the different redox potential of each element. On the other hand, ink based approaches are based on film deposition from solvent dispersions. A first step involves the formulation of a stable precursor ink with a proper concentration and viscosity. The precursor ink would be used for thin film deposition by doctor blade, spin coating, printing or spraying. [47,48,49] A subsequent drying step is needed in order to remove the organic compound previously added. [50] The resulting film has to be crack free and homogeneous enough for the further thermal treatment. Critical stresses could take place in this step contributing to the film cracking. Consequently, the solvent for the ink formulation should be well selected to prepare films free of surface defects. [51]

Ink based approaches are divided into molecular/ionic and NP based approaches. Molecular and ionic approaches are based on inks prepared by mixing metal salts with a proper organic binder or solvent. [52] NP approaches are based on the use of NPs for ink formulation. Additionally, NP-based technologies, gives us the possibility to prepare precursor chalcogenide NPs with the desired composition and crystal phase. [53,54,55] Also, NPs allow an easy ink formulation with a wide range of solvents. [56] Figure 8 depicts an overview of NP-ink solar cell fabrication. The solution-synthesis of NPs requires the use of organic ligands to control their growth and facilitate their dispersability. [57] These organic ligands are usually long aliphatic hydro-carbonated chains. The presence of these organic ligands, which have an electrical insulating character, strongly deteriorates the electronic properties of the obtained layers, decisively affecting the performance of the device. To solve this problem, the exchanging of the long hydrocarbon chains by inorganic ligands has been recently proposed. [58,59,60]

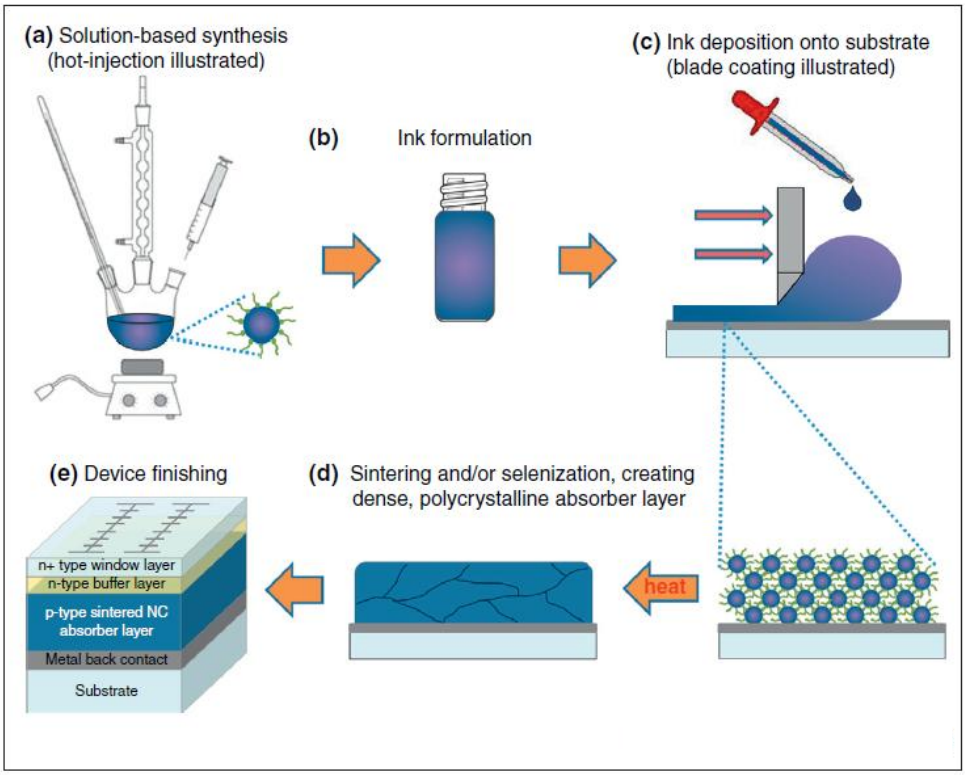

Figure 8. Schematic of sintered NP-ink solar cell fabrication: a) NP colloidal synthesis, b) NPs ink formulation in a proper solvent, c) Inks are deposited onto a metal-coated substrate, d) As-deposited NP films are thermally treated in a chalcogen atmosphere to form a dense crystalline absorber layer, e) The device is finished by depositing an n-type buffer layer followed by a window layer and the conductive top contacts. [61]

As mentioned before, due to the poor crystallinity of the as prepared ink based films, a thermal treatment is necessary in order to induce a proper crystal growth and improve the layer crystallinity. The difficulty to induce grain growth by sintering of NPs is a main issue to be addressed for NP implementation in PV applications. That topic will be discussed in the next chapter, trying to clarify the phenomena occurring during grain growth of NPs, and also identifying different grain growth strategies.

2 Grain Growth of Solution Processed Thin Films

2.1 Grain Growth of Nanocrystalline Materials

Control over the grain growth is of paramount technological importance not only on the field of PV but in several other applications due to the strong dependence that material performance has on the grain size. On one hand, small grain sizes provide strength and toughness, which is useful for structural materials as for example on nanocrystalline cemented tungsten carbide used for tools in the metalworking, drilling, and mining industries. [62] On the other hand, as noticed previously, large grained materials are required to improve PV performance of thin film solar cells. The reason to convert nanosize grains into large grains is that the large-grained absorber enhances efficiency of thin film solar cells by suppressing non-radiative centers, with which charge carriers recombine without releasing photons. This process lowers the light generation efficiency and increase heat losses. In this regard, to understand and control grain growth, kinetic and thermodynamic paths as wells as possible grain growth mechanisms is of paramount importance for improving the final PV performance. In this chapter different mechanism and approaches to control grain growth are summarized.

General speaking, grain growth is the term used to describe the increase in the average grain size in a nanocrystalline material (figure 1). On this regard, is important to note that a nanocrystalline material is formed by a grained structure in which the internal surfaces of adjacent grains are in contact by grain boundaries (GBs). Those GBs have higher energy than the bulk crystal and, hence, a reduction in the GB area will reduce the free energy of the system. Therefore, as grain size increases, the number of grains per volume decreases and thus the total area of GB and consequently the GB energy, resulting in a more stable material.

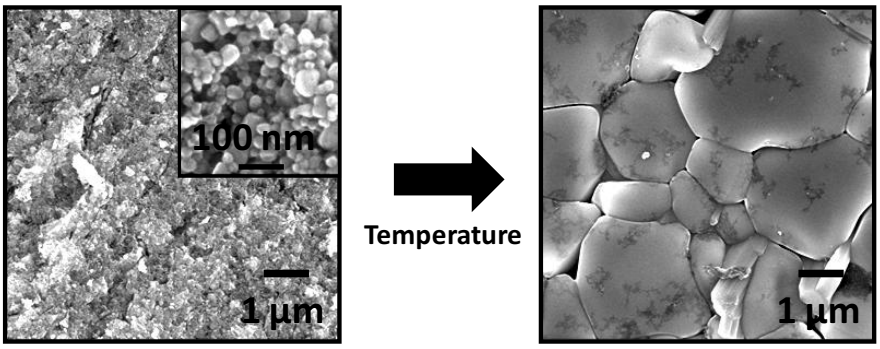

Figure 1. Grain growth of colloidal NPs is observed after sintering them at elevated temperatures. The number of GBs is reduced to form a more stable material.

To exemplify grain growth we can illustrate an array of regular hexagons which is the only stable arrangement in a two-dimensional grain structure and which fulfill both the space-filling and boundary tension equilibrium requirements. Any other arrangement would lead to grain growth. As sketched in figure 2, if a 5-sided polygon is introduced then it must be balanced by the surrounding 7-sided polygons in order to maintain the average number of edges per grain at 6.

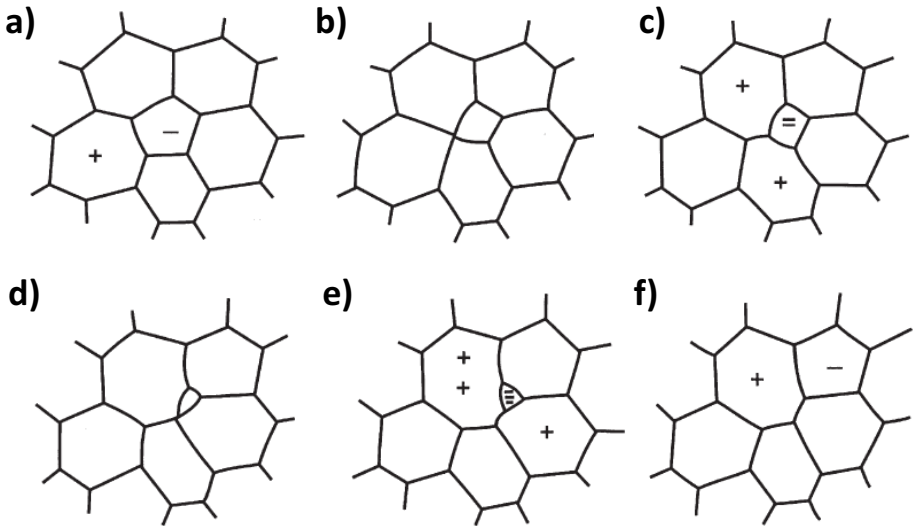

Figure 2. Schematic view of a grain growth process by introducing a polygon with less than 6 sides into a stable the structure (a). The 5-sided grain is consumed by the surrounding grains to maintain the maintain the average number of edges per grain. [63]

In addition, as grains present curved surfaces, atoms on the concave sides are more completely surrounded by atoms of their own crystal than atoms on the convex side. Thermal motion causes atoms at the curved interface to move continuously from one surface to the other and since they are more stable on the concave side, there is a net flow of atoms to this surface. Consequently, the boundary will migrate towards it center of curvature under a pressure due to surface curvature (figure 3).

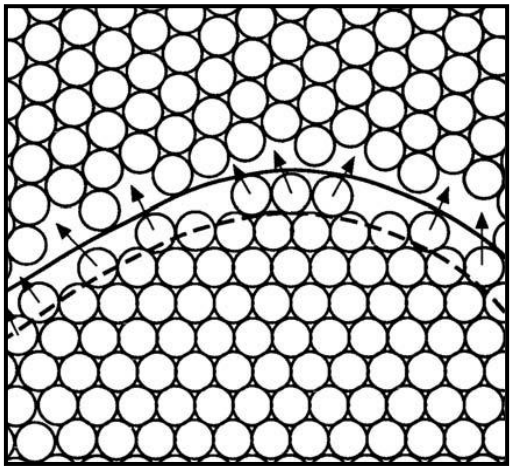

Figure 3. Classical picture of a grain boundary. The boundary migrates from the convex side of the boundary to the concave side. [64]

Finally, is possible to divide grain growth in two types; normal grain growth and abnormal grain growth. Normal grain growth is a continuous process in which the grains coarsen uniformly. The range of shape and grain sizes can be quite narrow as shown in figure 4a with a grain size distribution independent of the sintering time. After a specific growth time, the microstructure reaches a stable state showing a homogeneous grain size distribution. In some special circumstances, the microstructure can become unstable leading to the so-called abnormal grain growth or exaggerated grain growth. [63] Abnormal grain growth originates from a preferential growth of some crystallographic orientation or grains with respect less favored adjacent grains. As a result, large grains grow rapidly and uncontrolled in a matrix of fine grains (figure 4b) leading to a bimodal distribution microstructure (figure 5). [65]

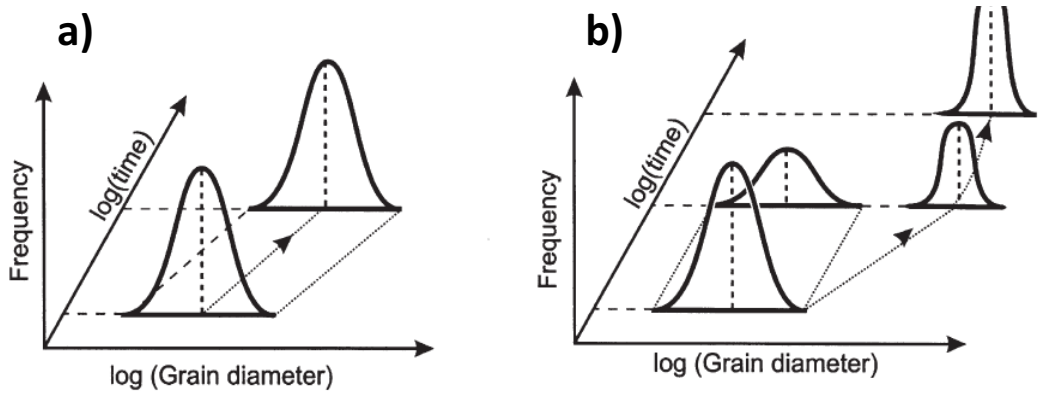

Figure 4. Schematic representation of the change in grain size distribution during (a) normal grain growth and (b) abnormal grain growth. [63]

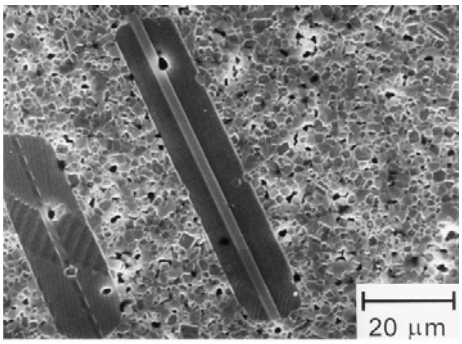

Figure 5. SEM image showing abnormal grain growth. 0.1 mol % TiO_2 excess $BaTiO_3$ sintered at 1250℃ for 10h under air. [66]

2.1.1 Grain Growth Kinetics

Burke and Turnbull, established that the driving force for grain growth was essentially the surface energy of the GBs, which impelled the boundaries to migrate towards their respective centers of curvature. [67] On this regard, they deduced a parabolic relationship for grain growth kinetics,

$$G^m = G_0^m + kt \qquad (1)$$

where G^m is the grain size at time t, G_0^m is the grain size at $t = 0$, and k is a temperature dependent rate constant. The rate constant is related to the intrinsic mobility of the boundary, M_b, by

$$k = 2\alpha M_b \gamma_{gb} \quad (2)$$

where α is a constant that depends on the shape of the grains and γ_{gb} is the GB energy. Furthermore, the mobility is related to the diffusion coefficient for the atoms across the boundary,D_a, by

$$M_b = \frac{D_a}{kt}\left(\frac{\Omega}{\delta_{gb}}\right) \quad (3)$$

where k is the Boltzmann constant, T is the temperature, Ω is the atomic volume and δ_{gb} is the GB thickness.

Therefore, according to equations 1, 2 and 3, the grain growth rate depend on the amount of GB energy as well as their mobility, M_b, which is enlarged with increased diffusivity.

2.2 Grain Growth Inhibition

To achieve full densification in sintered materials while keeping nanoscale grain sizes is of paramount importance in several industrial applications. The control of grain growth as a consequence of GB migration is in consequence required. For this purpose approaches such as *second phase inclusions*, *two step sintering process* and pressure assisted processes have been proposed. The latter including *transformation assisted consolidation*, *sinter-forging* and *spark plasma sintering* (SPS). [68,69,70,71]

The most effective approach for inhibiting grain growth involves the use of additives, second phase particles, which are incorporated into the material to form a solid solution. The presence of these second phase particles in the GB hampers grain growth by inducing a drag force of the particle opposed to the movement the GBs (figure 6). From a thermodynamic point of view, the drag force is the result of the reduction of the total GB energy, observed by GB occupation of second phase particles. [68,69,70] This phenomenon is known as the Zener pinning effect. [72,73]

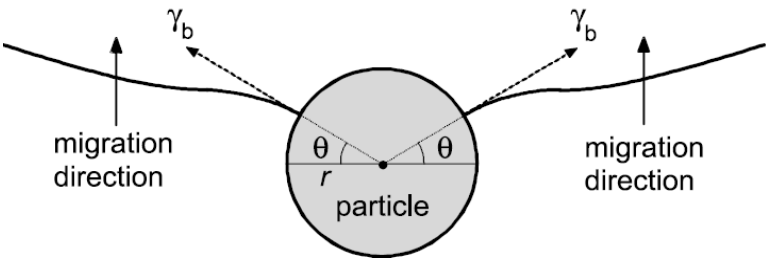

Figure 6. Schematic of the Zener effect. Dragging of GB movement by second phase particles. [65]

Other techniques such as pressure assisted processes are also used to inhibit grain growth. Applied pressure inhibits grain growth by decreasing the diffusivity and GB mobility. [74] As a consequence of the applied pressure densification is achieved at lower temperatures than usual sintering processes. As a result of the lower temperature used, the grain growth kinetic rate is also reduced. Some examples of different pressure assisted processes are listed below:

Transformation Assisted Consolidation: Several materials such as oxide-ceramic powders show a grain size reduction after consolidation under high pressure as a consequence of a phase transformation. As an example, nanosized TiO_2 is transformed from anatase to rutile phase after consolidation under pressures higher than 1GPa. [75] The precursor material should be in a metastable phase which is later transformed to the desired stable phase by sintering under pressure. During compaction and sintering, nucleation of stable phases occurs in competition to grain growth processes which are translated in an enhanced density and a negligible grain growth. Nucleation events are controlled by lowering the temperatures and increasing pressures leads to a decrease of the diffusion and an increase of the nucleation respectively.

Sinter-Forging: This technique is based on the simultaneous deformation of a porous ceramic and densification at elevated temperature under the action of a uniaxial stress. This procedure has been widely used to prepare materials such as nanocrystalline yttria-partially-stabilized zirconia (3Y-TZP) or nanophase TiO_2 while maintaining grain sizes. [76,77,78]

Spark Plasma Sintering: This technique is based on the sintering of metals and ceramics by using plasma on an electric discharge machine while a hydrostatic pressure is applied. The

spark plasma is created by a pulsed direct current during the heat treatment of the powders in a graphite die. [79] SPS has been successfully applied to produce nanocrystalline materials such as Cu_2SnSe_3 for thermoelectric applications. [80] The material is processed into a pellet by SPS to minimize grain growth. Figure 7 shows SEM images of Cu_2SnSe_3 pellets prepared by SPS at different temperatures. A minimal increase of the crystal domain size from the original 12 nm to 15 nm, 25 nm and 30 nm was observed after SPS at 400, 500 and 600℃ respectively confirming the suitability of this technique.

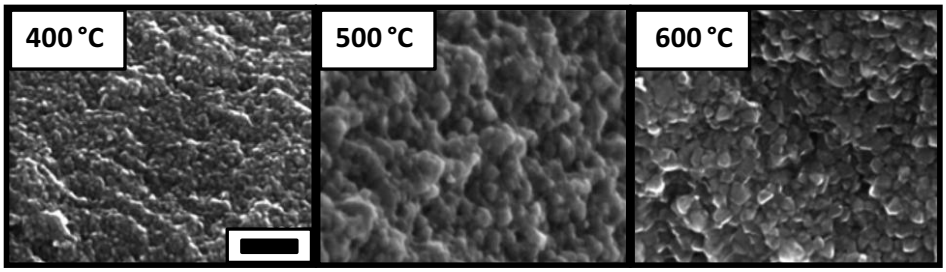

Figure 7. SEM images from nanocrystalline Cu_2SnSe_3 pellets prepared by SPS at 400, 500 and 600℃ (scale bar 200 nm). [80]

2.3 Grain Growth Promotion

Although the fabrication of semiconducting NP can be a facile, scalable, and relatively low-energy process, direct application of nanomaterials to PV systems has traditionally delivered poor device performance. Electrical properties of inorganic NP absorber layers can be significantly decreased by sintering the NP film at elevated temperatures, thus obtaining large grained films.[59,81,82,83] The ability to achieve high-quality large-grain absorbers is a key step in solar cell fabrication from NP precursors as this morphological feature is common to high-efficiency thin-film devices. Several strategies can be used to promote grain growth: phase transformation, chalcogen exchange, external doping, metal induced crystallization (MIC) or grain growth induced by reaction of heterogeneous precursors. In this chapter, the mechanisms behind the different grain growth reported methods are summarized.

2.3.1 Grain Growth Induced by Phase Transformation

The normal driving force for grain growth is a reduction in GB area, but, in some cases, we can have an additional contribution from the difference in free energy between stable

and metastable structural phases (*i.e*. diamond, wurtzite, …). Energy needs to be supplied to the system to induce the transformation from the meta to the ground state. For instance, thermal energy will induce this transformation with a further energy release. The coexistence of two different phases which presumably present different GB surfaces will increase the GB energy and the GB diffusivity consequently promoting the grain growth. As the grain size of the stable phase is increased, the GB diffusivity is diminished as a result of the GB area reduction leading to the grain growth completion. Figure 8 sketches an illustration of this mechanism.

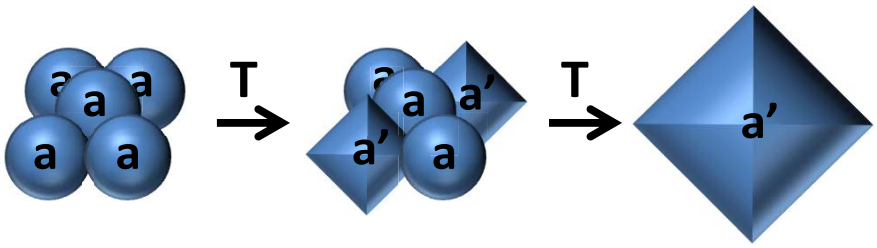

Figure 8. Illustration showing a grain growth event by phase transformation in which *a* phase is converted to *a'* by a high temperature sintering. The coexistence of the two phases is accompanied with an increased GB diffusivity inducing the grain growth.

As an example, Mainz et al. proposed a mechanism to obtain large grained semiconductor films from metastable CZTS nanorods induced by phase transition. [84] The colloidal synthesis reported aims to produce wurtzite phase CZTS nanorods, identified as an unstable phase in bulk, which subsequently leads to a low energy barrier for its fast conversion to bulk kesterite phase. The mechanism can be explained by the progress of two processes: First, a nucleation step which comprises the transition from wurtizte to kesterite NPs, and second, the grain growth of NPs into large crystals. Both processes have to take place simultaneously in order to obtain the desired large grained CZTS kesterite film. The convergence of these two steps can be accomplished by using fast heating rates which would also equal the respective activation energies. In contrary, a slow heating rate leads into different nucleation/transition and grain growth rates and the respective activation energies (E grain growth < E nucleation). Consequently, wurtzite would convert to kesterite before grain growth, obtaining smaller grain sizes. Figure 9 shows cross-sectional SEM

images and XRD of precursor wurtzite CZTS and large grained kesterite CZTS thin films after annealing at relatively low temperature (400℃).

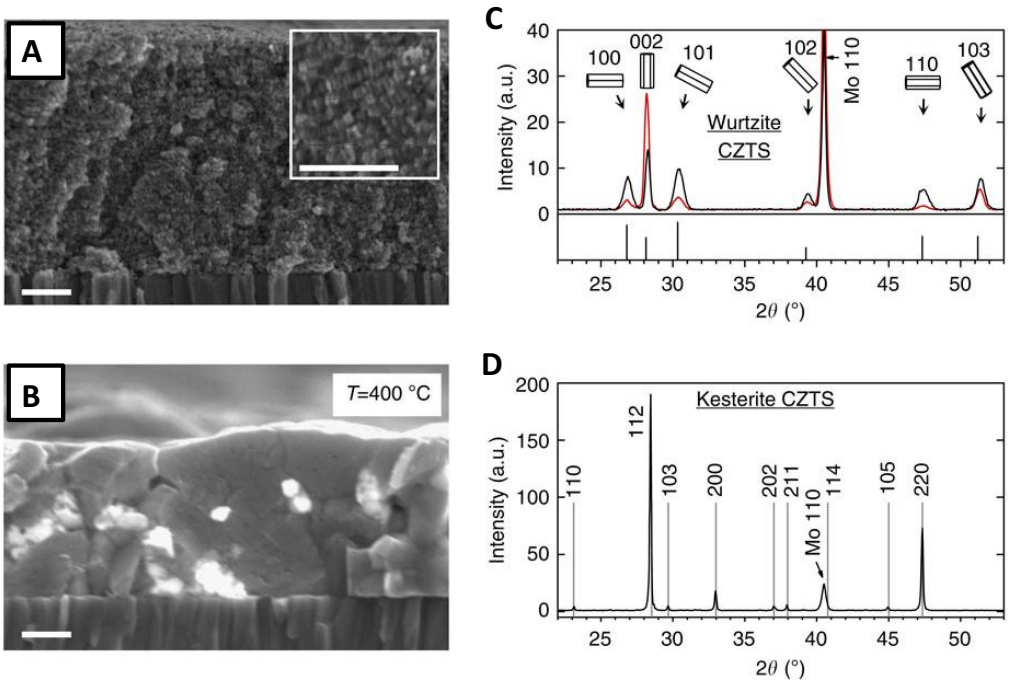

Figure 9. SEM cross-sectional images of precursor wurtzite CZTS thin film (A) and the obtained kesterite CZTS thin film after annealing at 400℃ (B) (scale bars, 200nm). XRD of wurtzite (C) and kesterite (D) CZTS thin films. [84]

2.3.2 Grain Growth Induced by Ion Exchange

Another pathway to induce grain growth in semiconductor thin films is by ion diffusion. This phenomenon is observed by treating the semiconductor under high temperatures and reactive atmospheres. The ions diffuse to the GB forming intermediate phases and thus increasing the GB diffusivity and consequently promoting grain growth (figure 10). Grains with different GB energy surfaces tend to react and grow in order to reduce the GB surface energy.

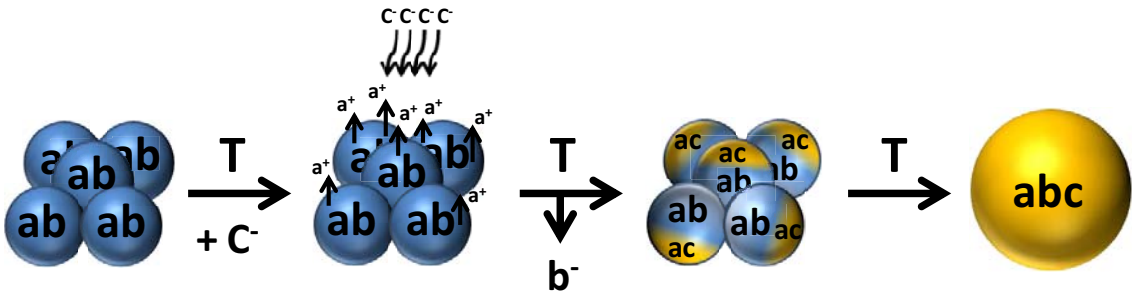

Figure 10. Illustration showing the typical grain growth by ion diffusion. The cations, a^+, diffuses from the grain to the GB by reacting with the anions, c^-. The formed intermediate compound, *ac*, increases the GB diffusivity and thus the grain growth.

For instance, a chalcogen exchange during sintering is a common strategy to induce NP grain growth by ion diffusion in CIGS and CZTS thin films.[31,42,49,85,86] Samples are sintered under reactive Se atmosphere and high temperatures. Large grained CZTSe and $CuIn_{1-x}Ga_xSe_2$ (CIGSe) films are obtained by selenizing nanocrystalline CZTS and CIGS precursors (figure 11). Moreover, the replacement of S by Se in the CIGS and CZTS matrix creates a volume expansion, which in turn reduces void spaces leading to high crystalline and densified CIGSe and CZTSe films. A further selenization of selenium precursors (CIGSe or CZTSe) or sulfurization of selenide or sulfide precursors will not underwent a volume increase and consequently leading to low quality thin films.

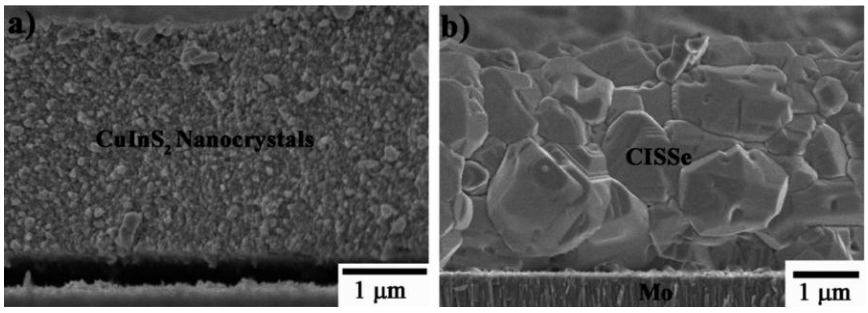

Figure 11. SEM cross-sectional images of CIS thin film before and after selenization at 500℃ for 45 min. [87]

A detailed description of the mechanism is the following: For instance, for the selenization of CZTS thin films, Cu^+ from the NPs diffuse to the surface to form large grains of CuSe as Se is incorporated into the film. Afterwards, Sn and then Zn start to incorporate to the initial CuSe grains, forming the final large grained CZTSe film (figure 12). [88]

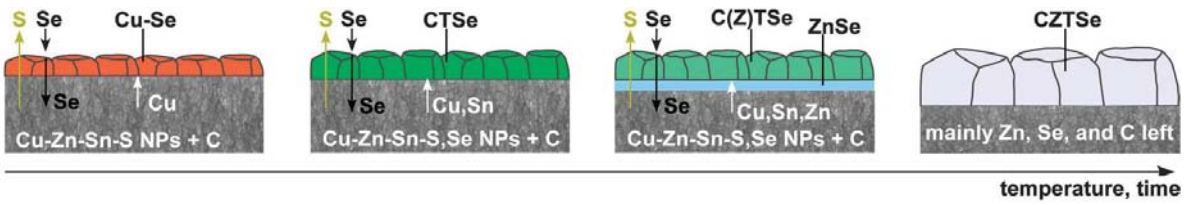

Figure 12. Schematic of CZTS thin film selenization in which Cu^{+} diffuses to the surface forming CuSe. Afterwards, Zn and Sn are incorporated to the initial CuSe to form the final large grained CZTSe thin film [88]

2.3.3 Grain Growth Induced by External Doping

The incorporation of external impurities, such as Sb, Bi, Na, K and Cs, has also been reported as effective grain growth doping agents for CIGS and CZTS solution processed thin films. [89,90,91,92] As a general idea, the incorporation of impurities to the crystal structure locally reduce the materials melting point, increasing its ionic mobility and its capacity for mass transfer and reorganization which promotes the grain growth process. (figure 13). Although the mechanism which leads to a grain growth can follow different pathways the final result is the same. In all these cases, a chalcogen exchange and/or a corresponding phase transition take place to complete the sintering. As an example, two different strategies with different mechanism are discussed below.

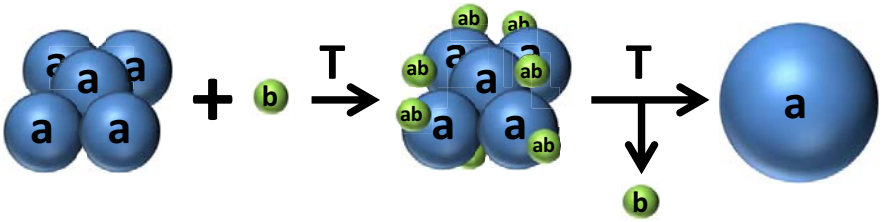

Figure 13. Illustration showing grain growth by external doping. The external agent, *b*, reacts with *a*, forming and intermediate compound which increases the GB diffusivity and hence the grain growth.

As a first example, grain growth in CIGS and CZTS thin films is increased with the presence of Na during selenization. Na could be supplied by diffusion from the glass substrate or by the incorporation of additional Na on chalcogenide thin films prepared by different techniques. Extra Na could be added by soaking chalcogenide film in a NaCl solution, depositing layers of NaF over the chalcogenide layer or by the direct incorporation of Na

impurities in precursor inks by using solution processed techniques. The Na-chalcogenide reaction mechanism proceeds as follows: In a first step, elemental Se provided by Se vapors react with the supplied Na forming polyselenide phases of Na_2Se_X around the crystal grains which subsequently act as a Se source. On a second step, these polyselenide phases react with the metal cations of CIGS or CZTS promoting the grain growth and crystallization of CIGSe or CZTSe. [93] Figure 14 show a schematic view of the mechanism involving the selenization of a CIS film in the presence of Na impurities.

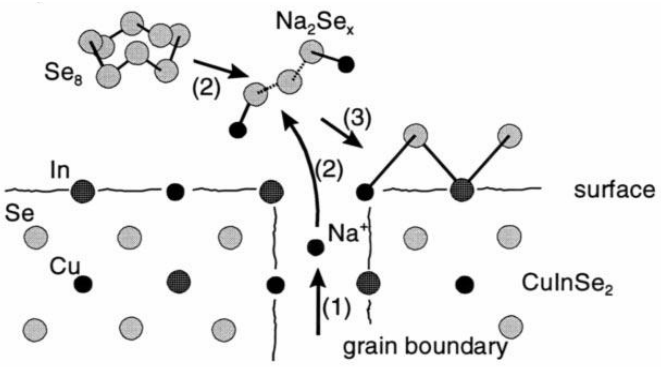

Figure 14. Schematic view of the mechanism involving the growth and oxidation of CIS in the presence of Na. a) CIS growth: 1) diffusion of Na ions from GB to film surface, 2) breaking of Se rings into chains and Na_2Se_x formation, 3) Na_2Se_x acts as the selenium source during grain growth. [93]

In Na-doped CIGS the layer of Na_2Se_X around CIGS grain crystallites acts as catalyst by supplying more Se than in Na free samples and thus leading to a more efficient selenization. [94] Under high Se and Na conditions, CISe is formed by the reaction of Cu_2S and InSe, which has been reported to obtain large crystallites as a consequence of preferential crystallographic mechanisms. [94] As shown in figure 15, Na doped CIGSe films present better crystallinity and morphology than Na free chalcogenide films.

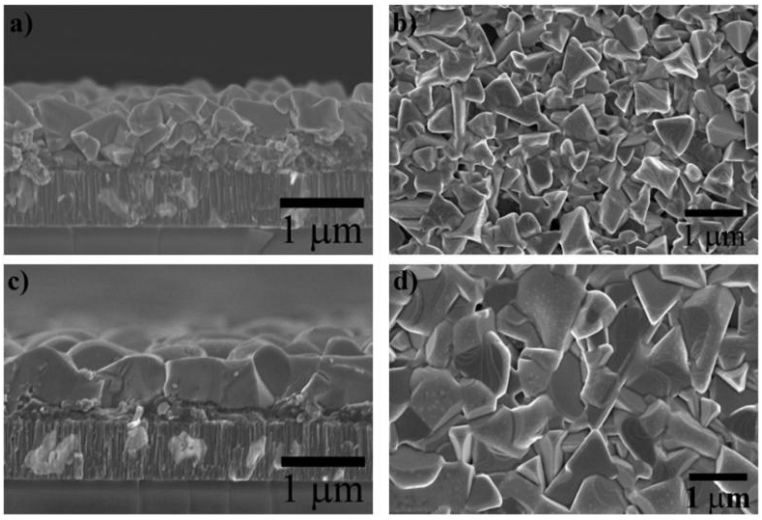

Figure 15. Cross-sectional and top SEM images of selenized at 500℃, Na free and Na doped CIGS thin films, a), b) and c), d) respectively. [94]

Another strategy implies the reaction of Sb impurities with CIGS NPs to further obtain large grained single phase chalcopyrite thin films. [95] The suggested mechanism is explained by the reaction of Cu precursor with Sb and Se to form the intermediate phases responsible of the improved grain growth to further react with In and Ga precursor and produce CIGSe. Moreover, Cu_2Se and Cu_3SbSe_3 are produced by the reaction of $CuCl_2$ and Se in the presence of $SbCl_3$. Cu_3SbSe_3 is a mobile phase at high temperatures, 200℃, in which Cu cations are delocalized. As a consequence of the mass transfer, highly reactive Cu^+ cations react with In and Ga precursor to produce chalcopyrite CIGSe films. The remaining Sb-Se species react with Cu_2Se to produce more Cu_3SbSe_3, which acts as a Cu^+ cations source for further CIGSe production. Without Sb presence, Cu_2Se follows a kinetically less favorable reaction with In and Ga precursor to form CIGSe (figure 16). By presenting a favorable kinetic pathway with the introduction of Sb impurities the reaction time for CIGSe sintering is reduced from 48 to 12 hours. The reaction is also accompanied by a decreased annealing temperature to produce highly crystalline CIGSe films (figure 17). The incorporation of only 1,2% mol of Sb is necessary to dope and reduce sintering temperature to 400℃. [90]

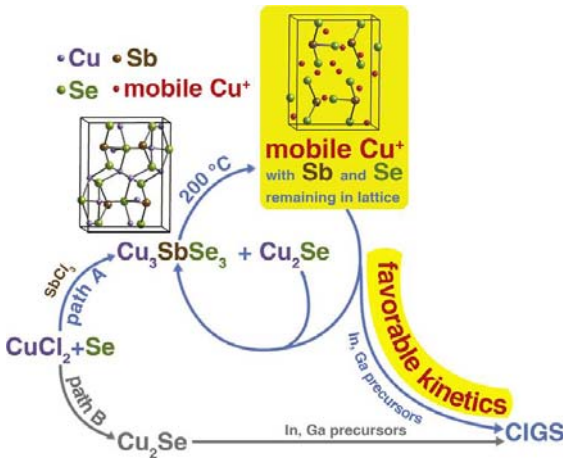

Figure 16. Suggested mechanism of Sb-doped CIGSe production by the reaction of Cu_2Se with In and Ga precursors. [95]

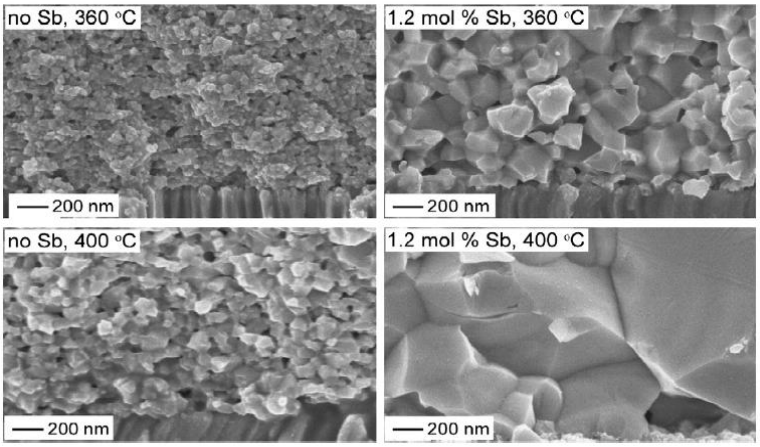

Figure 17. Cross-sectional SEM images of Sb-doped and un-doped CIGSe films selenized under different annealing temperatures. [90]

2.3.4 Grain Growth Induced by Metallic Films

Before discussing this strategy, it is important to underline that this procedure can be understand as a two step process involving a recrystalization process and a further grain growth starting amorphous phase. For instance MIC is widely used in amorphous semiconductors such as Si or Ge which can be crystallized by the interaction with a metal (*i.e.* Al or Ni). The interaction along the interface between the free electrons from the metal film and the semiconductor covalent bonds from the amorphous semiconductor is rather weak. This effect promotes the diffusion of the semiconductor atoms into the metal film and

vice versa. As a consequence, nucleation of semiconductor crystals takes place in the metallic matrix. Semiconductor grains surrounded by a metal matrix show high GB surface, thus high GB diffusivity leading to a grain growth. Particularly, MIC is a crystallization process for semiconductor thin film device fabrication used to increase grain size and also to reduce annealing temperature and time. There are 3 main MIC mechanisms namely: layer exchange mechanism, diffusion assisted crystallization and metal induced lateral crystallization which are described below.

As an example, the layer exchange mechanism involves the formation of polycrystalline Si films by eutectic forming metals. A layer exchange between the amorphous silicon (a-Si) and metal takes place during the transformation from a-Si to polycrystalline Si. As an example, Si nuclei can be formed in an Al/a-Si interface, which subsequently grow inside the Al layer until adjacent Si grains join together forming the polycrystalline Si (figure 18). [96]

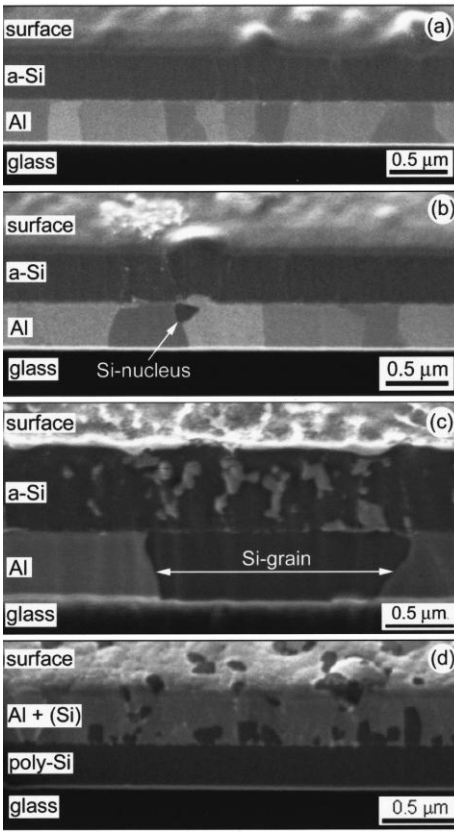

Figure 18. Cross-section Focused Ion Beam images of the *a*-Si/Al/glass structure. before annealing a), and after annealing at 500℃ for 5 min b), 10 min c), and 60 min d). [96]

2.3.5 Grain Growth Induced by Reaction of Heterogeneous Precursors

Large grained semiconductor thin films can also be obtained by the reaction of NPs with inorganic ligands or molecular compounds, but the reaction different types of NPs lead to a grain growth too (Figure 19). [97,98] Indeed, the use of different precursor materials show beneficial sintering effects by providing a large interface area which results in faster diffusion of atoms or ions and thus high ion mobility under high sinter temperatures. [99] This method has shown to be very efficient for the preparation of NPs thin films for electronic application. For instance, the use of inorganic ligands instead of the isolating organic ones leads to a burst on the conductivity. Below, the different approaches will be discussed along with some example.

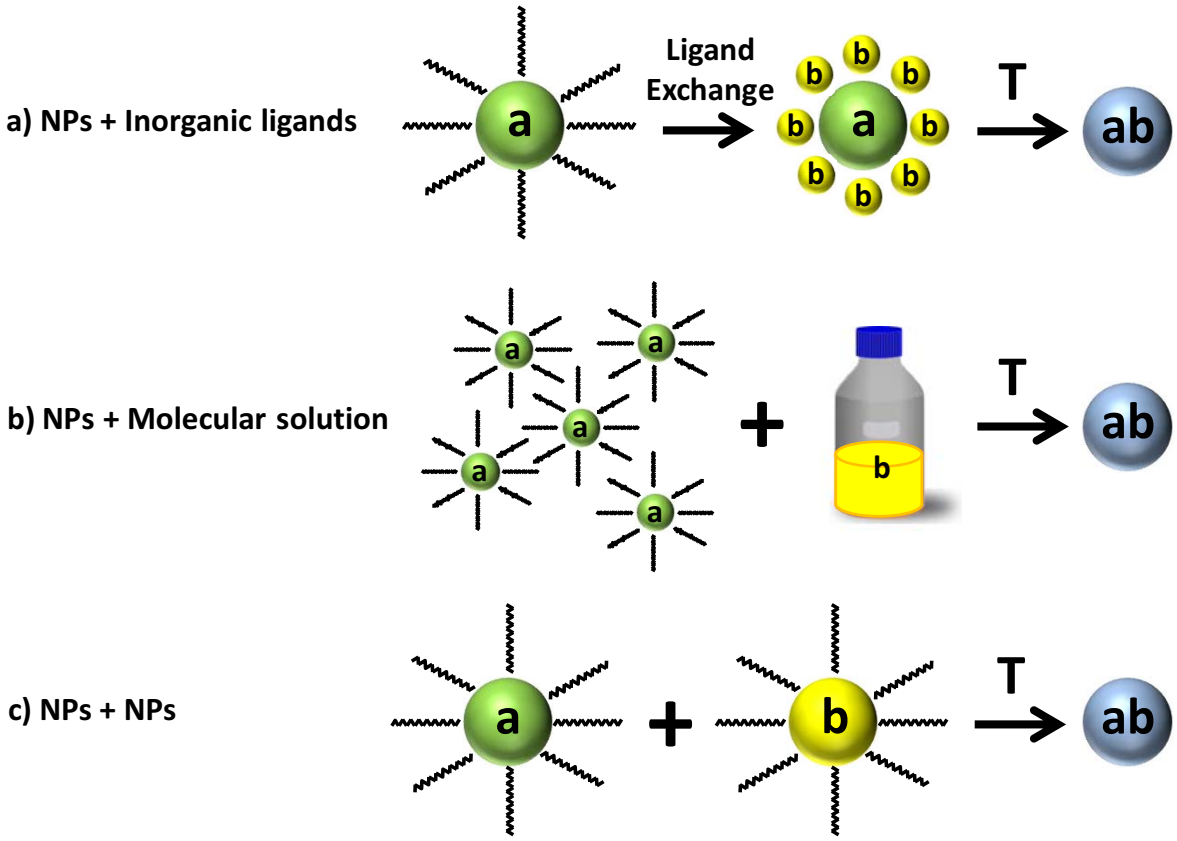

Figure 19. Illustration of the possible chemical transformation by mixing NPs with inorganic ligands (a), molecular solutions (b) and other NPs.

Reaction between NPs and inorganic ligands (figure 19a): As an example of the first case, large grained CIG(S,Se) thin films can be obtained by the reaction of colloidal $Cu_{2-x}Se$-OLA

NPs with $In_2Se_4^{2-}$ molecular metal chalcogenide (MMC) surface ligands, which are introduced by ligand exchange of initial OLA ligands (figure 20). [100] Different MMC surface ligands can be prepared and introduced in binary or ternary NPs permitting further chemical transformations to produce pure CIS, CIGS and CZTS phases. [101]

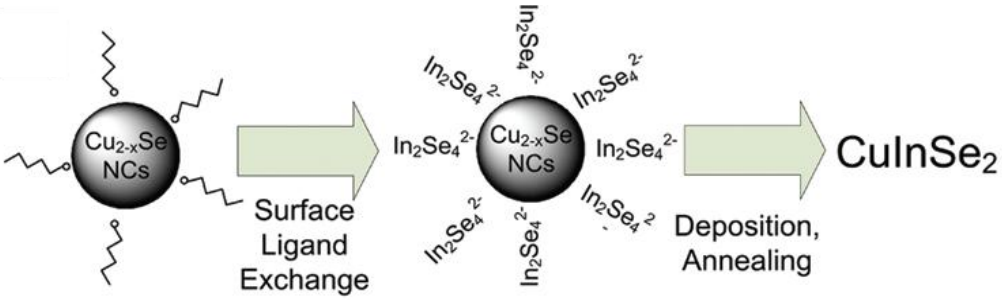

Figure 20. Schematic route to process CISe by reaction of $Cu_{2-x}Se$ NP with $In_2Se_4^{2-}$ capping ligands. [100]

Reaction between NPs and molecular solutions (figure 19b): The reaction of NPs with molecular precursors has been widely used to prepare large grained chalcogenide semiconductors. As an example, NP induced grain growth for $CI(S,Se)_2$ has been reported as a suitable method by incorporating CuS and In_2S_3 NPs to an aqueous CIS precursor. In this case, Cu rich NPs act as nucleation centers promoting an enhanced grain growth. [102] A similar approach combine in a proper ratio, Cu_2S and $SnSe_2$ hydrazine solutions with $ZnSe(N_2H_4)$ or $ZnS(N_2H_4)$ NP to form into single phase and high crystalline CZT(S,Se). [30]

Reaction between heterogeneous NPs (figure 19c): CIG(S,Se) and CZT(S,Se) large grained thin films can also be obtained by mixing three NPs containing the desired elements. For instance: CTS, ZnS and SnS or Cu_xS_y, ZnS and SnS. [97] A suitable driving force for sintering through mass transport is achieved through heterogeneities in the pre-sintered material.[99] The final film composition of the film can be easily tuned by adjusting the ratios between the precursors. [98] A similar approach relies on the addition of an extra element. Studies have been reported that Cu-rich CIGS nanocrystalline thin films present better grain growth during sintering. In this regard, Walker et al. reported a grain growth enhancement by mixing CuSe NPs to CIGSe NPs as precursor. [103] In both cases, the further sintering under selenium or inert atmosphere at high temperatures lead to well crystallized CZTSe and CIGSe films.

2.4 Conclusions

Since grain growth affects the functional and mechanical properties associated to the material microstructure, it becomes an important issue in materials science and engineering which has to be well understood in order to make a fully controlled design and engineering of materials. On this regard, grain growth mechanisms and kinetic models have been described in this chapter.

Additionally, different grain growth inhibition mechanisms and strategies to induce grain growth during sintering of NPs have been explained in this chapter. On one hand, several applications need to sinter precursor nanomaterials in order to obtain densified and maintaining nanometer scale while on the other hand large grained polycrystalline materials is a key step to prepare PV devices presenting suitable opto-electronic properties.

3 Methods and Techniques

This chapter describes the experimental procedures to prepare the materials and films and to fabricate the devices in chapters 4 and 5: NPs colloidal synthesis, flow production of CZTS NPs, NP ligand exchange, thin film deposition techniques, annealing treatments and solar cell device fabrication. Additionally, characterization techniques used to study compositional, structural and morphological properties of NPs and thin films, as well as the equipment used to test solar cell devices is explained here.

3.1 Colloidal Synthesis

Colloidal synthesis routes are used here to produce CIGS and CZTS NPs. Those NPs would be further used as building blocks to prepare thin films. A typical colloidal synthesis to produce NP involves three components: precursors, organic surfactants and solvents. In some systems, surfactant can act as solvent. Colloidal NPs are formed by a two step mechanism. First, the precursors chemically transform to active molecular species, monomers. When heating the mixture to an adequately high temperature, NPs nucleate. Later the formed nuclei "seed" would grow by incorporating remaining monomers. (figure 1).

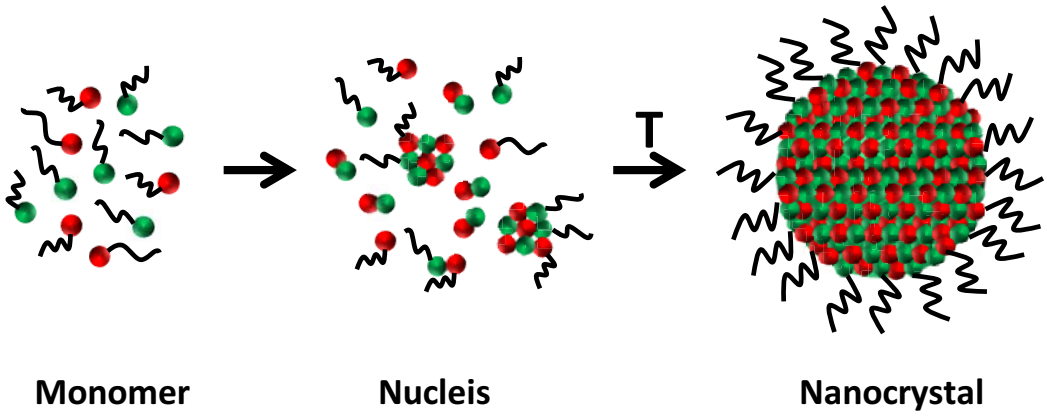

Figure 1. Schematic of NP formation from precursor upon high temperature reaction.

In order to obtain NPs with narrow size distribution, nucleation and growth kinetics need to be balanced. Nucleation must occur on a short time scale. This equilibrium is obtained by

selecting the proper chemical reagents and by using optimized reaction conditions, such as reaction temperature and growth time. The separation of nucleation and growth events is also possible by the hot-injection method. In this method, the rapid incorporation of reagents to the reaction system raises the precursor concentration above the nucleation threshold. Consequently a short nucleation would relieve the supersaturation. The temperature would drop down, allowing growth of NPs at lower temperatures (figure 2). Following this synthetic route, all NPs experience a single nucleation event and consequently would equally grow, consuming all available monomers. This results in highly monodisperse colloidal NPs. Furthermore, if NP growth continues, secondary growth by Oswald ripening can take place. Smaller particles dissolve and incorporate to larger particles, which eventually saturate the system. Consequently, the average NP size is increased with growth time.

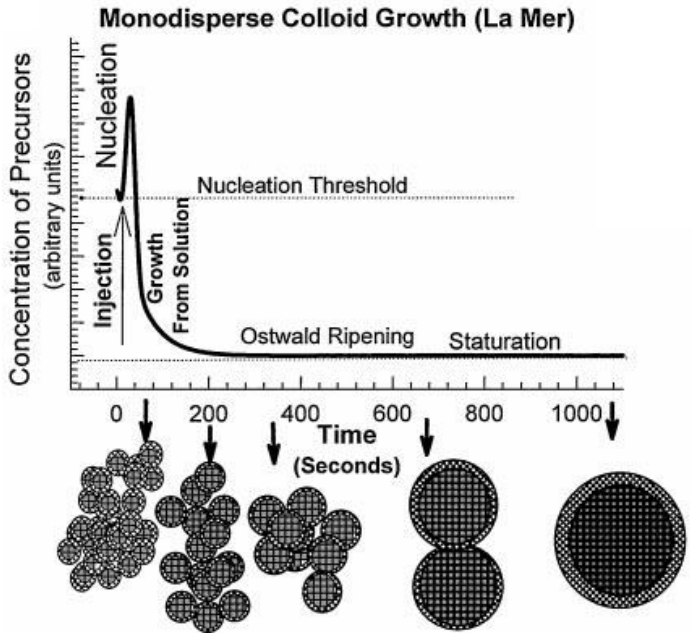

Figure 2. Scheme depicting the stages of nucleation and growth for the preparation of monodisperse NPs following La Mer model. [104]

Colloidal NP growth is directed by the organic surfactant molecules, which adhere to the growing NP. Organic surfactant are formed by a long hydrocarbon chain and a coordinating functional group, which bonds to NP surface preventing further growth and aggregation, and consequently slowing NP growth kinetics. Additionally, NP shape can be modulated by

selective adhesion of surfactant molecules to different crystal facets. Surfactant molecules can bind to particular facets, suppressing their growth by preventing monomer incorporation to these surfaces.

An important step of the synthesis is the NP purification. Non-reacted monomers and free ligand molecules need to be removed. The final properties of the NP depend on the purification, thus it is a critical step for the further use of the NPs. There are different techniques for NP purification: electrophoresis, magnetic separation, centrifugation and selective precipitation. The most common method is the precipitation/dissolution technique. This method consists in the introduction of a nonsolvent which is miscible with the original dispersing solvent but destabilizes the NP dispersions due to the unfavorable interaction with the nonsolvent with the organic ligands. The NPs precipitates leaving non-reacted by-products in solution. The obtained powder is re-dispersible in different solvents. Repeated precipitation and re-dispersion in fresh solvents complete the purification.

3.1.1 CIGS Nanocrystal Colloidal Synthesis

The CIGS NPs used in chapter 4 were obtained by mixing $Cu(acac)_2$ (1 mmol), $In(acac)_3$ (0.75 mmol), $Ga(acac)_3$ (0.25 mmol), trioctylphosphine oxide (TOPO 3.35 mmol) and oleylamine (OLA, 10 ml) under argon in a three neck flask connected to a Schlenk line. The mixture was kept under vacuum for 30 min at room temperature to purify it from low boiling point impurities. Afterward, temperature was increased to 155 ºC and 1-dodecanethiol (DDT, 7.7 mmol) was injected. The solution was maintained at this temperature for 15 min. Then temperature was raised to 270 ºC, and NP were allowed to grow for 30 min. CIGS NPs were finally purified by multiple precipitation and re-dispersion steps using a mixture of toluene and ethanol in a ratio 2:1 for precipitation and toluene for re-dispersion. Figure 4 shows a schematic of a colloidal synthesis and the CIGS NP synthesis thermal profile.

Ligand exchange was performed in the CIGS NP from chapter 4. 100 mg of CIGS NP were dispersed in 10 ml of chloroform and mixed at room temperature with 5 ml solutions of 1 M $BiCl_3$ in formamide, 1 M $SbCl_3$ in formamide and a 10 ml solution of formamide containing 1 ml of $(NH_4)_2S$ (20 wt % in water). The solution was shacked to displace the organic ligands

attached to the NP surface during 1 minute. A bi-phase solution was obtained, where the organic chains were retained into the chloroform phase, while the NPs tend to go to the formamide solution, containing the new ligand agent. NPs were purified by cycles of chloroform/formamide to drag and remove all the remaining organic compounds. After removing the chloroform phase, containing OLA groups, the solution was precipitated by centrifugation and subsequently re-dispersed in polar solvents like dimethyl formamide (DMF) or dimethyl sulfoxide (DMSO).

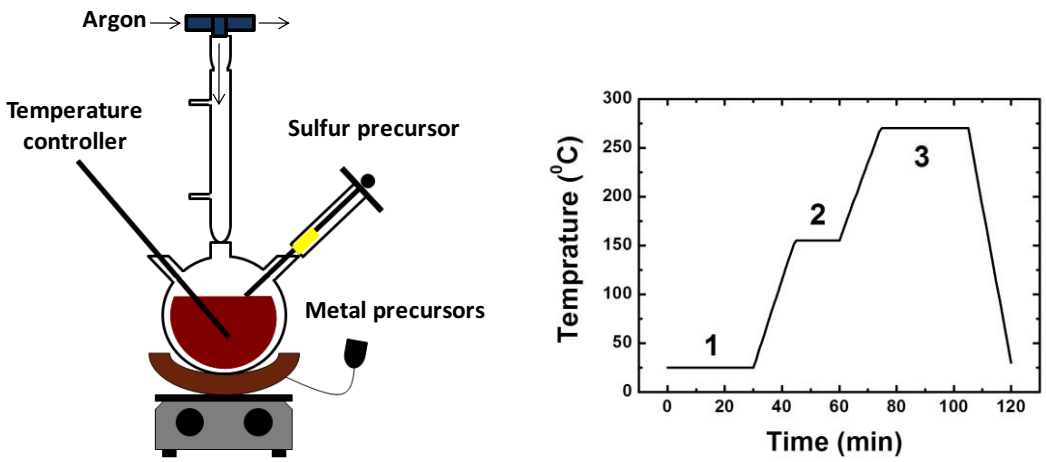

Figure 4. Schematic of a col.loidal synthesis system and a CIGS synthesis thermal profile: 1) purification 2) nucleation 3) growth.

3.1.2 CZTS Nanocrystal Colloidal Synthesis

The CZTS NP used in the chapter 5 were prepared by colloidal synthesis. 1.26 mmol of CuCl, 0.57 mmol of $SnCl_4 \cdot 5H_2O$, 1.35 mmol of ZnO and 0.5 mmol of octadecyl phosphonic acid (ODPA) were mixed with 30 ml of OLA under argon flow using a Schlenk line in constant stirring. The mixture was heated to 200 ºC and maintained at this temperature during 1 hour. After purging, the mixture was heated to 300 ºC. Then, an excess of the sulfur precursor, 1 ml of a 2 M solution of tetraethylthiuram disulfide in dichlorobenzene, was injected. The solution was maintained at this temperature during 30 min. Figure 5 shows the synthesis thermal profile. NPs were thoroughly purified by multiple precipitation and redisperion steps using 2-propanol and chloroform. Finally, NPs were dispersed in chloroform and stored in the glovebox until their posterior use.

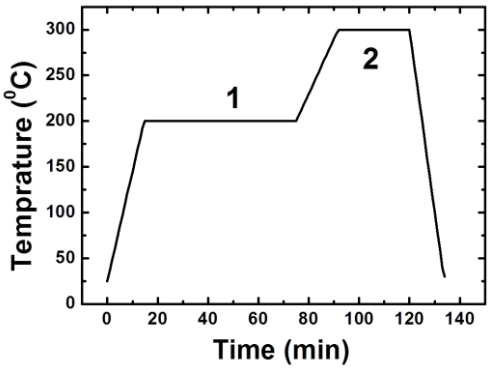

Figure 5. Thermal profile of a col.loidal CZTS NP synthesis: 1) purification 2) nucleation and growth.

CZTS NP organic ligands were displaced from the NP surface by using various short ligands. Solutions of NaCl, NaN_3 and KOH were used to replace organic ligands. Also solutions of $SnCl_4$, $ZnCl_2$ and CuCl were used in order to avoid introducing different elements to the CZTS structure. The exchange was carried out by mixing in a 1:1 ratio the chosen ligand solution with a molar concentration of 0.01M in formamide with the solution of NPs in chloroform. Figure 6 shows a schematic of the ligand exchange procedure. All mixtures were vigorously stirred and let stand until phase separation was observed. NP moved from the chloroform to the formamide phase. The final formamide solution containing the NP was washed several times with chloroform to drag all the remaining organic ligands surrounding the NP. NPs were finally precipitated using acetonitrile and redispersed in DMF. Figure 6 shows a schematic of the ligand exchange procedure.

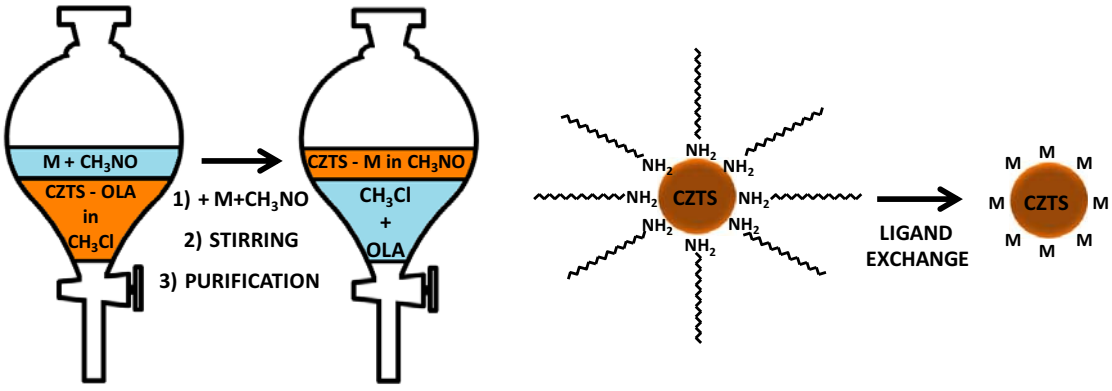

Figure 6. Schematized view of the procedure followed for the OLA displacement with a metal salt.

Also $SbCl_3$ and $(NH_4)_2S$, were used to replace organic ligands. Particularly, the $SbCl_3$ ligand exchange was carried out by mixing 5 ml of a 0.1 M $SbCl_3$ solution in formamide with 10 ml of a 10 g/L solution of NP in chloroform. The $(NH_4)_2S$ ligand exchange was performed by adding 1ml of $(NH_4)_2S$ (20 wt % in water) and 10 ml of formamide into a 10 ml solution of CZTS NP stabilized in chloroform (10g/L). The previously explained purification step was also used for $SbCl_3$ and $(NH_4)_2S$ ligand exchange systems.

3.2 CZTS Nanocrystal Continuous Production

The precursor solution for the continuous-flow process, reported in chapter 5, was prepared by dissolving $SnCl_4$ and $CuCl_2$ and ZnO in an OLA/Octadecene (ODE) mixture. In a typical preparation, 2.0 mmol of $CuCl_2{\cdot}H_2O$ (98%, Aldrich) and 1.0 mmol of $SnCl_4{\cdot}5H_2O$ (98%, Aldrich) were initially dissolved in a small amount of tetrahydrofuran (THF) to enhance the solubility of the $SnCl_4$ in OLA. After complete dissolution, 1.0 mmol of ZnO and a certain amount of OLA were added into the solution. The mixture was heated to 50−80 °C in a rotary evaporator. After complete dissolution of the ZnO, the pressure inside the evaporator was reduced to 5−10 mbar to remove THF and any other light products present in the reaction mixture. Just before the synthesis, specific amounts of sulfur and ODE were added to the solution containing the metal complexes. Figure 7 shows a scheme of the experimental setup used.

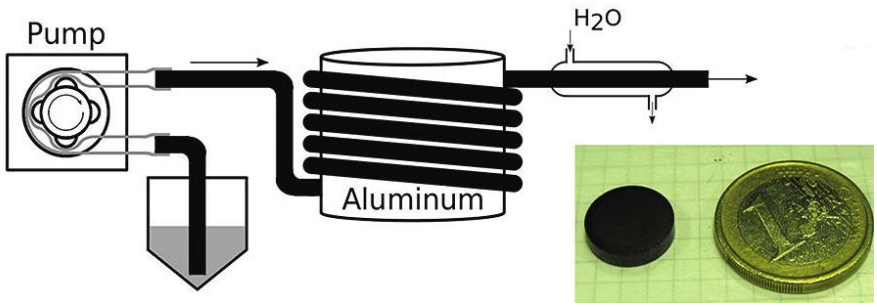

Figure 7. Scheme of the flow reactor setup and image of a 1 g pellet made of CZTS NP.

To purify the solution further from any low-boiling-point impurities (e.g., water or light-hydrocarbon impurities from ODE, the mixture was kept at 50 °C and 10 mbar until the sulfur was completely dissolved. The prepared precursor solution was pumped through a 1 m long

bronze tube having a 3 mm internal diameter and kept at a temperature in the range 300−320 °C. The flow rate was typically set within the range 1−5 mL/min. The reaction product was collected and washed several times by precipitation with isopropanol and redispersion in chloroform. The final product was readily soluble in various organic solvents (e.g., chloroform, THF, hexane).

3.3 CZTS Thin Film Deposition by Doctor Blade

CZTS films in chapter 5 were initially prepared by printing techniques from CZTS NP inks (schematic view in figure 8). CZTS ink is prepared by dispersing the NP within an organic solvent, 2-methyl 1-butanol, and then mixing it with an appropriate binder, ethyl cellulose plus 2-methyl 1-butanol. The binder is a viscous solution which is used to avoid crack formation on the surface of CZTS thin films at the time of printing or after the annealing treatments. Different amounts of solvent and binder were added in order to obtain a suitable ink and avoid crack formation.

Previous to deposit the ink, an adhesive scotch tape was used to cover the sides of the substrate acting as spacers. The film was only deposited in the scotch tape free area. Moreover, film thicknesses are equal to the scotch tape thickness. Afterwards, and before any thermal treatment, as printed CZTS films were dried at 100 ºC in a hot plate to remove the excess of organic solvent.

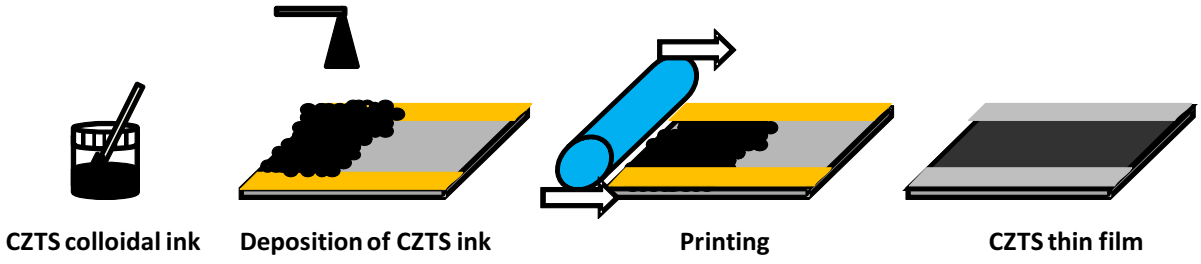

Figure 8. Schematic of a printing deposition procedure.

3.4 Spray Deposition of CIGS and CZTS Nanocrystals

CIGS and CZTS films from chapters 4 and 5 were prepared by a pulsed spray deposition system operated in open air conditions. Figure 9 displays a scheme of the custom-made

pulsed spray deposition system used in this work. The system used a pneumatic spray nozzle that employed nitrogen as the carrier gas and was controlled through an electrovalve. The substrate was vertically supported on a heated plate. The plate temperature and spray parameters, such as pulse time, number of spray pulses and time between pulses, were monitored and controlled through a computer. NP inks were deposited over 2x2 cm^2 Mo-coated SLG substrates.

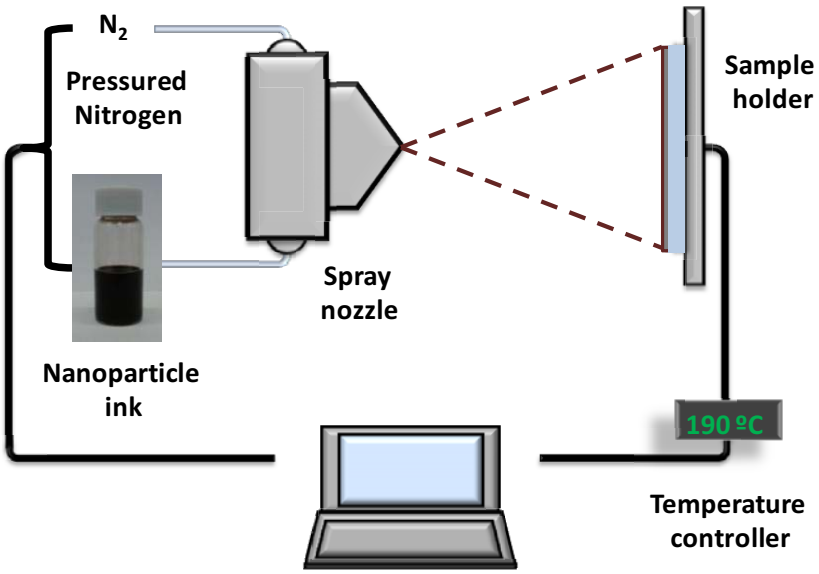

Figure 9. Schematic view of the pulsed spray deposition system used to produce CIGS and CZTS films onto Mo-coated SLG substrates.

3.5 Spin Coating of CIGS Nanocrystals

CIGS thin films in chapter 4 have also been prepared by spin coating deposition. Spin coating was performed on 2×2 cm^2 Mo-SLG substrates by applying a small amount of CIGS ink on the center of the substrate and using a first low speed rotation followed by a faster rotation in order to spread the coating material by centrifugal force. The thickness of the film can be adjusted by increasing or decreasing the number of spin coating cycles. Additionally, a drying step after each spin coating cycle is necessary to remove all remaining solvent. Accordingly, the sample is placed onto a hot plate at the required temperature to evaporate the solvent.

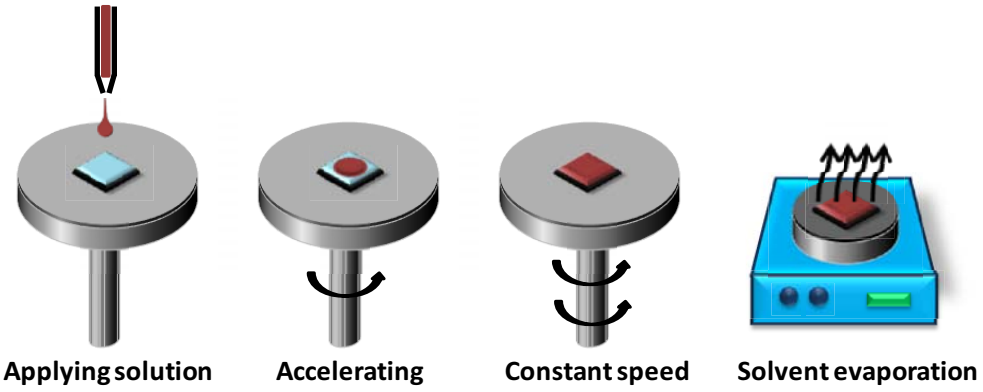

Figure 10. Schematic view of the spin coating deposition process used to produce CIGS films onto Mo-coated SLG substrates.

3.6 CIGS and CZTS Annealing Treatment

Selenization treatments were performed within a (partially) closed graphite box (with a small hole in the centre of its lid). Inside this graphite box, several pellets of elemental Se (30 mg each one) were introduced together with the samples and loaded into a quartz tube furnace in Ar atmosphere (figure 10). The Se amount was varied in a wide range, from 60 mg to 240 mg.

Crystallization processes of CIGS thin films from chapter 4 were carried out in the temperature range from 450 ºC to 550 ºC, placing the samples inside a graphite box in a Se-rich atmosphere (120 mg of elemental Se).

CZTS films from chapter 5 were crystallized during 60 min in a Se (100 mg) and Sn (15 mg) rich atmosphere while supported inside a graphite box at temperatures ranging from 475 ºC to 575 ºC. Selenization was accomplished by a two-step heating process. In the 1st step, Se incorporation was allowed into the CZTS layer at 250C. The 2nd step, involved a selenization and recrystallization process which was performed at an elevated temperature of 550°C.

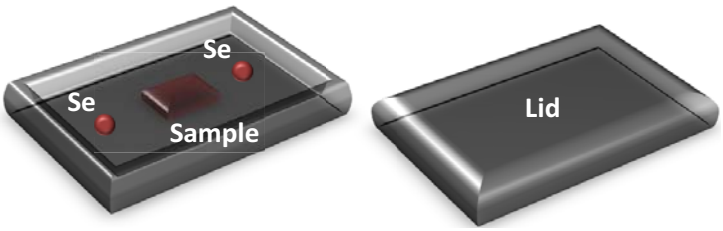

Figure 10. Schematic of a graphite box used to perform selenization/sulfurization treatments.

3.7 CIGS and CZTS Device Fabrication

Solar cells were fabricated from the crystallized CIGSe ($CuIn_{1-x}Ga_xSe_2$) and CZTSe films deposited on 2x2 cm^2 SLG substrate with 800 nm of magnetron-sputtered Mo as the device back contact. A 60 nm thick CdS buffer layer was deposited by chemical bath deposition. To complete the device, a layer of i-ZnO (intrinsic ZnO) (50 nm) and a 250 nm AZO layer were deposited by pulsed DC-magnetron sputtering (CT100 Sputtering System, Alliance Concepts). Finally the samples were scribed to 3 x 3 mm^2 cells using a micro diamond scriber MR200 OEG.

3.8 Nanoparticle, Thin Film and Device Characterization

3.8.1 Nanoparticle Characterization

The size, shape and crystallographic structure of the prepared NPs were characterized by transmission electron microscopy (TEM). Samples were prepared by placing a drop of the colloidal solution containing the NPs onto a carbon coated copper grid at room temperature and ambient atmosphere. TEM micrographs were obtained in a JEOL 2100 operating at 200 keV.

UV-Vis (Ultraviolet - visible) absorption spectrum from NP was recorded on a LAMBDA 950 UV-Vis spectrophotometer from Perkin Elmer.

3.8.2 Ligand Exchange Characterization

The amount of organic carbon of NP before and after ligand exchange was measured by elemental analysis (EA) and thermo gravimetric analysis (TGA). CHN quantitative elemental analysis was performed using an elemental organic analyzer Thermo EA 1108, working under a helium flow at 120 ml/min, combustion furnace at 1000 ºC, chromatographic column oven at 60 ºC and oxygen loop 10 ml at 100 kPa. TGA was performed on a Perkin-Elmer TGA 4000 with which dried and purified NPs were heated up to 500 ºC under a nitrogen flow during 60 min.

In chapter 5, dried CZTS NP samples before and after ligand exchange with $SbCl_3$ and $(NH_4)_2S$ were also measured by FTIR spectroscopy. An Alpha Bruker FTIR spectrometer with a

platinum attenuated total reflectance (ATR) single reflection module was used to acquire the Fourier-transform infrared (FTIR) spectra.

3.8.3 Thin Film Morphology and Composition Characterization

The morphology and composition of the layers before and after heat treatment, in chapter 4 and 5, was characterized with an SEM microscope (ZEISS Auriga) equipped with an energy dispersive X-ray spectroscopy (EDX, Oxford Instruments X-Max Silicon Drift Detector) detector.

Composition was also assessed using optical emission spectroscopy by means of inductively coupled plasma (ICP) on a Perkin Elmer Optima 3200 RL system. CZTS/CZTSe and CIGS/CIGSe films were dissolved in aqua regia for this purpose. X-ray photoelectron spectroscopy (XPS), was also used to assess the thin film composition. XPS spectra were obtained using a SPECS SAGE ESCA system employing Mg Ka as the X-ray source.

3.8.4 Structural Characterization

XRD measurements were carried out in a Bruker AXS D8 ADVANCE X-ray diffractometer with Cu K1 radiation (1.5406 Å). Raman scattering measurements were performed using a T64000 Horiba Jobin–Yvon spectrometer. Excitation was provided with the 514.5 nm emission line of an Ar+ laser and measurements were performed in backscattering configuration. The penetration depth of scattered light in the samples is estimated to around 100 nm. The focused spot size on the measured surface was about 100 µm, with an excitation power of 10 mW in order to avoid the presence of thermal effects in the spectra.

3.8.5 Photovoltaic Performance Characterization

PV devices were characterized using an AAA Abet 3000 Solar Simulator previously calibrated with a Si reference cell. The External Quantum efficiency (EQE) of the cells was measured with a Bentham PVE300 system in the 300-1600 nm wavelength ranges. The system was calibrated with Si and Ge photodiodes.

4 Solution Processed CIGSe Solar Cells

To produce smooth, crack-free and highly crystalline absorber layers are the main challenges in the fabrication of thin film solar cells using NP-based solution-processing technologies. This chapter addresses the optimization of the spray deposition parameters to produce highly homogeneous CIGS thin films with controlled thickness using NP-based inks. I further explore the use of inorganic ligand exchange strategies to introduce metal ions able to promote crystallization during the selenisation of the layers, removing structural defects and GB that potentially act as recombination centers.

4.1 Introduction

CIGSe thin films can be prepared by vacuum and non-vacuum technologies [20,105,106]. On the one hand, vacuum deposition methods allow achieving the highest device efficiencies, but they require large capital and operation costs, and are characterized by relatively low material yields and throughputs. These drawbacks compromise their potential to substantially reduce the current cost of PV modules. On the other hand, non-vacuum technologies, such as printing or electrodeposition, require lower capital investments and have associated lower maintenance costs. They also provide higher material yields and production rates, what make them highly appropriate for large scale industrial production. While solution-based approaches have reached efficiencies up to 15.2 % with CIGSe, their main limitation is the lower device efficiencies generally obtained when compared with vacuum-based technologies. Among the different solution-based technologies, the printing or spraying of colloidal NPs is particularly interesting to produce layers of quaternary materials with unmatched composition and phase homogeneity at the nanometer scale. [30,87,107,108] Such unparalleled control over material properties at the atomic scale is a result of the high level of control in the growth of these compounds recently reached by colloidal synthesis routes. [35,53,109,110] Nevertheless, efficient PV devices require not only compositionally homogeneous absorbers, but also continuous and dense layers made of large and defect-free crystal domains. [61,111] To properly crystalize CIGSe absorber layers, an

annealing treatment at a temperature close to 550℃ in a chalcogen atmosphere is generally used. As I explained before, a chalcogen exchange during the crystallization process promotes the formation of larger grains and denser layers. [87] However, the proper crystallization of the absorber layer is still one of the main challenges involved in the fabrication of PV devices by solution-based approaches. Several strategies to promote grain growth and to reduce the process temperature have been attempted. These strategies include the incorporation of Na, CuSe NPs or Sb′ in the absorber layer and the use of a multi-step selenization process. [89,95,103108,112,113]

In this chapter, I systematically optimized the ink formulation and spray deposition conditions to produce highly homogeneous, smooth and crack-free CIGS layers from NP-based inks. This chapter also describes the potential of crystallization promoters to achieve CIGSe absorbers with improved crystalline quality.

4.2 Results and Discussion

4.2.1 CIGS Nanocrystal Synthesis

CIGS NPs obtained by colloidal synthesis described in the previous chapter, had an average particle size of 20 ± 5 nm as observed from TEM characterization (figure 1). Composition can be adjusted in the whole range from $CuInS_2$ to $CuGaS_2$ by controlling the amounts of the different precursors. For the present work, I set the composition to $CuIn_{0.75}Ga_{0.25}S_2$, as measured by EDX. CIGS crystal structure was identified with wurtzite by XRD analysis (figure 1). I selected a synthesis procedure that yields wurtzite CIGS because the use of NPs with metastable crystal structures has been reported to provide an additional driving force for film crystallization during the selenization process. [84]

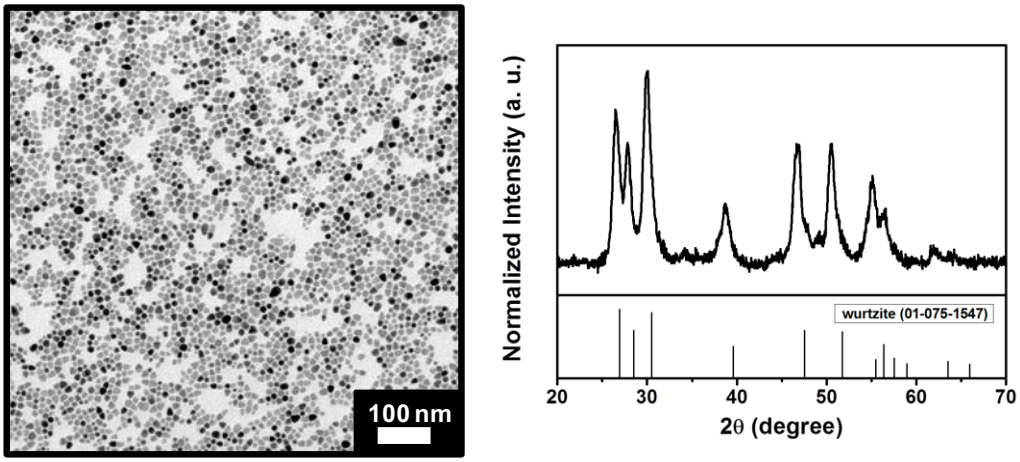

Figure 1. Representative TEM micrograph and XRD pattern of wurtzite CIGS NPs.

4.2.2 Precursor Ink Formulation

To create device-grade films from colloidal NPs, one unavoidable step is to remove the long organic ligands that were used to control NP growth during its synthesis in solution. NP ligands not only strongly compromise the film crystallization during the selenization treatment, but also result in relatively large amounts of carbon that accumulate between the absorber layer and the back electrode. [52] To overcome this limitation, organics can be removed after deposition by treating the film with compounds such as hydrazine. [114] For this treatment to be effective, the thickness of the film to be treated is strongly limited. Therefore, this treatment would need to be implemented after each spray pulse, what strongly complicates the layer growth process. The use of highly toxic compounds is another important limitation of the organic removal after deposition.

Due to the unsolved limitations involved in the organic removal after NP deposition, a suitable alternative to get rid of surface ligands is to displace them from the NP surface while in solution. The main challenge of this strategy, especially for spray deposition, is to remove the surface ligands without compromising the ink stability. Thus, when removing the surface ligands that keep NPs apart by steric repulsive forces, an electrostatic repulsion need to be introduced to prevent aggregation. This process is generally assisted by a change to a more polar solvent.

In this study OLA was displaced from the NP surface using $(NH_4)_2S$, which is a particularly suitable compound to prepare sulphide-based inks. [34,115] After ligand displacement, NPs were dispersed in DMSO which was used due to its very low toxicity and its suitable boiling point and surface tension. To minimize the final carbon content of the film, no binder was used during ink formulation. The final ink was stable for long periods of time, above months.

4.2.3 Spray Deposition of CIGS Nanocrystals

Several spray deposition conditions, such as substrate temperature, pulse duration, pulse number and time between spray pulses were carefully adjusted to obtain high quality CIGS thin films with a proper morphology, homogeneity and thickness (figure 2).

To produce homogeneous films, substrate temperature needs to be high enough to ensure the solvent removal upon contact with the substrate surface. Too low substrate temperatures resulted in the formation of ink droplets on the substrate, which strongly compromised the film homogeneity. Too high temperatures were also detrimental as the evaporation of the solvent before reaching the film resulted in the deposition of rough layers formed by particle aggregates. In the present work, the substrate temperature was set to 190℃, which is very close to the boiling point of the used solvent, DMSO.

As the NP ink was at ambient temperature when sprayed, to maintain the substrate temperature constant during deposition of the whole layer thickness, the pulse duration and the time between pulses had to be carefully adjusted. With each spray pulse, the substrate temperature decreased a magnitude proportional to the spray pulse duration. Therefore, too long pulses resulted in the formation of ink droplets, which translated in the growth of inhomogeneous films. Another important parameter was the time between pulses. Long enough times were needed to recover the substrate temperature. However, to increase the time between pulses would be obviously detrimental in terms of cost and productivity in an industrial scenario. The minimum time required depended on the duration of the pulse, the substrate temperature, the thermal inertia of the support and the power of the heater. In our set-up, pulse duration was set to 400 msec and the time between pulses to 30 sec.

The ink inorganic load was another key parameter determining the final quality of the layer. Highly porous thin films were obtained by using low concentrated NP inks, as a consequence of spraying lower amount of NP on each spray pulse. As shown in figure 2, the more concentrated the solution sprayed, the smoother the films obtained. Spraying high concentrated inks, higher amount of NPs would be deposited on each spray pulse, leading and easily accommodation of the NP and thus obtaining compact films. Finally, by using very high concentrated inks, increased amounts of NPs would be deposited on each spray pulse, which is translated in film stresses and would produce surface defects and cracks. A limit was found in the ink stability, associated with the NP solubility within the selected solvent. An unstable ink easily clogged the nozzle, which was an obvious limitation. The CIGS NP load was varied in the range between 1 and 60 g/L to investigate the inorganic load on the final layer quality. We finally set the inorganic load of inks prepared from CIGS NPs to 10 g/L.

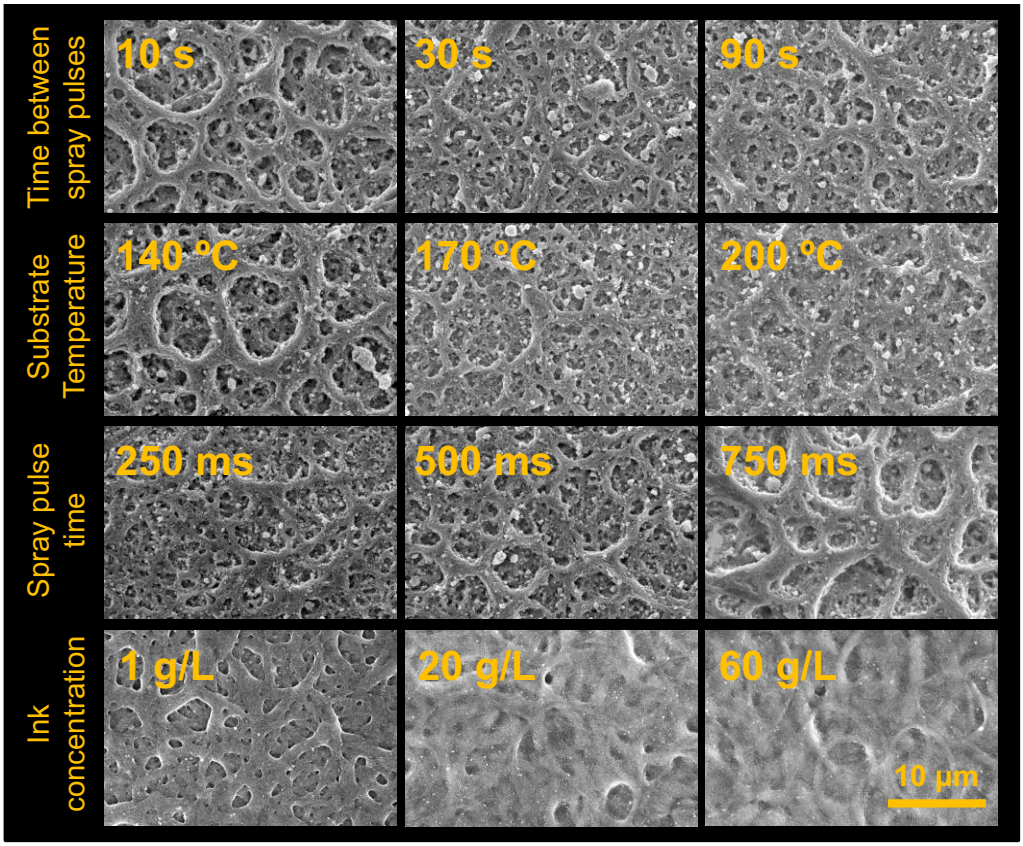

Figure 2. Top view SEM images of CIGS thin films obtained using different spray conditions: time between spray pulses (10-90 sec), substrate temperatures (140-200°C), spray pulse times (250-750 msec) and ink concentrations (1-60 g/L).

Finally, all other parameters being the same, the number of pulses determined the film thickness. This is shown in figure 3, where a series of samples with thickness between 1.5 um and 5.5 µm obtained by increasing the number of pulses from 10 to 40 are displayed. A typical thin film expansion is reported for CIGS and CZTS thin films after annealing treatments due to the initial compactness and the further grain growth of the material.[116] Nevertheless, a thickness reduction takes place after selenization of sprayed films. The contraction of the film could be attributed to its initial porosity, and the further compaction after grain growth by crystallisation, with which would fill all the possible free spaces, and subsequently reduce the initial film thickness.

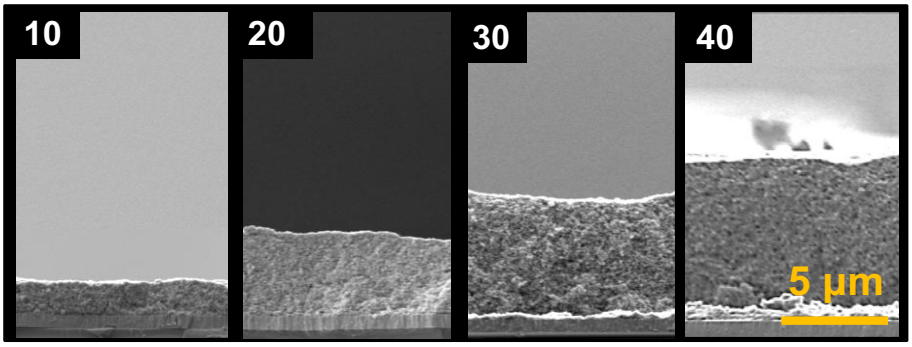

Figure 3. Cross-section SEM images of CIGS thin films prepared using a number of spray pulses between 10 and 40, as noted.

4.2.4 Selenization of CIGS Thin Films

Films were crystallized in a tubular furnace in the presence of elemental Se at temperatures in the range from 450℃ to 550℃ during 30 min. A complete replacement of the S by Se, transforming the precursor CIGS wurtzite film into a CIGSe chalcopyrite film took place even at 450℃ as observed from XRD measurements (figure 4).

In terms of chemical composition, the relative content of Ga and In was preserved during the selenization process. Compositions of $CuIn_{0.7}Ga_{0.26}S_{0.7}Se_{1.8}$, $CuIn_{0.73}Ga_{0.26}Se_{2.2}$ and $CuIn_{0.7}Ga_{0.27}Se_{2.1}$ were measured by EDX after selenizing the precursor $CuIn_{0.7}Ga_{0.24}S_{3.1}$ film at 450℃, 500℃ and 550℃ respectively.

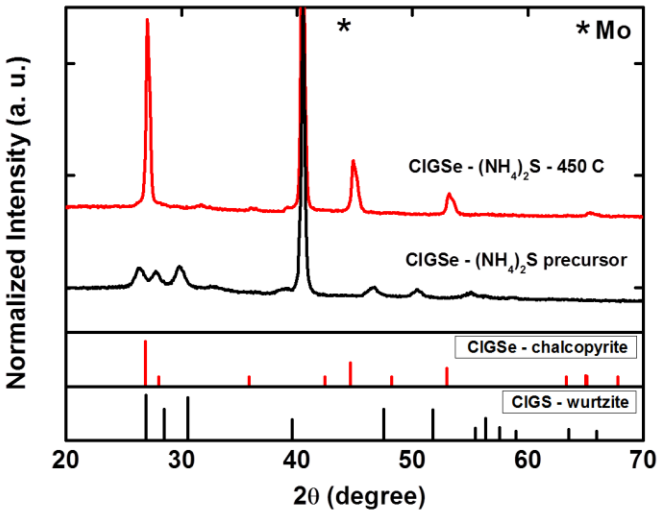

Figure 4. XRD pattern of wurtzite CIGS precursor thin film and chalcopyrite CIGS after selenization at 450℃.

To further promote the NP-based film crystallization, a boost of the ionic diffusion and atomic reorganization was required. In this direction, we assessed the potential of extrinsic metal ions to promote crystallization. Bi and Sb have been proposed as crystallization inducers in thin films of CIGS and related compounds [34,89,95]. While the crystallization induction mechanism is not understood in detail, it is accepted to be based on the local formation of a low melting point Bi and Sb-based alloy at the grain surface. The decrease of the ion diffusion energy associated with the external metal ion incorporation ultimately promotes the diffusion-controlled crystallization process. In CIGS films grown by vacuum-based techniques, external impurities can be co-deposited or introduced at the film surface using an additional step. When producing CIGS thin films from NP-based inks, one very suitable strategy to introduce external crystallization promoters is to take advantage of the ligand exchange step required to remove the ligands used in the NP synthesis. Thus, instead of $(NH_4)_2S$, we used $BiCl_3$ and $SbCl_3$ to displace the long aliphatic chains and at the same time introduce Bi or Sb ions on the NP surface. XRD measurement show that the introduction of external dopants does not affect to the initial wurtzite structure (figure 5).

After ligand exchange, the initial CIGS inks contained a percentage of around 5 % of Bi or Sb, as determined by ICP. To investigate the effect of the Bi and Sb incorporation, we annealed CIGS-$(NH_4)_2S$, CIGS-$BiCl_3$, CIGS-$SbCl_3$ NP-based films in the temperature range from

450°C to 550°C in a Se atmosphere during 30 min. Before the selenization, the samples were also dipped in NaCl 1M for 10 min. A complete substitution of S by Se took place during the selenization, transforming the precursor CIGS wurtzite film into a CIGSe chalcopyrite film, as shown in the XRD graphs of figure 5. In addition, EDX measurements corroborate that the Ga/(In+Ga) relative content is preserved in the process, obtaining the same values (in the range 0.25-0.26) before and after selenisation.

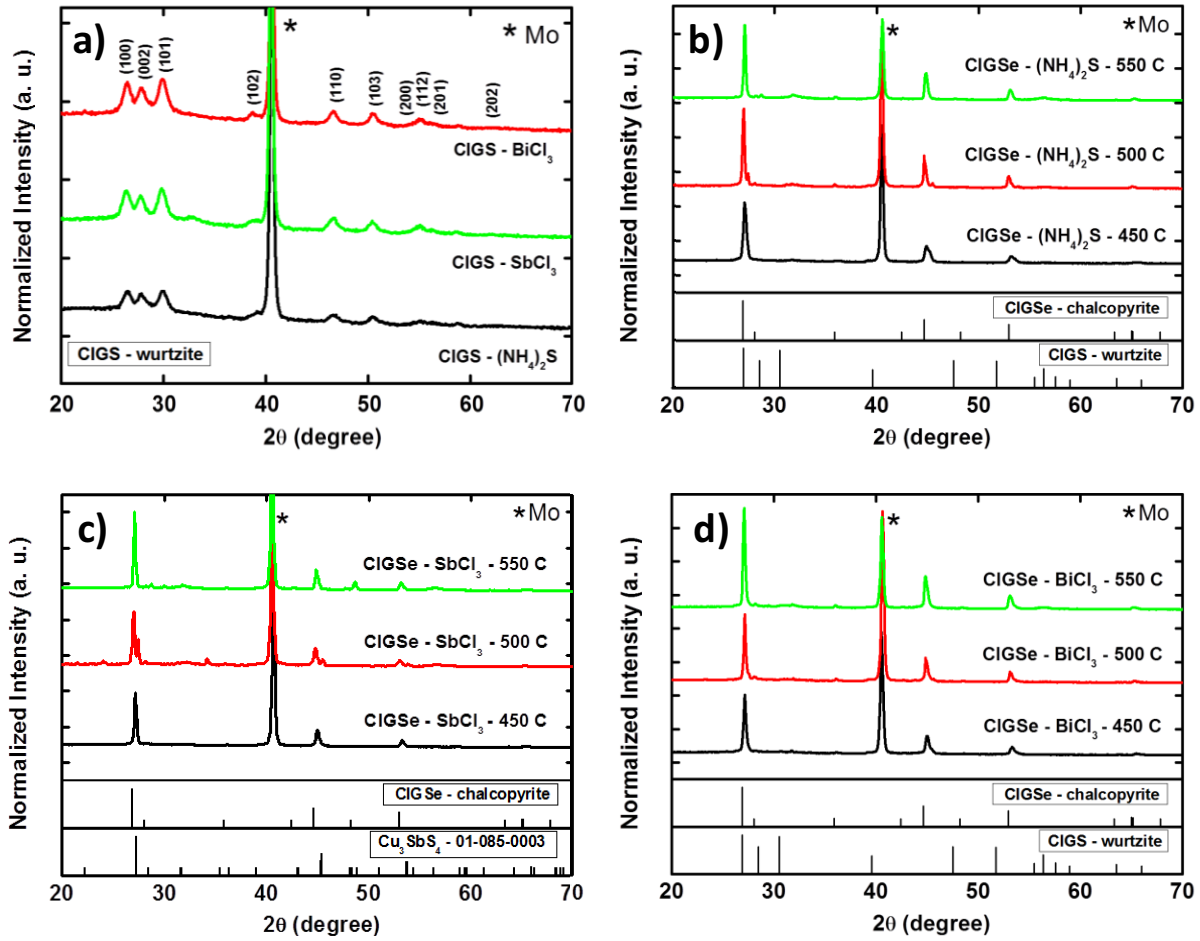

Fig. 5. XRD patterns of precursor wurtzite CIGS thin films prepared with CIGS-$(NH_4)_2S$, CIGS-$SbCl_3$ and CIGS-$BiCl_3$ (a) and XRD patterns of selenized CIGS-$(NH_4)_2S$ (b), CIGS-$SbCl_3$ (c) and CIGS-$BiCl_3$ (d) films at 450°C, 500°C and 550°C.

Figure 6 displays cross-section SEM images of the films produced after the selenization of the CIGS-$(NH_4)_2S$, CIGS-$BiCl_3$ and CIGS-$SbCl_3$ NP-based films. Homogeneous films composed of a small grained layer close to the back contact and covered with a top region with larger

and more crystalline grains, were obtained after crystallization of CIGS-$(NH_4)_2S$ films at 500°C and 550°C (figure 6, left column). This bi-layer structure is commonly observed in sintered ink-based absorbers. While small grained layers were obtained from CIGS-$(NH_4)_2S$ samples processed at temperatures between 450°C and 550°C, the introduction of Bi slightly promoted the crystal growth at low temperatures (450 °C, 500 °C). However, the incorporation of Bi did not allow the formation of fully crystalline layers even after sintering at 550°C. In contrast, highly crystalline films were obtained from the CIGS-$SbCl_3$ precursors after sintering at 500°C and 550°C, demonstrating the large potential of Sb to promote crystal growth.

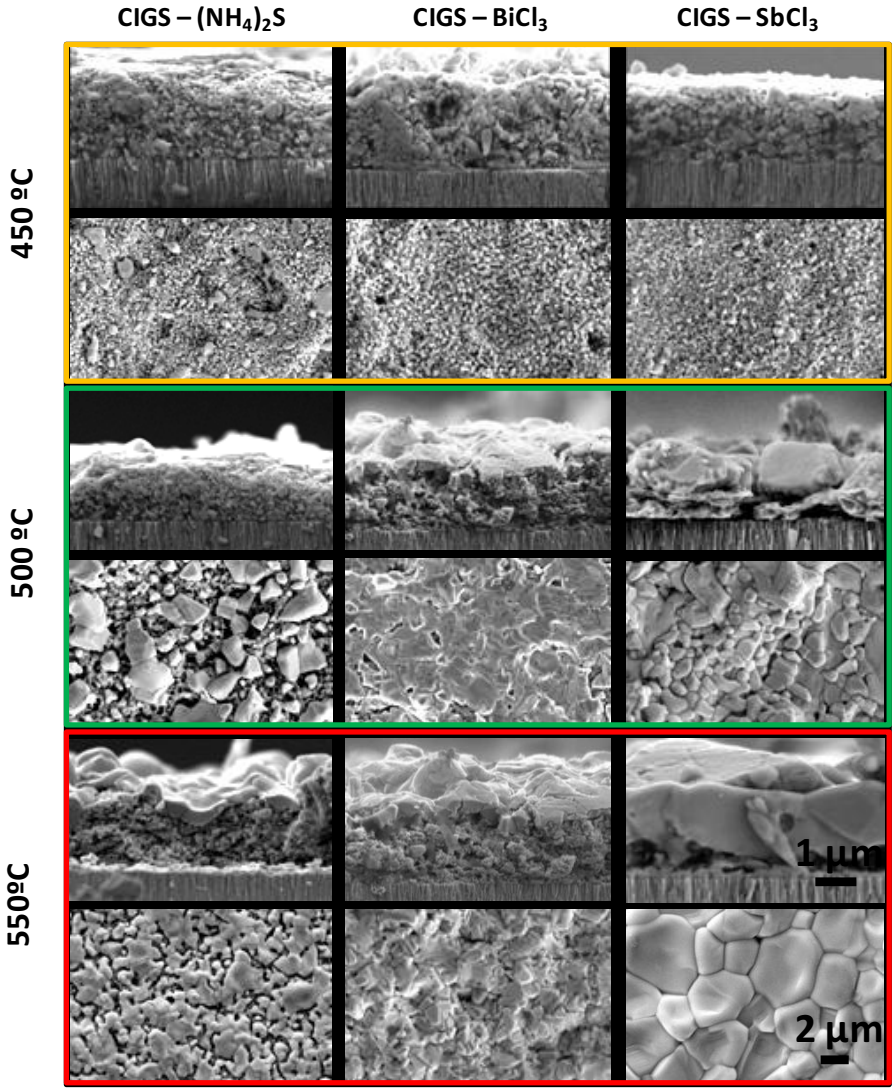

Figure 6. Cross-section SEM image of CIGS-$(NH_4)_2S$, CIGS-$BiCl_3$, and CIGS-$SbCl_3$ thin films after selenization at 450°C, 500°C and 550°C.

The introduction of Sb ions at the NPs surface resulted in the formation of a low melting point Sb-based chalcogenide which locally increased ionic mobility and thus the material capacity for mass transfer and reorganization. As crystallization proceeded and crystal domains grew, Sb was accumulated at the crystal surface. After the annealing treatment at 500℃ or above, no Bi or Sb was detected within the CIGSe film. These results suggest that Bi and Sb did not incorporate to the bulk CIGSe crystals but evaporated during the selenization process. The elimination of the external element from the final layer is important to ensure it does not negatively influence the final optoelectronic properties of the device.

4.2.5 CIGS Photovoltaic Performance

Solar cells were finally fabricated with CIGSe-$(NH_4)_2S$, CIGSe-$BiCl_3$, and CIGSe-$SbCl_3$ absorbers using the conventional structure consisting of CdS/i-ZnO/ITO. Almost all the cells exhibited a clear PV behaviour (figure 7). It is interesting to note that the best values were obtained for CIGS-$(NH_4)_2S$ thin films selenized of 550℃, thus, meaning that a better crystallisation obtained by introducing external dopants, Sb and Bi (figure 6), was not translated in a better PV performance. Nevertheless, even obtaining poor PV parameters and efficiencies, it was confirmed that an organic carbon removal is necessary in order to complete a NP based solar cell device showing PV behaviour. Further work is required in order to analyze interfaces and identify possible secondary phases or impurities, responsible of poor PV performance.

Additionally, PV parameters show an evolution depending on the temperature. As shown in table 1, J_{sc}, V_{oc} and FF were improved with increased selenization temperature. Poor PV parameters obtained from CIGS thin films selenized at low temperatures, 450℃, were translated in no efficient PV devices. By using higher selenization temperatures, highly crystallized and smooth surfaces were obtained, thus improving the interface between CIGS/CdS. The better contact between those layers is translated in an increased V_{oc} and consequently in a better FF.

Samples	J_{sc} (mA/cm²)	V_{oc} (mV)	FF (%)	Efficiency (%)
CIGSe-$(NH_4)_2S$ – 450ºC	1.9	98	28.5	0
CIGSe-$(NH_4)_2S$ – 500 ºC	7.5	136	29.4	0.26
CIGSe-$(NH_4)_2S$ – 550 ºC	8.1	206	30.7	0.5
CIGSe-$BiCl_3$ – 450ºC	2.6	51	27	0
CIGSe-$BiCl_3$ – 500 ºC	6.7	134	26.8	0.24
CIGSe-$BiCl_3$ – 550 ºC	5.7	172	34.5	0.34
CIGSe-$SbCl_3$ – 450ºC	3.5	74	25.3	0
CIGSe-$SbCl_3$ – 500 ºC	7.4	164	29.1	0.33
CIGSe-$SbCl_3$ – 550 ºC	6	190	34.7	0.38

Table 1. Electrical parameters of the solar cells

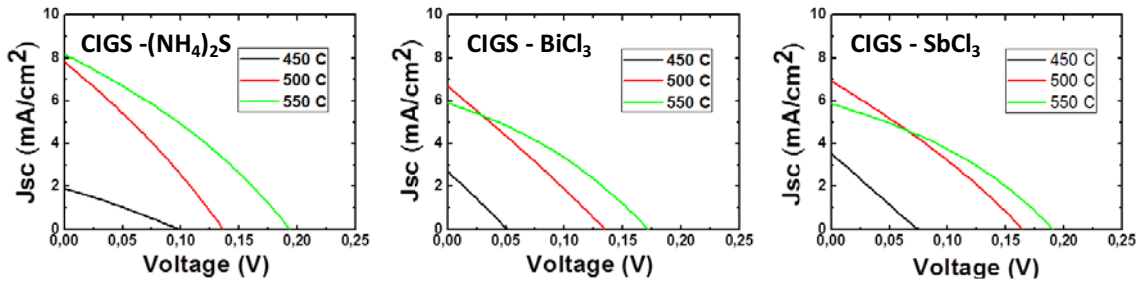

Figure 7. PV characteristics of CIGSe solar cells prepared from CIGS-$(NH_4)_2S$, CIGS-$SbCl_3$ and CIGS-$BiCl_3$ NPs.

4.2.6 Alternative Strategies for Grain Growth Optimization

As described in the previous section, and even if in some cases a certain trend of improvement of the recrystallisation is observed, it has not been possible to achieve in any case a fully recrystallised layer. This has lead to the development and analysis of alternative strategies to achieve a significant increase in grain size in the layers, without compromising compactness. The strategies investigated include: application of a mechanical pressure on the as-deposited precursor layers to improve their compactness, a soft intermediate annealing stage, 300°C in a hot plate, before the recrystallisation to increase the density of the layers and favor a more efficient removal of carbon containing species; a photonic sintering in air before recrystallisation. [117,118] This process has been reported to be useful for the sintering of layers formed by metallic NPs, a dipping of the samples with a NaCl solution

to favour incorporation of Na and placing a Se sheet on the surface of the samples during the recrystallisation step in elemental Se ambient. [108,119,120,121] During the process the Se sheet on the layer is covered with a glass sample. Figure 8 shows cross-section and top view SEM images of CIGS-$(NH_4)_2S$ samples selenised at 550ºC with the different proposed strategies.

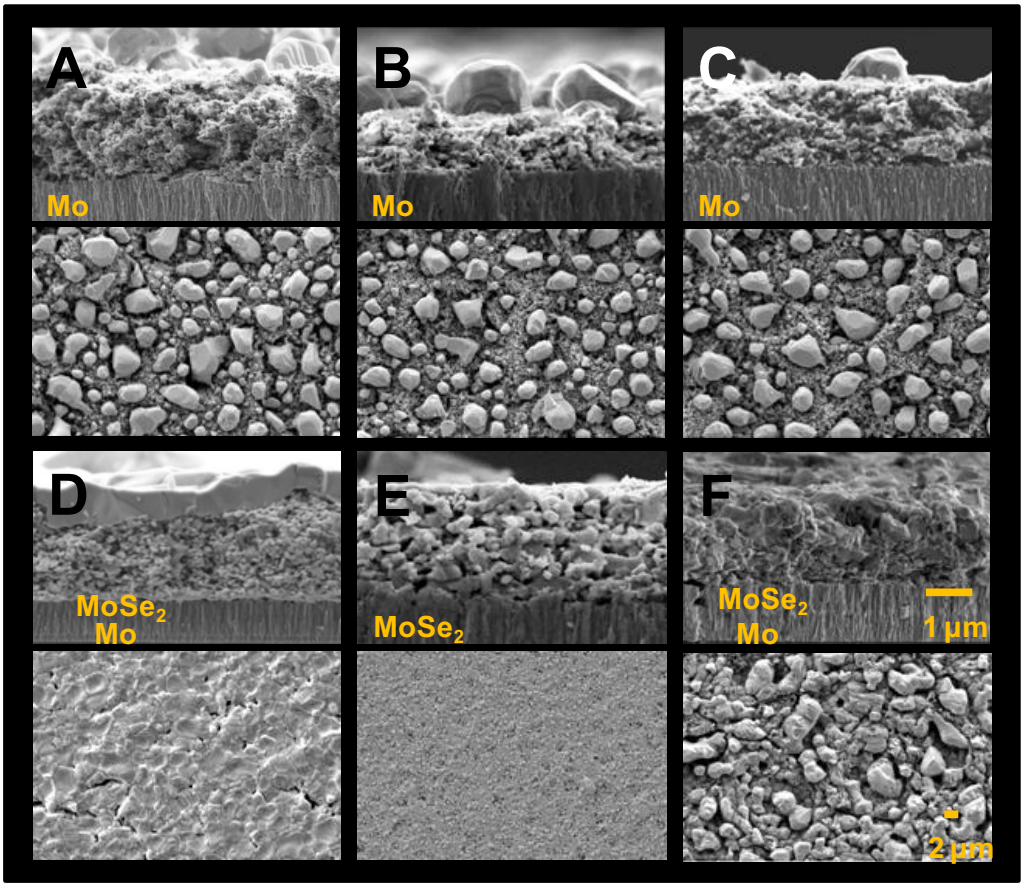

Figure 8. Top view and cross-section SEM image of CIGS-$(NH_4)_2S$ thin films after selenization,with precursor conditions: A) mechanically pressed, B) preannealed at 300°C under argon flow, C) after flash annealing, D) selenization at increased temperature, 585°C, E) NaCl (1 M) soaking for 10 min and selenized at 585°C, F) selenization with a selenium sheet on top of CIGS film at 600°C.

To favour full selenisation of the layers, in all these experiments annealing time has been increased to 1 hour. CIGS-$(NH_4)_2S$ thin films selenized after mechanically pressing the precursor (figure 8A), after preannealing the precursor (figure 8B) and after a flash annealing of the precursor (figure 8C), does not show a clear improvement in the crystalline quality

layers in relation to those annealed at the same temperature without any of these processes, in general, crystallization was only favoured in the surface region, and this was also accompanied by excessive selenisation of the Mo back layer. An additional feature that can improve the crystalline quality of the layers is an increase of the selenisation temperature. To investigate this, samples were selenised at 585 ℃ during 1 hour. Increasing the selenisation temperature allows achieving a higher degree of crystallization in the surface region. However, the back region shows still a lower crystalline quality, and the Mo back layer is almost fully selenised (figure 8D). Although the incorporation of Na helps to obtain an increased grain growth and a more compact film, a fully selenization of the Mo back layer is observed (figure 8E). In contrast, the use of a Se sheet on the surface of the precursor allowed achieving a significant improvement in the crystalline quality of the sample, being the sample characterized by the presence of bigger grains through the whole thickness of the layer (figure 8F). In addition, in this case not all Mo was selenised.

CIGS thin films are usually Na-doped by Na diffusion from the glass substrate to the absorber film. Moreover, extra Na could be supplied by a wide variety of methods. [108,122,123,124,125,126] Conventional procedures involves the deposition of a Na layer over the absorber film by spin coating or a dip coating of the CIGS film into a solution of NaCl prior selenization. The use of NP inks gives us the opportunity to introduce external impurities via the addition of the desired doping agent directly to the NP solution. With this procedure it is possible to control the concentration of the doping agent into the film.

We added different amount of Na_2S x $9H_2O$ into the CIGS-$(NH_4)_2S$ inks, to prepare 0.008 M and 0.05 M Na_2S x $9H_2O$ concentrated solutions. Those solutions were used to prepare thin films, which were then selenized under standard conditions. As seen in figure 10, the low Na_2S x $9H_2O$ concentration result in a typical bi-layer formed by a top crystallized layer and bottom nanoparticulate layer, similar to the un-doped CIGS-$(NH_4)_2S$ film. At the highest Na_2S x $9H_2O$ concentration, an improved crsytallinity was obtained. The inconvenient of using inks with high Na content is the fact that Na impurities would remain in the film. Na impurities could be eliminated by different chemical etching procedures. The selenization of

the back contact could be solved by using a barrier layer over the Mo, to prevent its crystallization or by adjusting Se and Na sources to prevent and control its selenization.

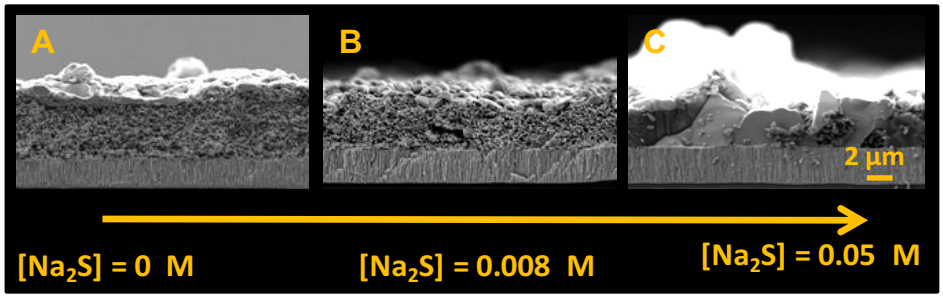

Figure 10. Cross-section SEM image of selenized CIGS-$(NH_4)_2S$ thin films, prepared with an ink containing different concentrations of Na_2S x 9 H_2O.

To solve the problems related to the uncontrolled formation of $MoSe_2$ during the selenization step, we modified the Mo layer. Low-density Mo layers are prepared by a novel process by increasing the pressure during the sputtering deposition. CIGS impurities, such as remaining organic carbon, would diffuse to the low-density (porous) Mo layer during selenization, allowing the formation of highly crystalline thin films.

Figure 11 shows the effect of the Mo substrate in a standard selenisation process (550° C, 30 minutes). Replacement of the standard Mo back layer by the layer deposited at higher pressures leads to a strong decrease in the thickness of the $MoSe_2$ at the back region, together with a better crystallization of the surface region of the layer. These results are very promising, as they show the possibility to decrease the degree of selenization of the back Mo layer by optimizing the deposition of the Mo layer on the glass substrates.

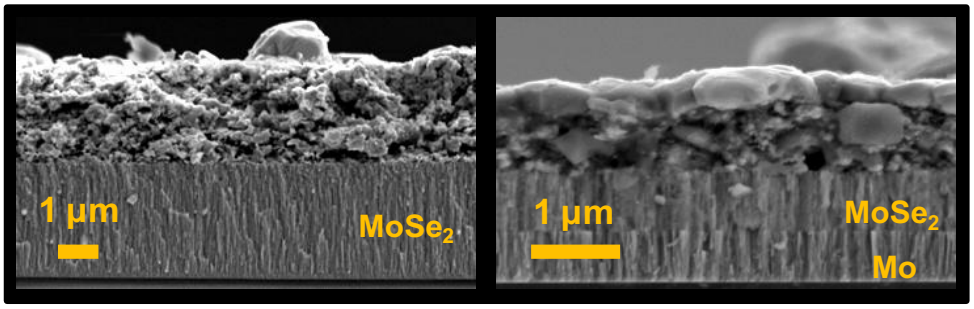

Figure 11. Cross-section SEM image of Mo back layer on samples selenised following the standard process (550°C, 30 minutes).Left: standard Mo; right: modified Mo.

4.2.7 Spin Coated CIGSe based Solar Cells

Alternative deposition techniques to prepare CIGS thin films were tested regarding the poor efficiencies obtained from sprayed CIGSe solar cells. In this section chalcopyrite CIGS NPs were used as precursor to prepare thin films by spin coating technique. Chalcopyrite CIGS NPs treated with $(NH_4)_2S$ were prepared and provided by the Instituto Italiano di Tecnologia (IIT) group. [127] The synthesis of chalcopyrite $CuIn_xGa_{1-x}S_2$ NPs were prepared by colloidal synthesis. CuCl, $InCl_3$, and $GaCl_3$ were mixed in a sulfur solution containing ODE and OLA and heated up to 250℃ during 30 min. The NP solution is then purified by precipitation and ligand exchanged with $(NH_4)_2S$. CIGS-$(NH_4)_2S$ NPs were dissolved in DMSO in a concentration around 80g/L for its further deposition.

Spin coating was performed on 2×2 cm² Mo-SLG substrates by applying 100 µL of CIGS ink on the center of the substrate and using a first low speed of 600 rpm for 6 seconds followed by a faster 1600 rpm for 30 seconds. 10 cycles of spin-coating were used with drying steps between each cycle in order to remove the solvent. The drying steps were performed by placing the sample onto a hot plate at 200℃ during 1 min (under air).

Afterwards, CIGS films were reactively sintered under Se atmosphere at high temperature (550℃), 1 bar and during 30 min to form crystalline CIGSe layers. No CIGS crystallization was observed by sintering under Ar atmosphere. It was then decided to incorporate hydrogen into the carrier gas, by using Ar/H_2 (95% Ar - 5% H_2) forming gas, all the other parameters being the same. By incorporating a few of hydrogen, crystallization was obtained at the surface of the film, as it can be observed in the figure 13. Grains of the micron size were clearly distinguished, indicating the effectiveness of hydrogen for the sintering during the selenization of CIGS nanoparticles-based films. Absorber thicknesses around 1-2 µm with a dual layer (a top one well crystallized with large grains and a bottom one with smaller grains) were obtained. The thickness of the absorber was around 1 µm and almost all the Mo was selenized, as it can be seen in the image with a ~2.2 µm thick $MoSe_2$.

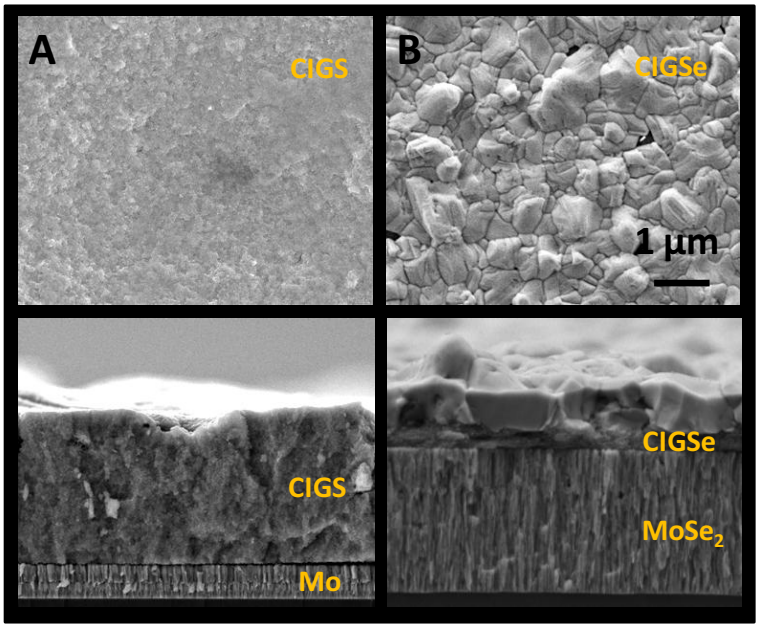

Figure 13. Top and cross-sectional SEM images from A) precursor CIGS spin coated films and B) selenized CIGS spin coated films.

Solar cells were then prepared using this thin absorber and thick $MoSe_2$ layer, by using the following sequence CdS/i-ZnO/ITO. Figure 14 depicts the PV performance of the best solar cell showing an efficiency of 4.8%. Large open circuit voltage V_{oc} of 410 mV and high short circuit current J_{sc} of 30.5 mA/cm^2 were obtained despite the not optimized thicknesses of both the absorber and $MoSe_2$.

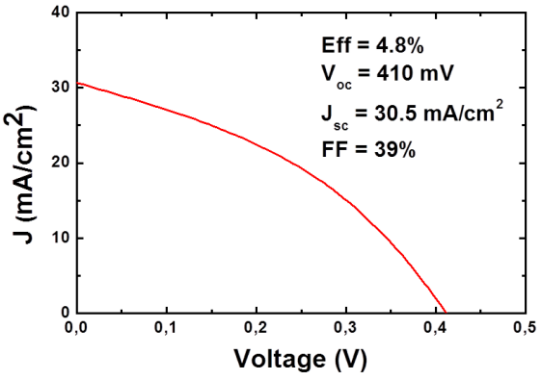

Figure 14. PV characteristics of CIGSe solar cells prepared from spin coated CIGS-$(NH_4)_2S$ thin films.

Several sets of solar cells were then prepared using this procedure, trying to optimize the thickness absorber, the Mo substrate and by using chemical solutions to etch possible

undesired phases. Figure 15 shows a comparison of solar cells prepared with different chemical etches of the absorber before the deposition of the CdS. It is interesting to note that using either KCN or $(NH_4)_2S$ allows achieving V_{oc} around 100 mV higher than without any etching. The beneficial effect of etching techniques could be related either to the effectively removal of undesired formed Cu phases at the surface and/or passivation of the surface.

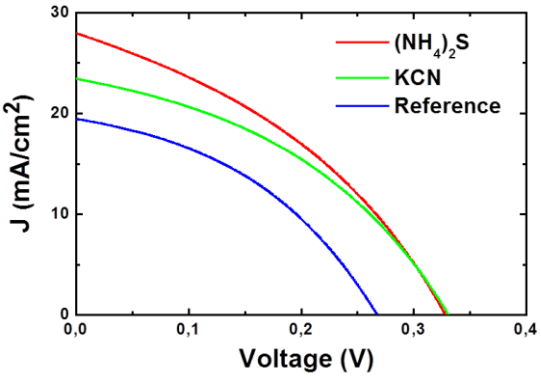

Figure 15. PV characteristics of CIGSe solar cells prepared from spin coated CIGS-$(NH_4)_2S$ thin films and treated with KCN and $(NH_4)_2S$ etching.

4.3 Conclusions

This chapter described the strategies that have been adopted for the development of solar grade CIGS thin films. This involved the use of wurtzite NPs instead of the chalcopyrite ones, and the optimization of the CIGS thin films deposition processes to produce smooth and highly homogeneous NP films using pulsed spray deposition. To obtain high quality films, short spray pulses, large enough times from pulse to pulse, substrate temperatures close to the solvent boiling point and inks with inorganic loads as high as possible were necessary.

Different strategies were also explored to optimize the sintering processes, including, ligand exchange strategies to remove organic carbon, induce grain growth by impurities doping and alternative annealing procedures. The use of crystallization promoters such as Sb, allows to fully crystalline the films at temperatures as low as 500°C. Additionally, the use of high annealing temperatures (575°C) and a Se sheet over the CIGS layer during the selenization produce high crystalline CIGSe thin films while avoiding the selenization of the

Mo layer. Moreover, it is proved that the introduction of Na impurities into the CIGS film by the incorporation of a Na salt into the CIGS NP ink increase CIGS grain growth. Finally, the selection of a suitable Mo substrate is mandatory to obtain high crystalline thin films. Accordingly, nanocrsytalline thin films require porous Mo substrate prepared by sputtering at high pressure in order to avoid complete selenization of the Mo layer and also to improve CIGS grain growth.

Finally, spin coating technique has been tested to prepare CIGS thin films from chalcopyrite CIGS NPs. The resulting CIGSe solar cells prepared from selenized CIGS thin films show higher PV performance. The increased efficiency obtained is mainly related to the smoother and homogeneous thin film precursor prepared by this technique. Thanks to this, the subsequent CdS deposition forms a better interface with CIGSe, which is translated in a improved PV performance.

5 Spray-deposited CZTSe Solar Cells

This chapter presents a synthetic route to prepare CZTS NP. Furthermore, these NP were used to prepare inks, which were printed into thin films by doctor blade or sprayed. The no need of vacuum and the processing at low temperatures of these techniques should represent a great reduction of the final cost of solar. A multi-strategy approach to overcome the main challenges of NP-based solution-processed CZTSe thin film solar cells is presented. We developed an efficient ligand exchange strategy to displace organic ligands from the surface of CZTS NP by inorganic salts, with which we are able to introduce dopants to further induce grain growth and enhance crystallization. After annealing the film in a Se-rich atmosphere, carbon-free and crystalline CZTSe absorber layers were obtained. CZTSe PV devices were fabricated and tested. This chapter also presents a procedure for the continuous production of CZTS NP with controlled composition.

5.1 Introduction

CZTS and CZTSe composed of abundant and low-toxicity elements are the main alternative to conventional absorber materials in thin film solar cells. CZTS and CZTSe thin films can be produced by conventional vacuum-based technologies, such as sputtering, evaporation or pulsed laser deposition. However these technologies are neither particularly low-cost nor versatile for the production of large area devices, because of the relatively high energies and controlled atmospheres they require and the low growth rates and material yields they have associated. Alternative low cost solution-processing methods allow the preparation of large area thin film semiconductors at low temperatures and at high production rates and yields. Unprecedentedly, for CZTS and CZTSe solar cells, solution-processing technologies have also achieved significantly higher device efficiencies than conventional vacuum-based technologies. [30,42,128] This improved performance is associated with the excellent compositional and phase control achieved by solution-based methods in such complex quaternary materials. [35,53,109,110,129,130,131]

Nevertheless, solution-based technologies are not without limitations. The main

challenges still encountered when producing large area thin films by solution-processing methods based on the deposition of NP are the following: The formation of cracks due to the high deposition rates and the volume reduction associated with the organics removal; the poor crystallinity of the as-deposited precursor films, which require a posterior thermal treatment; and the organics used during material synthesis and ink formulation and the residual carbon left after their thermal decomposition strongly deteriorate the film electronic properties and block its crystallization. A multi-strategy approach to overcome these limitations is presented here. We used a pulsed spray deposition system to produce CZTS films from colloidal CZTS NP having carefully adjusted compositions and organic free surfaces. Organic ligands used during NP synthesis were displaced by metal salts. We demonstrate here the effectiveness of these approaches to produce highly homogeneous, organic- and crack-free films.

A scale-up procedure derived from classical colloidal synthesis routes is also presented in this chapter. The required production amount is obtained by maintaining the synthetic conditions and concentrations optimized for small batches while increasing the total volume of solvent and thus the size of the reaction receptacle. This simple scale-up technique inevitably results in a degradation of the product homogeneity because of the reduced thermal and compositional uniformity of large volumes of solution, especially in the need of a hot injection step. Maximization of the solution homogeneity, in terms of composition and temperature, is key for producing nanomaterials with highly uniform and well-controlled characteristics. While a proper escalation of the homogenizing and heating mechanisms is indispensable, the heating and mixing volumes used also must be minimized because of the insufficient thermal and mass transport properties of the solvent. Thus, the natural scale-up procedure for obtaining large amounts of high-quality nanomaterials consist of using a very high frequency of identical and automated batch-to-batch events with relatively small volume batches. In the high-frequency limit, this procedure translates into an automated continuous-flow synthesis procedure. Several groups have developed microfluidic systems for continuous production of NPs. These previous works focused on the degree of control over the NP properties offered by this technology but ignored its scale-up potential.

[53,132,133,134] In spite of all its advantages, very few reports have been devoted to the large-scale synthesis of NP in macroscopic flow reactors. Among them, the synthesis of Ag NP, CdSe and SnTe nanorods in stainless steel reactors and in relatively thick polymeric (1/16 in) and silica glass capillaries (0.2−0.5 mm) should be mentioned, though authors referred to this last system as microfluidic.[134,135,136,137,138]

5.2 Results and Discussion

5.2.1 CZTS Nanocrystal Synthesis

CZTS NP for further solar cell fabrication were prepared by the reaction of Cu, Sn and Zn salts with tetra-ethylthiouram disulfide in the presence of ODPA and OLA. Composition could be tuned by changing the amount of precursors in the initial solution. A range between 0.75 and 1.75 mmol of Zn precursor was used to observe how this variation influences the final composition and structure. The amount of Zn increases and the amount of Cu decreases as the amount of Zn precursor is increased in the initial solution. XRD analysis confirmed that the crystal structure was not affected by modifying the composition (figure 1). Moreover, CZTSe solar cell efficiencies were obtained from Cu-poor and Zn-rich CZTSe. [30,42,128,139] Consequently, CZTS NP with composition of $Cu_{1.9}Zn_{1.1}Sn_{1.0}S_{4.0}$, as measured by EDX (figure 1), were used to study ligand exchange procedures, selenization processes and to fabricate CZTSe solar cells.

ZnO (mmol)	Cu / (Sn+ Zn)	Zn / Sn
0.75	1.15	0,32
1.25	1.05	0,81
1.35	1	1,02
1.40	0.90	1,02
1.45	0.75	1,03
1.60	0.7	1,38
1.70	0.6	1,54

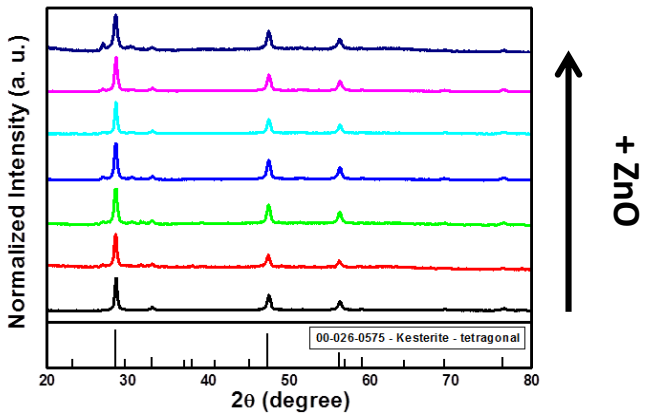

Figure 1. Composition and precursor concentration of the CZTS NP and XRD patterns of CZTS NPs (JCPDS no. 00-026-0575) prepared with different amounts of ZnO in the precursor solution.

Figure 2 shows representative TEM and HR-TEM micrographs of the ~ 25 ± 5 nm CZTS NP produced by colloidal synthesis. After purification, NPs were still stable in chloroform.

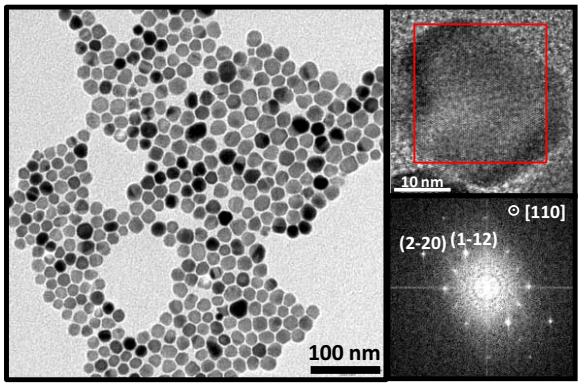

Figure 2. TEM and HR-TEM micrograph, and power spectrum analysis of CZTS NPs.

The optoelectronic behavior of the films was assessed from the transmittance measurements. The spectra were processed following the Tauc formalism: [140]

$$\alpha h\upsilon = A(h\upsilon - E_g)^{1/2}$$

where α is the absorption coefficient, A is a constant dependent on each transition and E_g the band gap energy for a direct transition between parabolic bands. A $(\alpha h\nu)^2$ vs $(h\nu)$ plot gives the band gap value upon extrapolation at $(\alpha h\nu)^2 = 0$ of the linear section of the plot. Optical transmittance of CZTS NP was measured in the range 400–2500 nm using the UV-VIS-NIR spectrophotometer. There is an absorption edge around 1500 nm (≈0.825 eV), which is translated in a 1.5 eV band gap (figure 3).

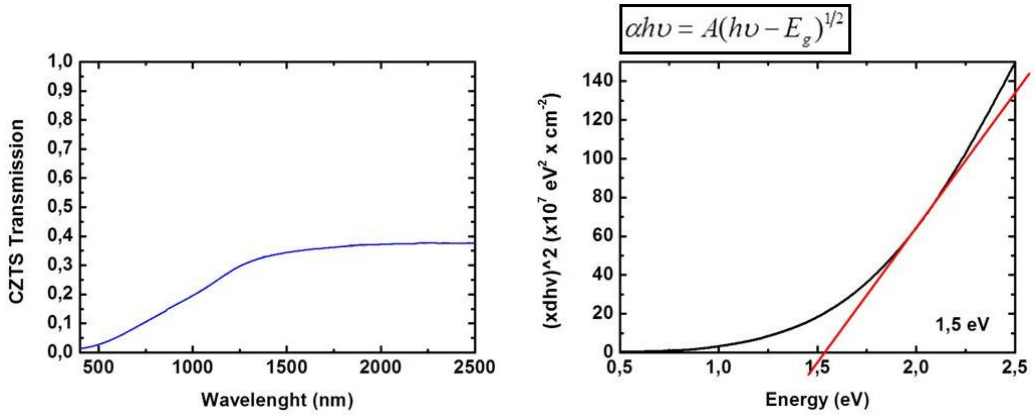

Figure 3. Band gap extracted from CZTS NPs transmittance.

5.2.2 CZTS Nanocrystals Continuous Production

The continuous production was used for the preparation of grams of this material with controlled composition under open-air conditions. A representative TEM image of the CZTS NP produced at 300℃ and a flow rate of 2.0 mL/min is shown in Figure 4. While the NP size distribution was fairly narrow, full shape and size control is still not available by this method for such complex quaternary materials. In the inset, a HR-TEM image of a few selected particles and a selected-area electron diffraction image of a single NP are also displayed to show the crystallinity of the obtained products.

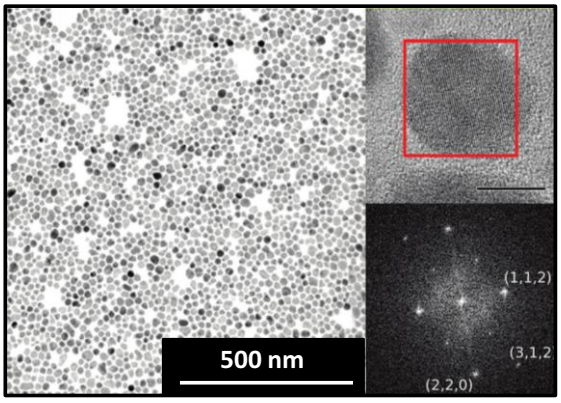

Figure 4. TEM micrograph of cleaned CZTS NPs prepared inside the flow reactor at 300℃. The inset shows an HRTEM image of a CZTS NP and the corresponding SAED pattern.

XRD patterns and Raman spectra of the NP before and after a sintering treatment at 500℃ (Figure 5) confirmed the crystallographic structure of the NP to be compatible with that of CZTS (JCPDS no. 00-026-0575; tetragonal kesterite). CZTS typically crystallizes in a kesterite-type structure (space group $I\bar{4}2m$) with two tetrahedral structural units, [Cu_2S] and [$SnZnS_4$], although CZTS with a wurzite-type crystal structure has been reported. [141,142] This structure can be derived from zinc blende ZnS by partial substitution of Zn with Cu and Sn. [23] The Raman peaks at 336 and 287 cm^{-1} are the main features of the kesterite-type structure, as previously reported for CZTS. [143]

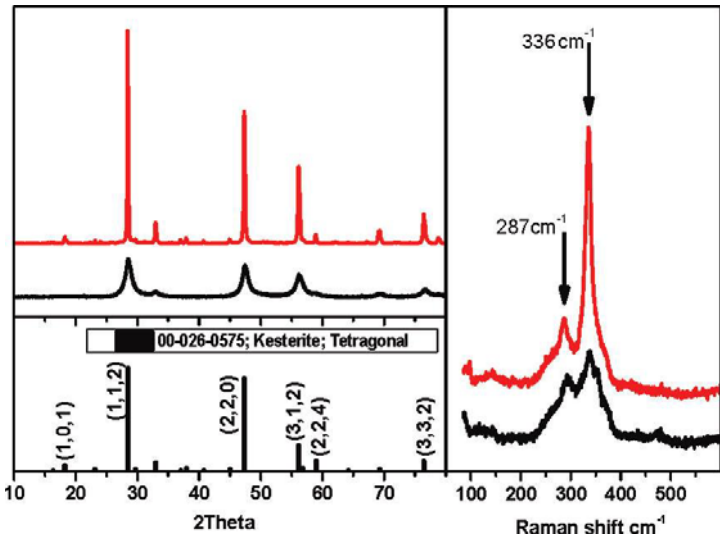

Figure 5. (left) XRD patterns and (right) Raman spectra of the prepared NP before (black) and after (red) annealing at 500°C for 1 h. As a reference, the diffraction pattern of CZTS (JCPDS no. 00-026-0575) is shown. The lattice parameters for the heated sample were a = b = 5.40 Å and c = 10.40 Å.

The materials composition was analyzed by SEM-EDX. Quite conveniently, the different reaction kinetics of Cu, Zn, and Sn with S allowed us to control the NP composition over a relatively wide range by appropriately adjusting the precursor concentrations, the reaction temperature and time and the flow rate. Figure 6 shows how the NP composition depends on the synthesis conditions. In particular, increasing the flow rate of the solution through the reactor afforded NP with higher Cu content. From our results, it became evident that the kinetics of the reaction of each element with the sulfur precursor is the fastest for Cu and the slowest for Zn. We believe that initially Cu_2S NP may nucleate, while first Sn ions and then Zn gradually enter into the NP structure as the solution advances inside the reaction tube. Lower reaction temperatures extended the time spread needed for the complete incorporation of Zn and Sn ions inside the CZTS crystal structure, thus reducing the possible flow rates available for the formation of stoichiometric NP.

It is worth mentioning that although quite a broad range of CZTS compositions were accessible by this procedure, only compositions close to the stoichiometric one were stable after annealing treatments above 500°C, confirming the narrow stability spot of the CZTS phase. [144] Phase segregation was observed during the annealing treatment for NPs with

compositions far from the stoichiometric one. Figure 7 show XRD measurements confirming the phase segregation.

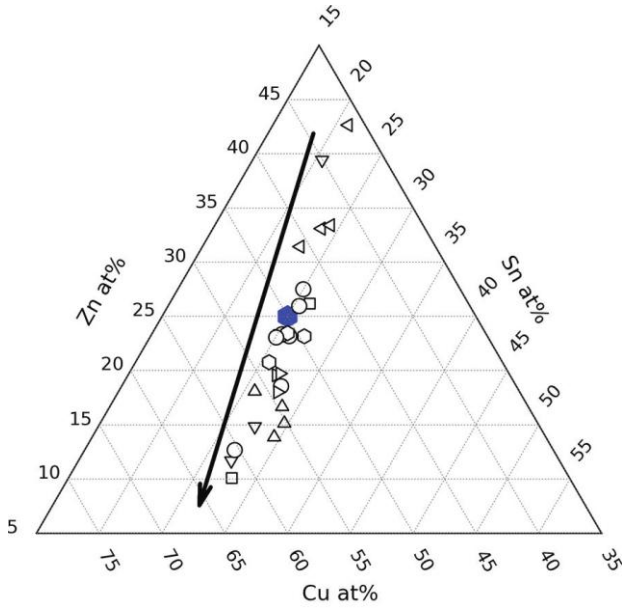

Figure 6. CZTS cationic ratios obtained from SEM–EDX. The arrow points the direction of increasing flow rate. Different symbols denote different reaction conditions.

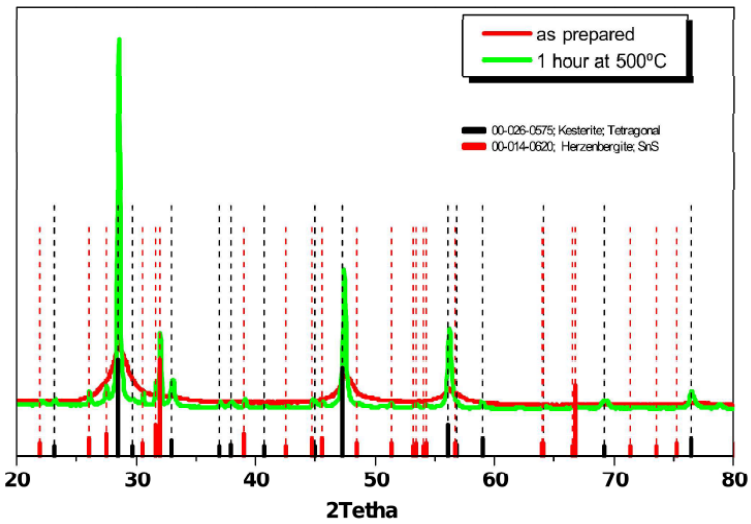

Figure 7. XRD spectrum of the prepared tin-rich CZTS NP before (red) and after (black) annealing at 500°C during 1 hour. As a reference, the diffraction pattern of CZTS (JCPD: 00-026- 0575) and SnS (JCPD: 00-014-0520) are shown.

Single-particle HRTEM−EDX analysis confirmed that all of the NPs contained all four elements. However, these analyses also demonstrated the existence of a distribution of NP compositions within each sample. In this regard, while the average composition of a sample of CZTSe NPs produced at relatively low temperature (230℃) by a heating-up procedure was close to the stoichiometric one, large particle-to-particle compositional variations existed. [145] Figure 8 shows the compositions of several single CZTS NPs prepared at 315℃. It was experimentally observed that the NP composition distribution was strongly dependent on the reaction temperature; the lower the reaction temperature, the broader the NP composition distribution within each sample. As an example, samples prepared at 300℃ showed much larger particle-to-particle compositional differences than those obtained at 315℃, which showed fairly good composition homogeneity (figure 9). Notably, no particle with elemental, binary, or ternary composition was found among the several tens of particles checked within each sample.

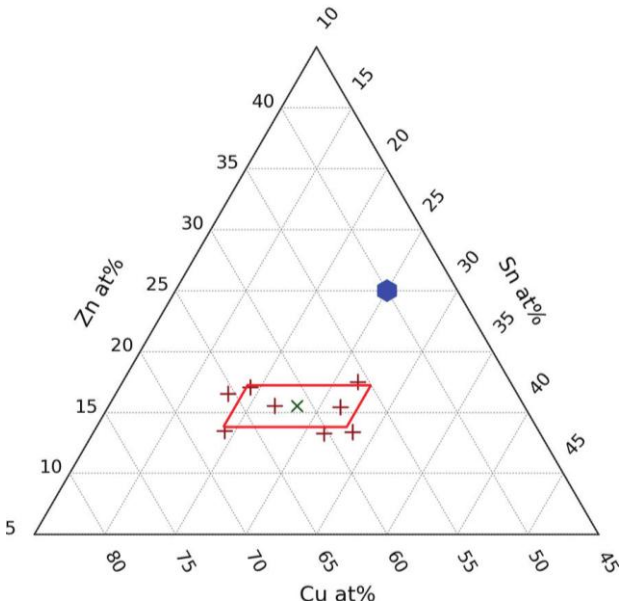

Figure 8. Single-particle composition (red +) obtained by HR-TEM−EDX analysis of a number of CZTS NPs synthesized at 315℃. The green x shows the mean composition obtained by averaging the values obtained from several NP. The blue hexagon in each graph shows the nominal composition of the precursor solution.

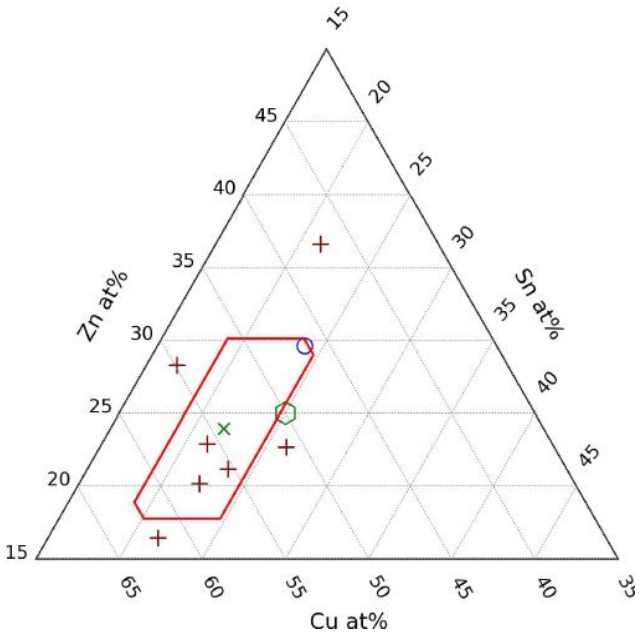

Figure 9. Single particle composition (red crosses) obtained by TEM-EDX of a number of CZTS NP synthesized at 300℃. The green cross shows the mean composition obtained by averaging the values obtained from the single particle analysis. The blue open circle denotes the composition obtained by SEM-EDX. The blue hexagon points the nominal concentration of each element in the precursor solution.

5.2.3 CZTS Nanocrystal Ligand Exchange

We believe OLA controls the NP growth and its stability. On the other hand, ODPA allows a better control of composition by coordinating with the precursor salts and facilitating their incorporation into the final crystal structure. ODPA does not remain attached to the NP surface, thus it was easily removed during the purification process and only OLA remained as organic impurity. Even when organic ligands can be decomposed by an annealing process, their carbon footprint still limits the device performance and blocks the crystal growth. [146] Furthermore, cracks are usually formed when removing organics after deposition. Therefore, to produce solar cell grade thin films, organics need to be displaced from the NP surface before deposition. However, to process the materials in solution and to obtain homogeneous films, NP need to be soluble in a liquid carrier. Thus, either we use thick solvents and binders that keep NP dispersed during long enough times, which will again leave large amounts of carbon after decomposition, or we replace the organic ligands used

during the synthesis by shorter but still effective stabilizers. [60,101] In this last direction, inorganic salts are excellent candidates to displace organic ligands and render the NP soluble in low boiling point solvents that after deposition can be easily evaporated without a carbon footprint.

The use of inorganic salts gives also the opportunity to tune the final film composition or to introduce external dopants that control the material electronic properties. [147] Solutions of $(NH_4)_2S$, NaCl, NaN_3 and KOH were used as ligands. Also solutions of $SnCl_4$, $ZnCl_2$ and CuCl were used in order to avoid introducing different elements to the CZTS structure. The ligand exchange process was characterized by EA of carbon and TGA in order to quantify the amount of carbon removed (figure 10). EA gives us the percentage of carbon present in the sample by a combustion analysis. The sample is burned in presence of oxygen which results in different products measurable by their mass, allowing calculating the amount of the desired element present in our sample. In the TGA analysis CZTS powder is heated in a nitrogen flow from 30 to 500°C, and maintained at that temperature during 1 hour. At this temperature all the organic carbon should be eliminated. The EA results confirmed that we removed a large part of the organic carbon from the NPs, from the 2.9 % before ligand exchange to values below 1 % after ligand exchange. These results were confirmed by TGA observing a reduction of weight of a 14 % before ligand exchange and between 1 and 2 % after ligand exchange. Additionally, XRD measurment confirmed that there was no change in the structure after the ligand exchange with any ligand exchange agent (figure 11).

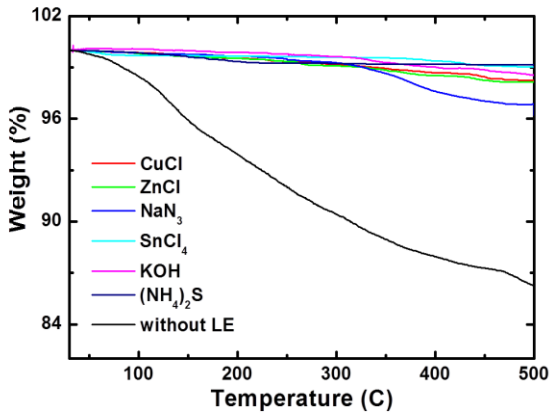

Ligand Exchange	% Carbon E A
CuCl	0.71
$ZnCl_2$	0.75
NaN_3	1.27
$SnCl_4$	0.81
KOH	0.74
$(NH_4)_2S$	0.9
NO LE	2.93

Figure 10. TGA analysis and carbon EA of CZTS NPs with different surface ligands.

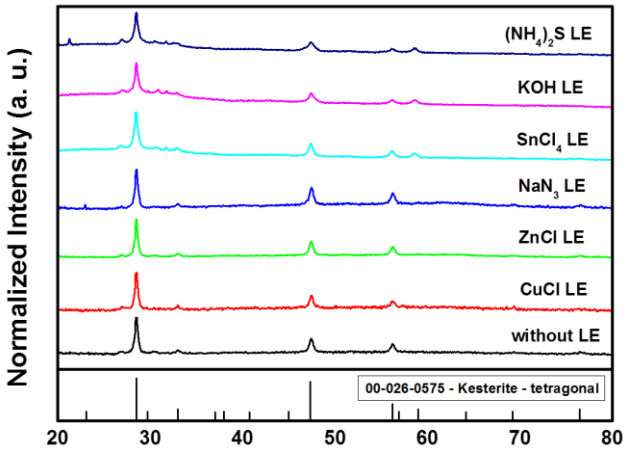

Figure 11. XRD patterns of CZTS NPs with different surface ligands.

$CuCl_2$, $ZnCl_2$ and $SnCl_4$ were also tested as inorganic ligand exchange agents. One initial idea was to tune the composition of the final film through the ligand displacement agent. However, while the replacement of organic ligands by those salts was successful and carbon removal was accomplished, the precise control of the amount of added ions was challenging and the formation of secondary phases with the annealing treatment was an important drawback. Thus, we concluded that the tuning of the material composition was more efficiently performed during the NP synthesis. Moreover, the introduction of Cu, Zn or Sn did not promote the crystal domain growth of the corresponding thin films, after selenization in standard conditions (550°C, Se/Sn rich atmospheres), as observed in figure 12. While we chose to control the film composition at the NP synthesis stage, we tested multiple ligand exchange agents looking for the one that did not change the film composition but helped its crystallization. Among the different salts tested, best results were obtained for $SbCl_3$.

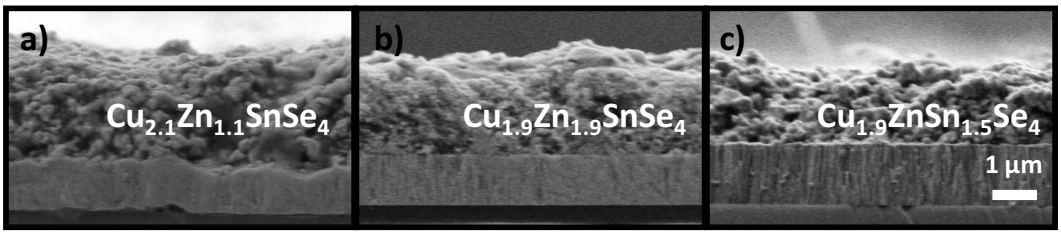

Figure 12. SEM cross-sectional images and EDX data from CZTSe thin prepared from the selenization at 550°C of CZTS NPs after $CuCl_2$ ligand exchange (a), $ZnCl_2$ ligand exchange (b) and $SnCl_4$ ligand exchange.

OLA displacement with $SbCl_3$ was carried out using a bi-phase system explained in the chapter 3. As a reference, we also replaced OLA with a relatively more conventional specie, $(NH_4)_2S$, using a similar procedure. Figure 13a shows the mass loss as a function of temperature for CZTS-OLA, CZTS-$SbCl_3$ and CZTS-$(NH_4)_2S$ NPs. A relative mass decrease of a 3 % was measured for purified CZTS-OLA NPs when heated to 450°C under a nitrogen flow. On the other hand, after $(NH_4)_2S$ and $SbCl_3$ ligand exchange, NPs showed a mass loss of less than 1 % associated to the evaporation of S, Sb and probably Sn. The higher mass loss measured for CZTS-OLA NPs was consistent with the thermal decomposition of the bulky OLA molecules, which were not present at the surface of CZTS-$SbCl_3$ and CZTS-$(NH_4)_2S$ NPs. Figure 13b shows the ATR-FTIR spectra of dried CZTS-OLA, CZTS-$SbCl_3$ and CZTS-$(NH_4)_2S$ NPs. The CZTS-OLA spectrum showed the C-H vibration modes in the high-frequency region (2800-3000 cm^{-1}) characteristic of OLA. This feature disappeared from the CZTS-$SbCl_3$ and CZTS-$(NH_4)_2S$ spectra.

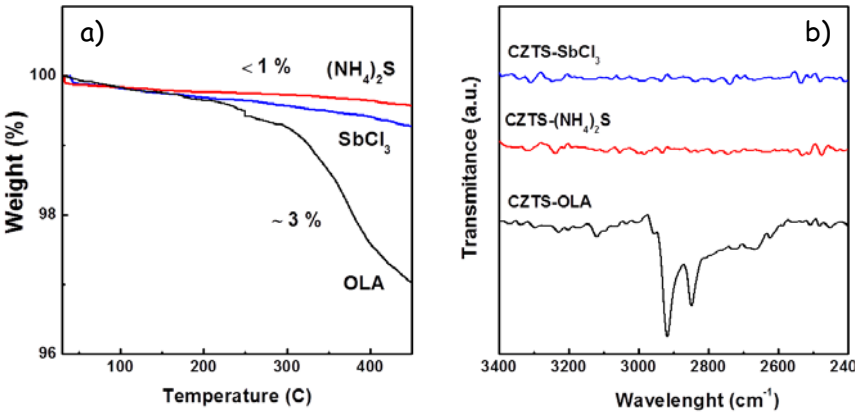

Figure 13. a) TGA analysis and b) ATR-FTIR spectra from CZTS-OLA, CZTS-$SbCl_3$ and CZTS-$(NH_4)_2S$ NPs.

The carbon left after annealing CZTS NPs in a nitrogen atmosphere was measured by CHN quantitative EA. A 3 % of carbon was obtained from the analysis of annealed CZTS-OLA NPs. On the other hand, the carbon percentage measured from annealed CZTS-$SbCl_3$ and CZTS-$(NH_4)_2S$ NPs was below the detection limit of our system: ~ 0.1 %. After organic ligand displacement and purification, CZTS-$SbCl_3$ and CZTS-$(NH_4)_2S$ NPs were stable in solution during times long enough to allow their deposition. Subsequent studies will test the $SbCl_3$ influence on CZTS structure and morphology before and after thermal treatments. CZTS-

$(NH_4)_2S$ and CZTS-OLA thin films are used as references.

5.2.4 Printing of CZTS Thin Films

Initially, CZTS thin films were prepared by the doctor blade technique. One of the main problems in the preparation of thin films of CZTS by printing techniques is the presence of cracks after high temperatures treatments. According to this, the study of the ink composition has been done as we believe that is one of the critical points. The amount of organic solvent and binder was varied in order to find the proper ink composition to avoid crack formation. Figure 14 show the interferometer images from dried CZTS films, where is possible to see that CZTS layers prepared with ink composition 3, 4, 7 and 8 shows cracks even before any annealing treatment.

Sample	1	2	3	4	5	6	7	8
CZTS (g)	0.1	0.1	0.1	0.1	0.1	0.1	0.1	0.1
Org. Solvent (g)	0.75	1	1.25	1.5	0.5	0.5	0.5	0.5
Binder (g)	0.17	0.22	0.25	0.32	0.2	0.3	0.4	0.5

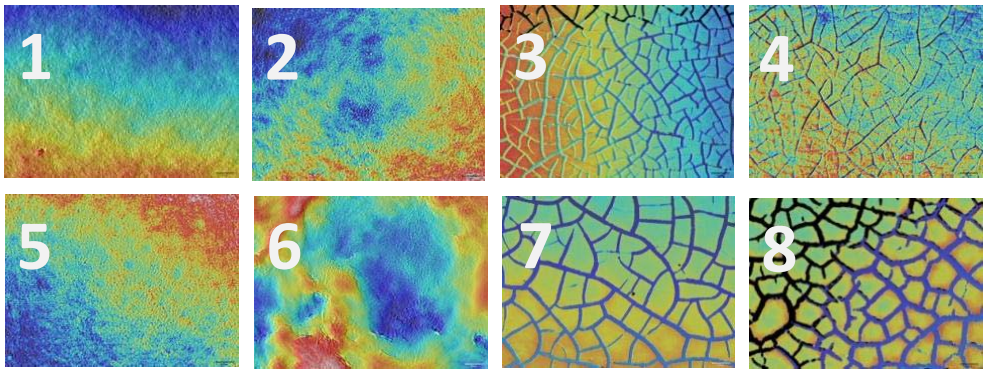

Figure 14. Interferometer images from CZTS thin films printed from CZTS inks with different amounts of organic solvent and binder.

As shown in the composition table from figure 14, as much organic solvent or binder was added, more cracks were observed. This is consistent with the fact that the organic solvent will be removed as the film is dried, leading to surface defects and crack formation. Further selenization treatments were performed from printed CZTS films (550℃ for 1h in a Se/Sn rich atmosphere). As show in figure 15, cracks are still present after high temperature

treatments. Additionally, it was not possible to obtain highly crystalline layers. A typical bi-layer formed by a crystalline top film and a bottom thick nanocrystalline layer (figure 16). In conclusion, we decided to look for alternative film deposition techniques, which not require additional organic compounds for NP ink formulation. Accordingly, spray deposition was selected as a suitable technique to prepare NP thin films.

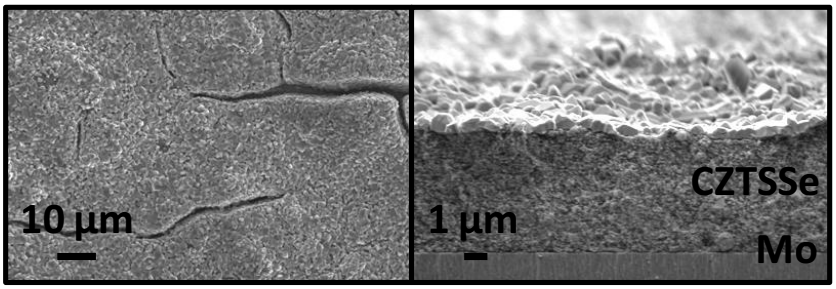

Figure 15. Top and cross-section SEM images of a selenized CZTS printed thin film.

5.2.5 Spray Deposition of CZTS Thin Films

An automated pulsed spray-deposition system was used to deposit the NPs into homogeneous and crack-free films with controlled thickness. The optimized process to produce homogeneous 4 µm-thick CZTS films were 40 cycles of 0.5 s pulses with a pulse-to-pulse time of 60 s, and a substrate temperature of 160℃. For the crystallization analysis and to fabricate solar cells, CZTS NPs were sprayed onto 2x2 cm^2 Mo-coated SLG substrates in air from a 5 g/L CZTS solution in DMF. Crack free and smooth surfaces were obtained as observed in figure 16.

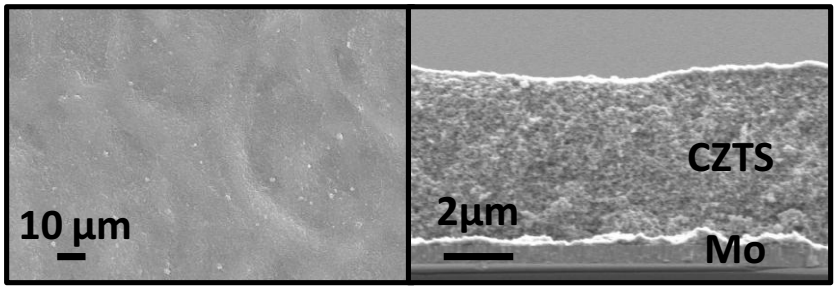

Figure 16. Top and cross-section SEM images of spray deposited CZTS thin film.

5.2.6 Selenization of CZTS Thin Films

A necessary thermal treatment of the precursor thin film is required in order to obtain suitable high density, compact and crystalline film to be implemented in a subsequent PV device. A major inconvenient of kesterite material is its thermal instability. At high temperatures, CZTS decomposes in its metal binaries, as shown in reaction 1. Particularly, the loss of Sn is reported by many groups, mainly by evaporation of SnS (g). [148] The decomposition starts when S is lost in form of S (g). Afterwards, the low S pressure leads to desorption of SnS (s). The chalcogen changes the oxidation state of Sn from (IV) to (II), which converts the Sn present in the CZTS to surface SnS (s). The binary SnS (s) is very volatile and is evaporated (reaction 2). As both reactions are reversible, the addition of Sn and S during the thermal treatment would equilibrate partial pressures, and the binary metal salts would reconvert to CZTS. [149,150]

$$Cu_2ZnSnS_4\ (s) \leftrightarrow Cu_2S\ (s) + ZnS\ (s) + SnS\ (s) + 1/2\ S_2\ (g)\ \text{(reaction 1)}\ ^{150}$$

$$SnS\ (s) \leftrightarrow SnS\ (g)\ \text{(reaction 2)}\ ^{150}$$

CZTS stability was assessed by annealing sprayed CZTS-$(NH_4)_2S$ thin films under different conditions. Figure 17 presents XRD patterns and raman spectra of CZTS samples before and after annealing at 600℃ with (10-25 mg) and without SnS_2. No crystalline phase was detected by XRD and raman for the samples annealed without SnS_2. In contrary, when SnS_2 was added, very crystalline films with kesterite structure were observed.

From this point, all the CZTS films were annealed in the presence of Sn and S or Se. The use of pure sulfide CZTS NPs and a selenization procedure allows us to control the amount of selenium we want to introduce to the final CZTS material, by varying the amount of selenium that we introduce into the graphite box during the annealing treatment. Thanks to that, we can control the S/Se ratio, which allows us to tune the band gap from 1.5 ev (CZTS) to 1 ev (CZTSe). That variation gives us the possibility to work with a PV absorber range similar to chalcopyrites. Additionally, the chalcogen exchange from S to Se, lead to an enhanced crystallization. [61,87]

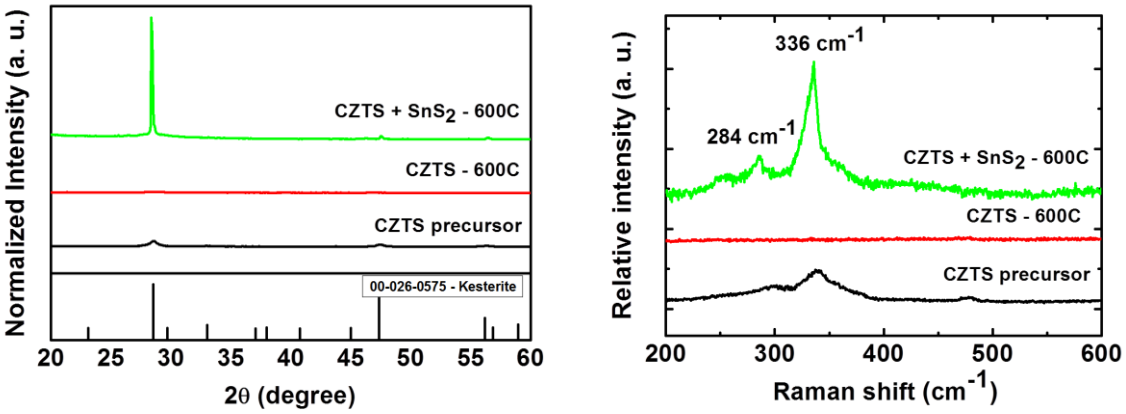

Figure 17. XRD patterns and Raman spectra of as-deposited and 600°C sulfurized, films prepared from CZTS-OLA NP (in presence and absence of SnS_2).

Once the proper annealing conditions were selected, we are able to study the structure of CZTS-OLA, CZTS-$SbCl_3$ and CZTS-$(NH_4)_2S$ sprayed thin films. XRD and raman spectra were taken from CZTS-OLA, CZTS-$SbCl_3$ and CZTS-$(NH_4)_2S$ films before and after selenization. To produce solar cell grade layers, CZTS films were annealed for 60 min in a Se and Sn-rich atmosphere. A complete substitution of S by Se took place during selenization, transforming the precursor kesterite CZTS film (JCPDS 00-026-0575, figure 18a) into kesterite CZTSe (JCPDS 01-070-8930, figure 18b). A partial selenization of the Mo bottom layer was also observed. Raman spectra were measured with 514.5 nm excitation wavelength having a penetration depth of backscattered light below 100 nm (figures 18c, 18d). The precursor film exhibited the typical Raman spectrum of CZTS nanocrystalline layers with broad peaks (FWHM of 13-14 cm^{-1}) at 288 and 336 cm^{-1} and a shoulder at 374 cm^{-1} corresponding to the two main A symmetry modes and likely to a B symmetry mode of the CZTS kesterite structure. [33,151,152,153,154,155] After annealing, and independently of the ligand, the crystalline quality of the films was largely improved (FWHM of main A peak= 5.5-6.5 cm^{-1}). CZTSe films showed a peak at 173 cm^{-1} which has been recently attributed to two A modes, the main A mode at 197 cm^{-1}, and two weaker peaks at around 233 cm^{-1} related to E/B symmetry modes. [33,151,152,153,154] No secondary phases were detected by either XRD or Raman measurements. Raman characterization using UV excitation (λ=325 nm) also discarded the presence of ZnS.

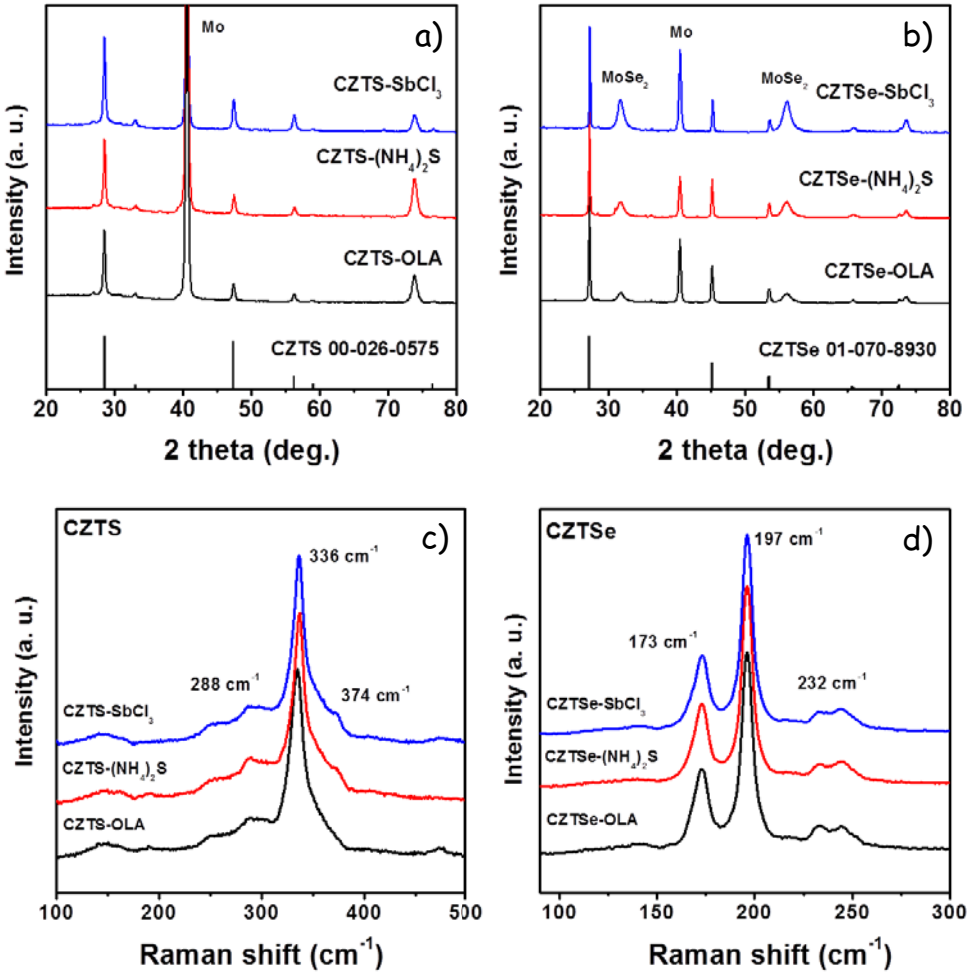

Figure 18. XRD patterns (a,b) and Raman spectra (c,d) of as-deposited (a,c) and 550°C selenized (b,d) films prepared from CZTS-OLA, CZTS-$SbCl_3$ and CZTS-$(NH_4)_2S$ NPs.

Figure 19 shows cross-sectional SEM images of the precursor films and the films selenized at different temperatures, from 475°C to 575°C. Absorbers crystallized from CZTS-OLA and CZTS-$(NH_4)_2S$ films exhibited a typical bi-layer structure formed by a bottom layer with fine grains and a top layer with larger crystals. Conversely, the absorbers crystallized from CZTS-$SbCl_3$ NPs showed a single layer structure with large crystals covering from the substrate to the surface. Films obtained from CZTS-$SbCl_3$ NPs systematically showed significantly larger crystal domain sizes than the ones produced from CZTS-$(NH_4)_2S$ and CZTS-OLA NPs and even at temperatures below 500°C relatively large crystal domains, in the micrometer range, were obtained.

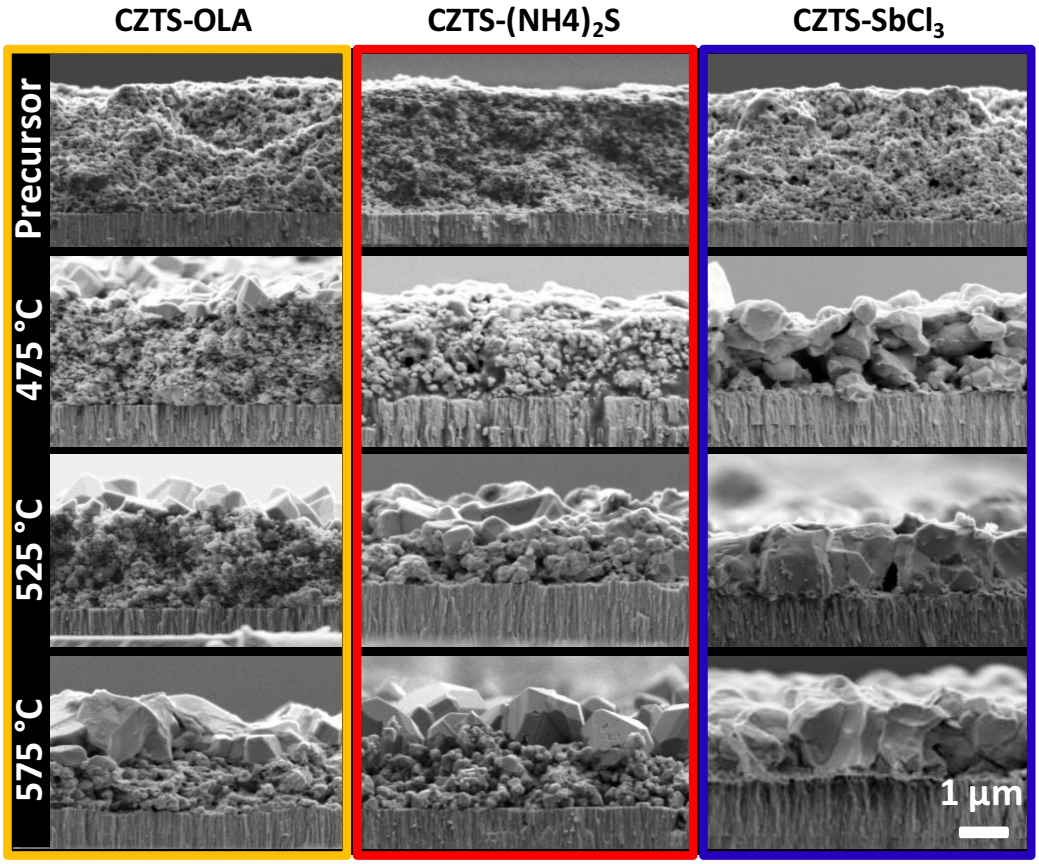

Figure 19. Cross-sectional SEM images of CZTS precursor and CZTSe films prepared from CZTS-OLA, CZTS-$SbCl_3$ and CZTS-$(NH_4)_2S$ NPs and annealed at temperatures from 475°C to 575°C.

Surprisingly, no Sb was detected after crystallization at temperatures above 500°C. No peak shift or additional band was observed in the Raman spectra or the XRD patterns and no Sb was detected in the composition analysis performed by EDX, ICP and XPS. EDX and ICP analyses showed the films to be copper-poor and zinc-rich, conserving the NPs composition, both before (Cu/(Zn+Sn)=0.85 & Zn/Sn=1.09) and after crystallization (Cu/(Zn+Sn)=0.81 & Zn/Sn=1.01). Additionally, EDX showed an Sb content of about 5 % for the CZTS-$SbCl_3$ thin films before selenization, but no Sb was detected on the CZTSe-$SbCl_3$ films after the heat treatment. ICP analyses showed an 8 % by mass of Sb in the CZTS-$SbCl_3$ film before selenization, but no Sb after selenitzation. As-deposited CZTS-$SbCl_3$ films showed intense XPS Sb $3d_{5/2}$ and $3d_{3/2}$ peaks, corresponding to an atomic 20 % Sb composition, but the crystallized CZTSe-$SbCl_3$ films showed no Sb-related peak (figure 20). Just an oxygen peak corresponding to a slight surface oxidation of the materials was detected by XPS in the

crystallized but air exposed layers (figure 20). These results suggest that Sb did not incorporate to the bulk CZTSe crystals but it evaporated during the selenization process. XPS analysis showed no Sb on the NPs surface after selenization. Before selenization relatively intense Sb3d bands were measured by XPS. The Sb concentration calculated from the XPS spectra was an atomic 20 %. Thus we conclude that a high quantity of Sb was introduced in the material surface during the ligand exchange process. EDX analysis before selenization showed the Sb concentration before selenization to be approximately a 5 %. Taking into account the NP size (~20 nm), this corresponds to approximately 1 atom of Sb for every 2.7 atoms on the surface of CZTS. This is consistent with the XPS results taking into account that XPS probes just the first 2-3 nm from the surface. Differences between XPS and EDX results point towards a complete localization of the Sb at the particle surface. XPS and EDX results are also consistent with a complete coverage of Sb ions probably bond to surface S sites.

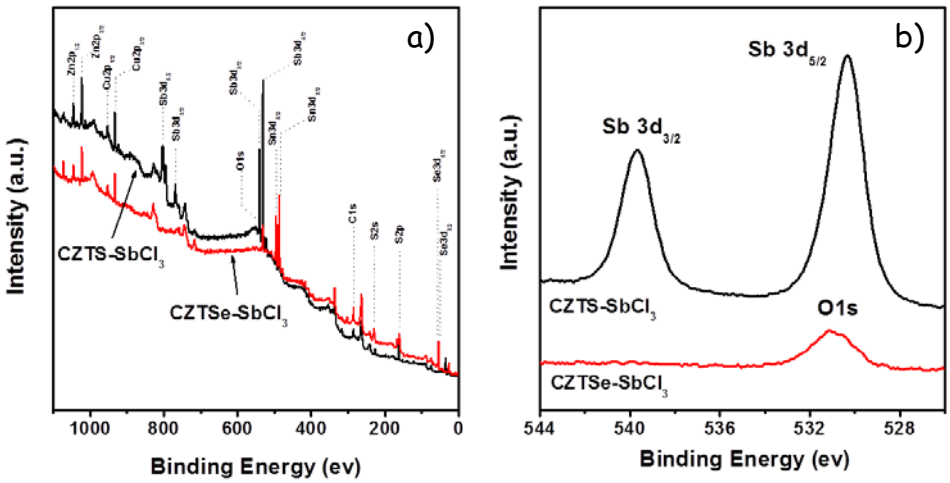

Figure 20. XPS spectra of a precursor CZTS-$SbCl_3$ film and of a CZTSe-$SbCl_3$ film selenized at 550°C.

The use of Sb to promote crystal growth in Cu(In,Ga)Se_2 films was previously reported, but its role remains unclear. [89,90,156] We hypothesize that Sb incorporated to the CZTSe structure at the crystal surface locally forming a low melting point Sb-based chalcogenide. Various are the Sb-containing compounds with diamond-like phases that could be locally formed, e.g. Cu_3SbSe_4 with a melting temperatures of 425℃ or even the quinary phase $CuZnSn_2Sb_3Se$, although none of these were detected by XRD or Raman. [157,158] Even in a sub-stoichiometric ratio, the incorporation of Sb to the crystal structure could locally reduce the

material's melting point, increasing its ionic mobility and its capacity for mass transfer and reorganization. We believe the decrease of the ion diffusion energy associated with Sb chemical incorporation ultimately promoted the diffusion-controlled crystallization process. As crystals domains grew, Sb was displaced to their surface where it accumulated. As crystallization proceeded, Sb evaporated and after 1 h at temperatures above 500℃, no Sb was left within the CZTSe film.

As commented before, Zn-rich CZTS precursors are required in order to prepare high efficient kesterite solar cells. [30,159] It is reported that Zn-rich conditions are necessary in order to avoid the formation of ternary phases, such as $Cu_2Sn(S,Se)_3$, with which the V_{oc} is limited as a consequence of its low bandgap, 0.84 eV and also to improve the p-type conductivity. [160] Nevertheless, the Zn excess would conduct to the formation of other secondary phases such as Zn(S,Se), which could be removed by selective etching techniques. [139,161] While, Zn-rich (Zn/Sn=1.2) CZTS NPs were first used as standard precursor, it was interesting to assess the influence in the final selenized film by using even more Zn-rich (Zn/Sn=1.4) CZTS NP. After selenization of Zn/Sn=1.4 CZTS-$SbCl_3$ sprayed thin films, it was observed that bigger crystals and more compact surfaces were obtained compared to the standard CZTSe thin films (figure 21). However, as shown in figure 21b and 21c, small grains of ZnSe, confirmed by EDX, were formed in the surface and in the back region. As measured by EDX, even high Zn content precursor NP was used, the bulk CZTSe film after selenization show an optimal composition of Zn/Sn=1.2, meaning that the rest of the Zn is present in form of ZnSe. While the excess of Zn improved the crystallization, it was responsible of the ZnSe formation. The presence of ZnSe in the CZTSe surface would degrade PV performance by minimizing J_{sc} and V_{oc}, as a consequence of a bad ohmic contact between the CZTSe and the CdS buffer layer. Although, selective chemical etchings were performed in order to successfully remove surface ZnSe grains, no PV behavior was observed from the devices prepared with this absorber. This result confirms that only a narrow range of compositions are suitable to prepare efficient kesterite PV devices. [143]

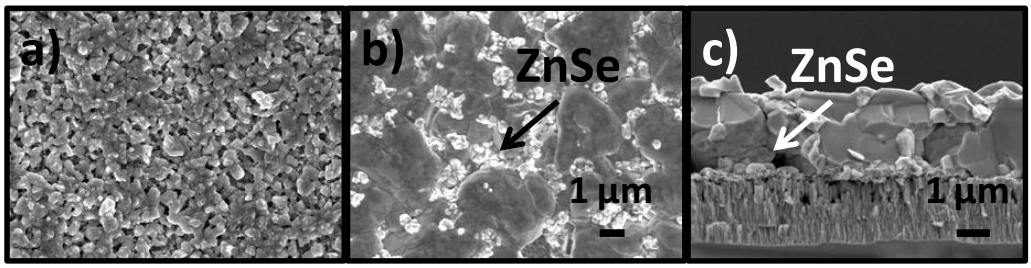

Figure 21. Top SEM images of selenized zin rich CZTS precursors with different Zn content a) Zn/Sn=1.2 and b) Zn/Sn=1.4 and c) the corresponding cross-sectional SEM image of sample b).

5.2.7 CZTSe Photovoltaic Performance

Kesterites with a high selenium content are more easily n-type doped than pure sulfide kesterites. [162] The presence of an n-type region on the surface of the p-type absorber favors the electron hole separation of photo-generated carriers. The resulting n-type doping is beneficial to form a proper inverted surface and decrease the recombination that takes place in the CZTSe/CdS interface. Additionally, is expected that the n-type doped selenium rich CZTSSe, present an improved carrier collection efficiency at longer wavelengths compared with pure sulfide kesterites, which is finally translated into better device performances. [163]

In order to confirm previous suggestions CZTS and CZTSe devices were tested. The pure sulfide CZTS, was prepared by annealing the sprayed CZTS-$SbCl_3$ precursor thin film in a S/Sn rich atmosphere at 550℃, during 1 h, inside a graphite box. CZTSe was obtained after selenization of CZTS-$SbCl_3$ precursor in a Se/Sn rich atmosphere in the same temperature and time conditions. As shown in cross-sectional SEM images from figure 22, bigger crystals and more compact films were obtained by selenization of CZTS-$SbCl_3$. However, a thick $MoSe_2$ was formed in the back contact, which could be detrimental for the PV performance as commented in previous chapters, affecting the CZTSe film adhesion and the ohmic nature of the back contact. No MoS_2 is observed in the sulfurized CZTS-$SbCl_3$ film. A better PV performance is confirmed for CZTSe solar cells. [163] CZTS show higher V_{oc} and lower J_{sc}, due to its larger Eg and to the lower carrier collection at higher wave-lengths respectivelly. However, higher efficiencies were obtained from CZTSe PV devices (figure 23). From this point it was decided to work with Se rich CZTS samples.

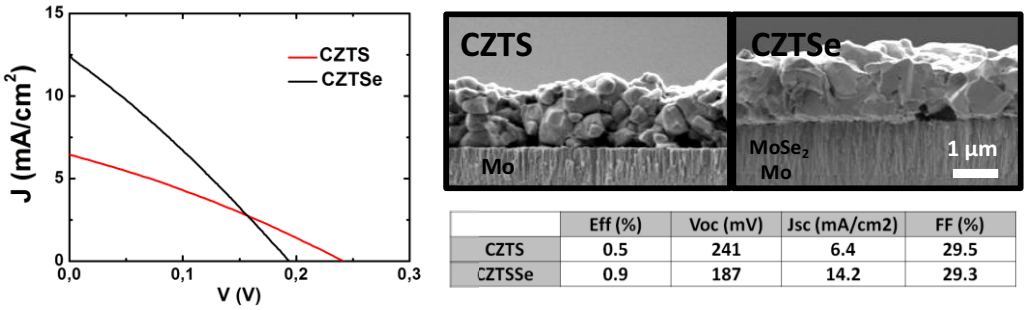

	Eff (%)	Voc (mV)	Jsc (mA/cm2)	FF (%)
CZTS	0.5	241	6.4	29.5
CZTSSe	0.9	187	14.2	29.3

Figure 22. I-V curves and PV parameters of CZTS and CZTSe devices.

Next study was to analyze the influence of the temperature in the absorber film morphology and its subsequent PV performance. Figure 23 shows the CZTS-$SbCl_3$ crystal growth evolution with selenization temperature (60 min) and its characteristic J-V curve obtained under AM1.5 illumination. While the J_{sc} was almost doubled by from 11 to 21 mA/cm^2, the V_{oc} and the FF was dramatically increased from 50 to 188 mV and 26 to 37 % respectively. The better crystal growth, observed at high selenization temperature, is translated into an improved interface contact between the absorber and the CdS buffer layer, minimizing recombination losses and thus enhancing its FF and efficiency.

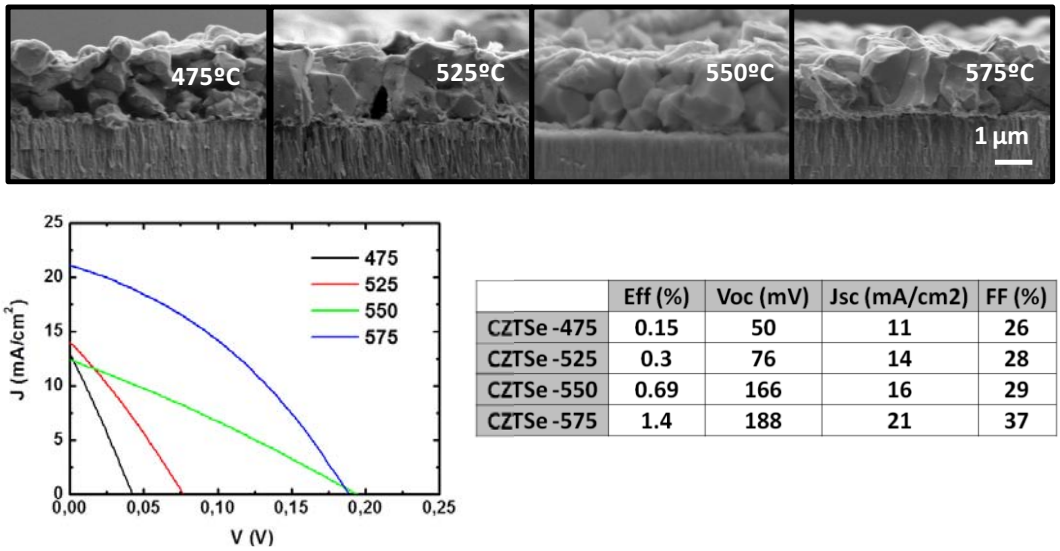

	Eff (%)	Voc (mV)	Jsc (mA/cm2)	FF (%)
CZTSe -475	0.15	50	11	26
CZTSe -525	0.3	76	14	28
CZTSe -550	0.69	166	16	29
CZTSe -575	1.4	188	21	37

Figure 23. SEM images of CZTS thin films selenized at 475°C, 525°C, 550°C and 575°C (a), and their PV performance (b).

In a first optimization, devices prepared with selenized CZTS-$SbCl_3$ films at 575°C showing relatively high current density of 20 mA/cm^2 were systematically achieved. However, rather

low open circuit voltages close to 200 mV and fill factors below 40 % were measured. This is translated into power conversion efficiencies of 1.4 % that although modest are encouraging for this low-cost and high-yield technology that allows the absorber material deposition in air and with the use of no hazardous chemicals, nor high vacuum equipment. Figure 24 shows a cross-sectional SEM image of the 1.4% CZTSe device.

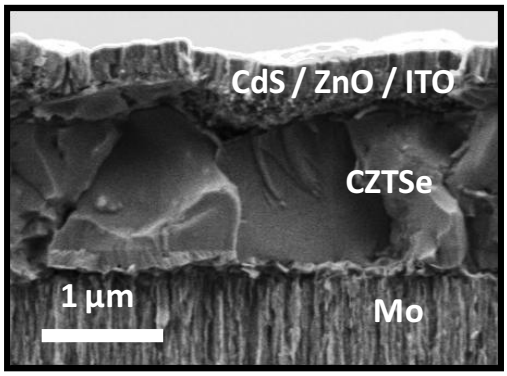

Figure 24 SEM cross-sectional image of the 1.4% CZTSe device.

The device spectral response of the same sample showed external quantum efficiencies up to 45 % and allowed to calculate a band gap of 0.97 eV (figure 25). EQE showed a relatively high degree of recombination at the space charge region, suggesting that the improvement of the junction could help to increase efficiency. Indeed, we believe the moderate performances measured could be related with a poor CZTSe-CdS interface, which also reduced the device open circuit voltage and fill factor.

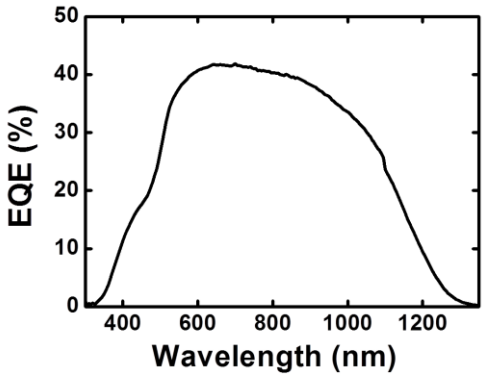

Figure 25. EQE spectral response of the same 1.4% efficiency CZTSe device.

The poor CZTSe-CdS interface could come from the presence of pinholes on the absorber surface. In order to reduce the presence of surface defects and subsequently improve the FF and the PV efficiency, a multistep selenization strategy was performed. A first 1 μm CZTS-$SbCl_3$ film was sprayed onto a Mo substrate. That film was selenized under soft conditions, meaning lower selenization temperatures, 450℃, and low Se pressure, by adding a lower Se content, 50 mg of Se, inside the graphite box, during the selenization. Soft conditions were selected in order to alleviate the formation of a $MoSe_2$ layer at the back contact. Figure 26 depicts cross-sectional SEM images of the whole procedure, showing small grained CZTSe thin films obtained after the first selenization.

Spray deposition of a second CZTS-$SbCl_3$ layer was performed over the first selenized film. In order to increase the grain growth, the second selenization was done under more aggressive conditions (550℃ and 100 mg of Se). The Se rich atmosphere during selenization was unable to penetrate the first crystallized layer, avoiding the reaction between the Mo and Se, and blocking the growth of the $MoSe_2$.

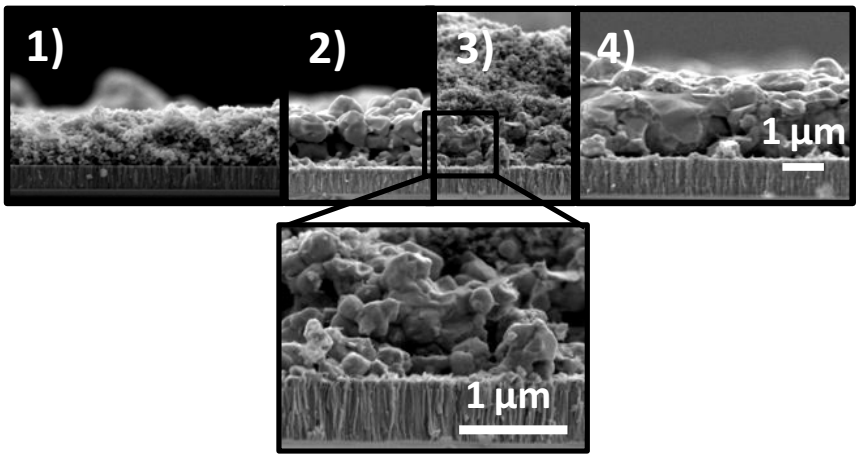

Figure 26. Cross-sectional SEM images of a multistep selenization strategy: 1) sprayed CZTS-$SbCl_3$ precursor 2) first selenization process at 450℃ at low Se pressure 3) second spray deposition of CZTS-$SbCl_3$, 4) second selenization at 550℃ under high Se pressure.

PV paramteres from a multistep selenized CZTS solar cell were compared to a standard selenized CZTS PV device (figure 27). While the J_{sc} was slightly improved from 17.2 to 18.4 mA/cm^2, the V_{oc} and FF were increased from 137 to 177 mV and 27.7 to 33.7% respectively.

The enhanced V_{oc} and FF lead to higher solar cell efficiencies. I-V curves from the multistep selenized absorber show similar V_{oc} from all the scribed cells in the same sample, around 200 mV, against the wide range of values observed from the standard sample, from 50 to 140 mV (figure 27). This is consistent with our previous hypothesis, confirming that it was possible to form more homogeneous CZTSe films, after a multistep selenization strategy. Furhter optimization, by increasing the number of spray/selenization cycles, is required in order to enhance the PV parameters.

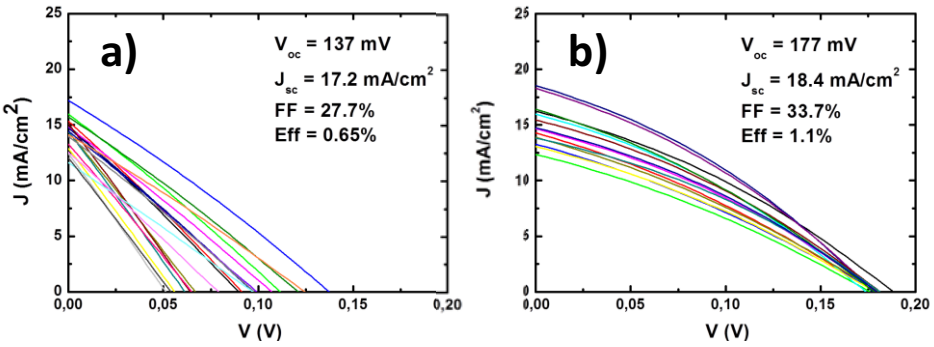

Figure 27. I-V curves of a standard (a) and a multistep (b) selenized CZTS-$SbCl_3$ PV devices.

5.3 Conclusions

In summary, a ligand exchange strategy to remove organics, introduce antimony and render CZTS NPs in solution and an automated pulsed spray deposition system to produce homogeneous and crack-free thin films were presented. Their combination allowed obtaining carbon-free thin films with controlled thickness and composition. We further demonstrate that the Sb-based ligand exchange strategy not only eliminates carbon from the final film thus improving electrical conductivity, but it also strongly promotes crystal growth before Sb is completely removed from the film. The Sb-assisted crystal growth is associated with the formation of a Sb-based compound at the GBs, which locally reduces the melting point, thus promoting the film diffusion-limited crystallization. Additionally a multistep selenization procedure has been proved as suitable strategy to prepare homogeneous devices. While thus-prepared CZTSe devices require optimization, our results demonstrate that the multi-strategy approach presented here has a high potential to produce low-cost PV grade CZTSe layers.

Also, a successful route for the continuous production of CZTS NPs has been presented. The preparation procedure allows simple and efficient control of the NP composition over a wide range. The route was used for the preparation of several grams of CZTS NPs, which were used for the thermoelectric characterization of this material in a nanocrystalline form. Single-particle HR-TEM−EDX analysis confirmed the presence of all four elements within each NP and demonstrated a narrow compositional distribution among NPs within each sample. The NP composition distribution was minimized at the highest reaction temperatures used.

6 Conclusions

This thesis describes the strategies that have been adopted for the development of CIGS and CZTS thin films for PV applications by solution processing of colloidal NPs. The conclusions can be extracted as following:

1) Detailed synthetic routes to produce CIGS and CZTS NP by colloidal synthesis are here presented. The composition control has been achieved by tuning the precursor concentration and using the proper organic surfactants and solvents. Also, pure wurtzite CIGS and kesterite CZTS crystal phases free of secondary phases were obtained by using the proper temperature, time and precursor solutions.

2) Additionally, a large scale procedure to prepare grams of CZTS NP is here presented. This method confirms the easy industrial scalability by preparing NPs by a simple vacuum free and low temperature system.

3) Ligand exchange methodologies to remove organic chains from the NP surface have been addressed. The effectiveness of the ligand exchange strategy to reduce the organic carbon present in CIGS and CZTS NP and the improvement of the further thin film crystallization is assessed. Additionally, the introduction of external dopants, such as $BiCl_3$ and $SbCl_3$ to induce a better grain growth, via ligand exchange of the organic ligands is proposed. The purified ligand exchanged NP were dispersed in a proper solvent to be used as a NP ink for further thin film deposition.

4) The synthesized NPs were successfully used as building blocks for the production of NP thin films by solution processing techniques. A simple custom-made automated pulsed open air spray deposition system is here used to produce smooth and crack free CIGS and CZTS thin films from colloidal CIGS and CZTS NPs. Spin coating technique have also been used to prepare CIGS thin films from chalcopyrite CIGS NPs. The conditions to obtain the proper thin film morphology and desired thicknesses have been optimized.

5) Different strategies have also been explored and analyzed for the optimization of the sintering processes. We have set the sintering parameters (temperature, time and experimental annealing conditions) to obtain pure and high crystalline chalcopyrite CIGS and kesterite CZTSe thin films.

6) Finally, PV performances from solution processed CIGSe and CZTSe solar cells are discussed.

Bibliography

(1) Smil, V. Op Cit 2003.

(2) SERVICE, R. F. Sci. C 2005, 309, 548.

(3) European Photovoltaic Industry Association. See Httpwww Epia OrgfileadminEPIAdocspublicGlobalMarketOutlookforPhotovoltaicsuntil2014 Pdf 2010.

(4) Shah, A.; Torres, P.; Tscharner, R.; Wyrsch, N.; Keppner, H. science 1999, 285, 692.

(5) Chopra, K.; Paulson, P.; Dutta, V. Prog. Photovolt. Res. Appl. 2004, 12, 69.

(6) Green, M. A. Prog. Photovolt. Res. Appl. 2006, 14, 383.

(7) Slaoui, A.; Collins, R. T. MRS Bull. 2007, 32, 211.

(8) Kazmerski, L. L. J. Electron Spectrosc. Relat. Phenom. 2006, 150, 105.

(9) Green, M. A.; Emery, K.; Hishikawa, Y.; Warta, W.; Dunlop, E. D. Prog. Photovolt. Res. Appl. 2014, 22, 701.

(10) Panthani, M. G.; Korgel, B. A. Annu. Rev. Chem. Biomol. Eng. 2012, 3, 287.

(11) Memming, R. Semiconductor electrochemistry; John Wiley & Sons, 2008.

(12) Würfel, P.; Würfel, U. Physics of solar cells: from basic principles to advanced concepts; John Wiley & Sons, 2009.

(13) Prabhakar, T.; Jampana, N. Sol. Energy Mater. Sol. Cells 2011, 95, 1001.

(14) Scragg, J. J.; Wätjen, J. T.; Edoff, M.; Ericson, T.; Kubart, T.; Platzer-Björkman, C. J. Am. Chem. Soc. 2012, 134, 19330.

(15) Wada, T.; Kohara, N.; Nishiwaki, S.; Negami, T. Thin Solid Films 2001, 387, 118.

(16) Shafarman, W.; Phillips, J. IEEE, 1996; pp. 917–919.

(17) Wang, W.; Winkler, M. T.; Gunawan, O.; Gokmen, T.; Todorov, T. K.; Zhu, Y.; Mitzi, D. B. Adv. Energy Mater. 2013, n/a.

(18) Repins, I.; Contreras, M. A.; Egaas, B.; DeHart, C.; Scharf, J.; Perkins, C. L.; To, B.; Noufi, R. Prog. Photovolt. Res. Appl. 2008, 16, 235.

(19) Devaney, W.; Chen, W.; Stewart, J.; Mickelsen, R. Electron Devices IEEE Trans. On 1990, 37, 428.

(20) Jackson, P.; Hariskos, D.; Lotter, E.; Paetel, S.; Wuerz, R.; Menner, R.; Wischmann, W.; Powalla, M. Prog. Photovolt. Res. Appl. 2011, 19, 894.

(21) Jaffe, J.; Zunger, A. Phys. Rev. B 1983, 28, 5822.

(22) Stanbery, B. J. Crit. Rev. Solid State Mater. Sci. 2002, 27, 73.

(23) Chen, S.; Gong, X.; Walsh, A.; Wei, S.-H. Phys. Rev. B 2009, 79, 165211.

(24) Zhang, S.; Wei, S.-H.; Zunger, A.; Katayama-Yoshida, H. Phys. Rev. B 1998, 57, 9642.

(25) Birkmire, R. W.; Eser, E. Annu. Rev. Mater. Sci. 1997, 27, 625.

(26) Katagiri, H.; Sasaguchi, N.; Hando, S.; Hoshino, S.; Ohashi, J.; Yokota, T. Sol. Energy Mater. Sol. Cells 1997, 49, 407.

(27) Shockley, W.; Queisser, H. J. J. Appl. Phys. 1961, 32, 510.

(28) Chen, S.; Gong, X. G.; Walsh, A.; Wei, S.-H. Appl. Phys. Lett. 2009, 94.

(29) Wei, H.; Ye, Z.; Li, M.; Su, Y.; Yang, Z.; Zhang, Y. CrystEngComm 2011, 13, 2222.

(30) Todorov, T. K.; Reuter, K. B.; Mitzi, D. B. Adv. Mater. 2010, 22, E156.

(31) Ford, G. M.; Guo, Q.; Agrawal, R.; Hillhouse, H. W. Chem. Mater. 2011, 23, 2626.

(32) Schorr, S.; Hoebler, H.-J.; Tovar, M. Eur. J. Mineral. 2007, 19, 65.

(33) Fontané, X.; Calvo-Barrio, L.; Izquierdo-Roca, V.; Saucedo, E.; Pérez-Rodriguez, A.; Morante, J.; Berg, D.; Dale, P.; Siebentritt, S. Appl. Phys. Lett. 2011, 98, 181905.

(34) Carrete, A.; Shavel, A.; Fontané, X.; Montserrat, J.; Fan, J.; Ibáñez, M.; Saucedo, E.; Pérez-Rodríguez, A.; Cabot, A. J. Am. Chem. Soc. 2013, 135, 15982.

(35) Shavel, A.; Cadavid, D.; Ibáñez, M.; Carrete, A.; Cabot, A. J. Am. Chem. Soc. 2012, 134, 1438.

(36) Chen, S.; Yang, J.-H.; Gong, X.; Walsh, A.; Wei, S.-H. Phys. Rev. B 2010, 81, 245204.

(37) Shin, B.; Gunawan, O.; Zhu, Y.; Bojarczuk, N. A.; Chey, S. J.; Guha, S. Prog. Photovolt. Res. Appl. 2013, 21, 72.

(38) Wang, K.; Gunawan, O.; Todorov, T.; Shin, B.; Chey, S.; Bojarczuk, N.; Mitzi, D.; Guha, S. Appl. Phys. Lett. 2010, 97, 143508.

(39) Katagiri, H.; Jimbo, K.; Yamada, S.; Kamimura, T.; Maw, W. S.; Fukano, T.; Ito, T.; Motohiro, T. Appl. Phys. Express 2008, 1, 041201.

(40) Fernandes, P.; Salomé, P.; Da Cunha, A. Thin Solid Films 2009, 517, 2519.

(41) Todorov, T. K.; Reuter, K. B.; Mitzi, D. B. Adv. Mater. 2010, 22, E156.

(42) Guo, Q.; Ford, G. M.; Yang, W.-C.; Walker, B. C.; Stach, E. A.; Hillhouse, H. W.; Agrawal, R. J. Am. Chem. Soc. 2010, 132, 17384.

(43) Scragg, J. J.; Dale, P. J.; Peter, L. M. Thin Solid Films 2009, 517, 2481.

(44) Scragg, J. J.; Berg, D. M.; Dale, P. J. J. Electroanal. Chem. 2010, 646, 52.

(45) Ahmed, S.; Reuter, K. B.; Gunawan, O.; Guo, L.; Romankiw, L. T.; Deligianni, H. Adv. Energy Mater. 2012, 2, 253.

(46) Guo, L.; Zhu, Y.; Gunawan, O.; Gokmen, T.; Deline, V. R.; Ahmed, S.; Romankiw, L. T.; Deligianni, H. Prog. Photovolt. Res. Appl. 2014, 22, 58.

(47) Ilari, G. M.; Fella, C. M.; Ziegler, C.; Uhl, A. R.; Romanyuk, Y. E.; Tiwari, A. N. Sol. Energy Mater. Sol. Cells 2012, 104, 125.

(48) Tian, Q.; Xu, X.; Han, L.; Tang, M.; Zou, R.; Chen, Z.; Yu, M.; Yang, J.; Hu, J. CrystEngComm 2012, 14, 3847.

(49) Carrete, A.; Placidi, M.; Shavel, A.; Pérez-Rodríguez, A.; Cabot, A. Phys. Status Solidi A 2014.

(50) Van Embden, J.; Chesman, A. S.; Della Gaspera, E.; Duffy, N. W.; Watkins, S. E.; Jasieniak, J. J. J. Am. Chem. Soc. 2014, 136, 5237.

(51) Tanaka, K.; Moritake, N.; Oonuki, M.; Uchiki, H. Jpn. J. Appl. Phys. 2008, 47, 598.

(52) Fella, C. M.; Uhl, A. R.; Romanyuk, Y. E.; Tiwari, A. N. Phys. Status Solidi A 2012, 209, 1043.

(53) Ibáñez, M.; Cadavid, D.; Zamani, R.; García-Castelló, N.; Izquierdo-Roca, V.; Li, W.; Fairbrother, A.; Prades, J. D.; Shavel, A.; Arbiol, J.; Pérez-Rodríguez, A.; Morante, J. R.; Cabot, A. Chem. Mater. 2012, 24, 562.

(54) Li, W.; Ibanez, M.; Zamani, R. R.; Garcia-Castello, N.; Gorsse, S.; Cadavid, D.; Prades, J. D.; Arbiol, J.; Cabot, A. CrystEngComm 2013, 15, 8966.

(55) Li, W.; Zamani, R.; Rivera Gil, P.; Pelaz, B.; Ibáñez, M.; Cadavid, D.; Shavel, A.; Alvarez-Puebla, R. A.; Parak, W. J.; Arbiol, J.; Cabot, A. J. Am. Chem. Soc. 2013, 135, 7098.

(56) Zhong, J.; Xia, Z.; Zhang, C.; Li, B.; Liu, X.; Cheng, Y.-B.; Tang, J. Chem. Mater. 2014.

(57) Yin, Y.; Alivisatos, A. P. Nature 2004, 437, 664.

(58) Kovalenko, M. V.; Scheele, M.; Talapin, D. V. Science 2009, 324, 1417.

(59) Talapin, D. V.; Lee, J.-S.; Kovalenko, M. V.; Shevchenko, E. V. Chem. Rev. 2009, 110, 389.

(60) Nag, A.; Kovalenko, M. V.; Lee, J.-S.; Liu, W.; Spokoyny, B.; Talapin, D. V. J. Am. Chem. Soc. 2011, 133, 10612.

(61) Bucherl, C. N.; Oleson, K. R.; Hillhouse, H. W. Curr. Opin. Chem. Eng. 2013, 2, 168.

(62) Fang, Z. Z.; Wang, X.; Ryu, T.; Hwang, K. S.; Sohn, H. Int. J. Refract. Met. Hard Mater. 2009, 27, 288.

(63) Rollett, A.; Humphreys, F.; Rohrer, G. S.; Hatherly, M. Recrystallization and related annealing phenomena; Elsevier, 2004.

(64) Rahaman, M. N. Sintering of ceramics; CRC press Boca Raton:, 2008.

(65) Kang, S.-J. L. Sintering: densification, grain growth and microstructure; Butterworth-Heinemann, 2004.

(66) Lee, B.-K.; Chung, S.-Y.; Kang, S.-J. L. Acta Mater. 2000, 48, 1575.

(67) Burke, J.; Turnbull, D. Prog. Met. Phys. 1952, 3, 220.

(68) Lange, F.; Hirlinger, M. M. J. Am. Ceram. Soc. 1984, 67, 164.

(69) Nieh, T.; Wadsworth, J. J. Am. Ceram. Soc. 1989, 72, 1469.

(70) Owen, D.; Chokshi, A. Acta Mater. 1998, 46, 667.

(71) Chen, I.-W.; Wang, X.-H. Nature 2000, 404, 168.

(72) Louat, N. Acta Metall. 1982, 30, 1291.

(73) PA, M.; Chandra, T. ISIJ Int. 1998, 38, 913.

(74) Liao, S.; Mayo, W.; Pae, K. Acta Mater. 1997, 45, 4027.

(75) Liao, S.-C.; Chen, Y.-J.; Mayo, W.; Kear, B. Nanostructured Mater. 1999, 11, 553.

(76) Hague, D. C.; Mayo, M. J. Mater. Sci. Eng. A 1995, 204, 83.

(77) Owen, D.; Chokshi, A. H. Nanostructured Mater. 1993, 2, 181.

(78) Uchic, M.; Höfler, H.; Flick, W.; Tao, R.; Kurath, P.; Averback, R. Scr. Metall. Mater. 1992, 26, 791.

(79) Omori, M. Mater. Sci. Eng. A 2000, 287, 183.

(80) Ibanez, M.; Cadavid, D.; Anselmi-Tamburini, U.; Zamani, R.; Gorsse, S.; Li, W.; Lopez, A. M.; Morante, J. R.; Arbiol, J.; Cabot, A. J Mater Chem A 2013, 1, 1421.

(81) Olson, J.; Rodriguez, Y.; Yang, L.; Alers, G.; Carter, S. Appl. Phys. Lett. 2010, 96, 242103.

(82) Panthani, M. G.; Kurley, J. M.; Crisp, R. W.; Dietz, T. C.; Ezzyat, T.; Luther, J. M.; Talapin, D. V. Nano Lett. 2014, 14, 670.

(83) Goldstein, A.; Echer, C.; Alivisatos, A. Science 1992, 256, 1425.

(84) Mainz, R.; Singh, A.; Levcenko, S.; Klaus, M.; Genzel, C.; Ryan, K.; Unold, T. Nat. Commun. 2014, 5.

(85) Guo, Q.; Kim, S. J.; Kar, M.; Shafarman, W. N.; Birkmire, R. W.; Stach, E. A.; Agrawal, R.; Hillhouse, H. W. Nano Lett. 2008, 8, 2982.

(86) Kaelin, M.; Rudmann, D.; Kurdesau, F.; Meyer, T.; Zogg, H.; Tiwari, A. Thin Solid Films 2003, 431, 58.

(87) Guo, Q.; Ford, G. M.; Hillhouse, H. W.; Agrawal, R. Nano Lett. 2009, 9, 3060.

(88) Mainz, R.; Walker, B. C.; Schmidt, S. S.; Zander, O.; Weber, A.; Rodriguez-Alvarez, H.; Just, J.; Klaus, M.; Agrawal, R.; Unold, T. Phys. Chem. Chem. Phys. 2013, 15, 18281.

(89) Yuan, M.; Mitzi, D. B.; Liu, W.; Kellock, A. J.; Chey, S. J.; Deline, V. R. Chem. Mater. 2010, 22, 285.

(90) Yuan, M.; Mitzi, D. B.; Gunawan, O.; Kellock, A. J.; Chey, S. J.; Deline, V. R. Thin Solid Films 2010, 519, 852.

(91) Chen, F.-S.; Ma, J.-S.; Sung, J.-C.; Lu, C.-H. Sol. Energy Mater. Sol. Cells 2014, 124, 166.

(92) Contreras, M. A.; Egaas, B.; Dippo, P.; Webb, J.; Granata, J.; Ramanathan, K.; Asher, S.; Swartzlander, A.; Noufi, R. IEEE, 1997; pp. 359–362.

(93) Braunger, D.; Hariskos, D.; Bilger, G.; Rau, U.; Schock, H. Thin Solid Films 2000, 361, 161.

(94) Hergert, F.; Jost, S.; Hock, R.; Purwins, M.; Palm, J. Thin Solid Films 2007, 515, 5843.

(95) Xiang, Y.; Zhang, X.; Zhang, S. J. Solid State Chem. 2013, 204, 278.

(96) Nast, O.; Wenham, S. R. J. Appl. Phys. 2000, 88, 124.

(97) Wang, Y.; Gong, H. J. Electrochem. Soc. 2011, 158, H800.

(98) Cao, Y.; Denny, M. S.; Caspar, J. V.; Farneth, W. E.; Guo, Q.; Ionkin, A. S.; Johnson, L. K.; Lu, M.; Malajovich, I.; Radu, D.; Rosenfeld, H. D.; Choudhury, K. R.; Wu, W. J. Am. Chem. Soc. 2012, 134, 15644.

(99) Carter, N. J.; Yang, W.-C.; Miskin, C. K.; Hages, C. J.; Stach, E. A.; Agrawal, R. Sol. Energy Mater. Sol. Cells 2014, 123, 189.

(100) Jiang, C.; Lee, J.-S.; Talapin, D. V. J. Am. Chem. Soc. 2012, 134, 5010.

(101) Kovalenko, M. V.; Scheele, M.; Talapin, D. V. Science 2009, 324, 1417.

(102) Cai, Y.; Ho, J. C. W.; Batabyal, S. K.; Liu, W.; Sun, Y.; Mhaisalkar, S. G.; Wong, L. H. ACS Appl. Mater. Interfaces 2013, 5, 1533.

(103) Walker, B.; Agrawal, R. IEEE, 2012; pp. 002654–002657.

(104) Murray, C. B.; Kagan, C.; Bawendi, M. Annu. Rev. Mater. Sci. 2000, 30, 545.

(105) Lee, D.; Yong, K. Korean J. Chem. Eng. 2013, 30, 1347.

(106) Todorov, T. K.; Gunawan, O.; Gokmen, T.; Mitzi, D. B. Prog. Photovolt. Res. Appl. 2013, 21, 82.

(107) Akhavan, V. A.; Goodfellow, B. W.; Panthani, M. G.; Reid, D. K.; Hellebusch, D. J.; Adachi, T.; Korgel, B. A. Energy Env. Sci 2010, 3, 1600.

(108) Guo, Q.; Ford, G. M.; Agrawal, R.; Hillhouse, H. W. Prog. Photovolt. Res. Appl. 2013, 21, 64.

(109) Ibáñez, M.; Zamani, R.; LaLonde, A.; Cadavid, D.; Li, W.; Shavel, A.; Arbiol, J.; Morante, J. R.; Gorsse, S.; Snyder, G. J. J. Am. Chem. Soc. 2012, 134, 4060.

(110) Ibáñez, M.; Zamani, R.; Li, W.; Shavel, A.; Arbiol, J.; Morante, J. R.; Cabot, A. Cryst. Growth Des. 2012, 12, 1085.

(111) Stolle, C. J.; Harvey, T. B.; Korgel, B. A. Curr. Opin. Chem. Eng. 2013, 2, 160.

(112) Harvey, T. B.; Mori, I.; Stolle, C. J.; Bogart, T. D.; Ostrowski, D. P.; Glaz, M. S.; Du, J.; Pernik, D. R.; Akhavan, V. A.; Kesrouani, H. ACS Appl. Mater. Interfaces 2013, 5, 9134.

(113) Fang, Z. Z. Sintering of advanced materials; Elsevier, 2010.

(114) Talapin, D. V.; Murray, C. B. Science 2005, 310, 86.

(115) Yu, X.; An, X.; Shavel, A.; Ibañez, M.; Cabot, A. J. Mater. Chem. A 2014.

(116) Salomé, P.; Fernandes, P.; da Cunha, A. Thin Solid Films 2009, 517, 2531.

(117) Eberspacher, C.; Fredric, C.; Pauls and Jack Serra, K. Thin Solid Films 2001, 387, 18.

(118) Law, M.; Luther, J. M.; Song, Q.; Hughes, B. K.; Perkins, C. L.; Nozik, A. J. J. Am. Chem. Soc. 2008, 130, 5974.

(119) Marjanovic, N.; Hammerschmidt, J.; Perelaer, J.; Farnsworth, S.; Rawson, I.; Kus, M.; Yenel, E.; Tilki, S.; Schubert, U. S.; Baumann, R. R. J. Mater. Chem. 2011, 21, 13634.

(120) Park, S.-W.; Kim, D.-I.; Lee, T.-S.; Lee, K.; Yoon, Y.; Cho, Y. H.; Kim, J. H.; Ahn, K. M.; Lee, K. J.; Jeon, C.-W. Sol. Energy Mater. Sol. Cells 2014, 125, 66.

(121) Park, J. S.; Seo, J.; Park, S. W.; Jung, W. J.; Park, N. M.; Kim, J.; Jeon, C. W. Jpn. J. Appl. Phys. 2012, 51, 10NC21.

(122) Granath, K.; Bodegård, M.; Stolt, L. Sol. Energy Mater. Sol. Cells 2000, 60, 279.

(123) Nakada, T.; Iga, D.; Ohbo, H.; Kunioka, A. Jpn. J. Appl. Phys. 1997, 36, 732.

(124) Rockett, A.; Britt, J.; Gillespie, T.; Marshall, C.; Al Jassim, M.; Hasoon, F.; Matson, R.; Basol, B. Thin Solid Films 2000, 372, 212.

(125) Rudmann, D.; Da Cunha, A.; Kaelin, M.; Kurdesau, F.; Zogg, H.; Tiwari, A.; Bilger, G. Appl. Phys. Lett. 2004, 84, 1129.

(126) Wei, S.-H.; Zhang, S.; Zunger, A. J. Appl. Phys. 1999, 85, 7214.

(127) Dilena, E.; Xie, Y.; Brescia, R.; Prato, M.; Maserati, L.; Krahne, R.; Paolella, A.; Bertoni, G.; Povia, M.; Moreels, I. Chem. Mater. 2013, 25, 3180.

(128) Todorov, T. K.; Tang, J.; Bag, S.; Gunawan, O.; Gokmen, T.; Zhu, Y.; Mitzi, D. B. Adv. Energy Mater. 2013, 3, 34.

(129) Shavel, A.; Arbiol, J.; Cabot, A. J. Am. Chem. Soc. 2010, 132, 4514.

(130) Singh, A.; Geaney, H.; Laffir, F.; Ryan, K. M. J. Am. Chem. Soc. 2012, 134, 2910.

(131) Aldakov, D.; Lefrançois, A.; Reiss, P. J. Mater. Chem. C 2013, 1, 3756.

(132) Steinhagen, C.; Panthani, M. G.; Akhavan, V.; Goodfellow, B.; Koo, B.; Korgel, B. A. J. Am. Chem. Soc. 2009, 131, 12554.

(133) Li, W.; Shavel, A.; Guzman, R.; Rubio-Garcia, J.; Flox, C.; Fan, J.; Cadavid, D.; Ibáñez, M.; Arbiol, J.; Morante, J. R. Chem. Commun. 2011, 47, 10332.

(134) Kawa, M.; Morii, H.; Ioku, A.; Saita, S.; Okuyama, K. J. Nanoparticle Res. 2003, 5, 81.

(135) Lin, X. Z.; Terepka, A. D.; Yang, H. Nano Lett. 2004, 4, 2227.

(136) Huang, J.; Lin, L.; Li, Q.; Sun, D.; Wang, Y.; Lu, Y.; He, N.; Yang, K.; Yang, X.; Wang, H. Ind. Eng. Chem. Res. 2008, 47, 6081.

(137) Nakamura, H.; Yamaguchi, Y.; Miyazaki, M.; Maeda, H.; Uehara, M.; Mulvaney, P. Chem. Commun. 2002, 2844.

(138) Jin, H. D.; Chang, C.-H. J. Mater. Chem. 2011, 21, 12218.

(139) Fairbrother, A.; García-Hemme, E.; Izquierdo-Roca, V.; Fontané, X.; Pulgarín-Agudelo, F. A.; Vigil-Galán, O.; Pérez-Rodríguez, A.; Saucedo, E. J. Am. Chem. Soc. 2012, 134, 8018.

(140) Jellison Jr, G. Thin Solid Films 1998, 313, 33.

(141) Liu, M.-L.; Huang, F.-Q.; Chen, L.-D.; Chen, I.-W. Appl. Phys. Lett. 2009, 94, 202103.

(142) Lu, X.; Zhuang, Z.; Peng, Q.; Li, Y. Chem Commun 2011, 47, 3141.

(143) Mitzi, D. B.; Gunawan, O.; Todorov, T. K.; Wang, K.; Guha, S. Sol. Energy Mater. Sol. Cells 2011, 95, 1421.

(144) Olekseyuk, I.; Dudchak, I.; Piskach, L. J. Alloys Compd. 2004, 368, 135.

(145) Haas, W.; Rath, T.; Pein, A.; Rattenberger, J.; Trimmel, G.; Hofer, F. Chem Commun 2011, 47, 2050.

(146) Ibáñez, M.; Zamani, R.; Li, W.; Cadavid, D.; Gorsse, S.; Katcho, N. A.; Shavel, A.; López, A. M.; Morante, J. R.; Arbiol, J.; Cabot, A. Chem. Mater. 2012, 24, 4615.

(147) Cadavid, D.; Ibanez, M.; Shavel, A.; Dura, O. J.; Lopez de la Torre, M. A.; Cabot, A. J Mater Chem A 2013, 1, 4864.

(148) Weber, A.; Mainz, R.; Schock, H. J. Appl. Phys. 2010, 107, 013516.

(149) Redinger, A.; Berg, D. M.; Dale, P. J.; Siebentritt, S. J. Am. Chem. Soc. 2011, 133, 3320.

(150) Scragg, J. J.; Ericson, T.; Kubart, T.; Edoff, M.; Platzer-Björkman, C. Chem. Mater. 2011, 23, 4625.

(151) Khare, A.; Himmetoglu, B.; Johnson, M.; Norris, D. J.; Cococcioni, M.; Aydil, E. S. J. Appl. Phys. 2012, 111, 083707.

(152) Gürel, T.; Sevik, C.; Çağın, T. Phys. Rev. B 2011, 84, 205201.

(153) Fontané, X.; Izquierdo-Roca, V.; Saucedo, E.; Schorr, S.; Yukhymchuk, V.; Valakh, M. Y.; Pérez-Rodríguez, A.; Morante, J. J. Alloys Compd. 2012, 539, 190.

(154) Djemour, R.; Redinger, A.; Mousel, M.; Gütay, L.; Fontané, X.; Izquierdo-Roca, V.; Pérez-Rodríguez, A.; Siebentritt, S. Opt Express 2013, 21, A695.

(155) Espindola-Rodriguez, M.; Placidi, M.; Vigil-Galán, O.; Izquierdo-Roca, V.; Fontané, X.; Fairbrother, A.; Sylla, D.; Saucedo, E.; Pérez-Rodríguez, A. Thin Solid Films 2013, 535, 67.

(156) Zhang, S.; Wu, L.; Yue, R.; Yan, Z.; Zhan, H.; Xiang, Y. Thin Solid Films 2013, 527, 137.

(157) Berger, L. I.; Prochukhan, V. D. Ternary diamond-like semiconductors; Springer, 1995.

(158) Nenow, D.; Pamplin, B. 1984.

(159) Repins, I.; Beall, C.; Vora, N.; DeHart, C.; Kuciauskas, D.; Dippo, P.; To, B.; Mann, J.; Hsu, W.-C.; Goodrich, A.; Noufi, R. Sol. Energy Mater. Sol. Cells 2012, 101, 154.

(160) Marcano, G.; Rincón, C.; López, S.; Sánchez Pérez, G.; Herrera-Pérez, J.; Mendoza-Alvarez, J.; Rodríguez, P. Solid State Commun. 2011, 151, 84.

(161) López-Marino, S.; Sánchez, Y.; Placidi, M.; Fairbrother, A.; Espindola-Rodríguez, M.; Fontané, X.; Izquierdo-Roca, V.; López-García, J.; Calvo-Barrio, L.; Pérez-Rodríguez, A. Chem.- Eur. J. 2013, 19, 14814.

(162) Chen, S.; Walsh, A.; Yang, J.-H.; Gong, X.; Sun, L.; Yang, P.-X.; Chu, J.-H.; Wei, S.-H. Phys. Rev. B 2011, 83, 125201.

(163) Duan, H.-S.; Yang, W.; Bob, B.; Hsu, C.-J.; Lei, B.; Yang, Y. Adv. Funct. Mater. 2013, 23, 1466.

Acknowledgements

I would like to express my sincere gratitude to my research supervisor, ***Dr. Andreu Cabot***, for offering me the opportunity to carry out my PhD thesis in the Functional Nanomaterials group at IREC and introducing me to research. I also want to thank him for giving me the opportunity to do my PhD in such an interesting topic as photovoltaics through nanoparticles. Finally I want to thank him for providing the excellent experimental laboratories and characterization facilities with which it has been possible to complete this work.

My most sincere thanks to all the members of the Functional Nanomaterials group with whom I shared so many unforgettable moments during these years in the University and in IREC. I do not want to forget anyone: Alexey, Maria, Fan, Wenhua, Doris, Raquel, Joost, Zhishan, Xuelian, Silvia, Joana, Ariadna, Rick, Pedro, Alejandro, Gihan, Pablo, Liu and Michaela.

I also want to thank the Photovoltaics group for their all collaboration and all the helpful discussions: Diouldé (I owe you several Vichy Catalan jeje), Xavi, Marcel, Simon, Moisés, Yudania, Juan, Mirjana, Edgardo…

També vull recordar tota la gent de l'IREC amb la que he compartit bons moments a l'oficina, dinars, tupper-group's, cafés a l'Ahmed, dinars al parada, quiz night's, calçotades, etc

També vull donarli les gràcies a la meva familia. Sense la vostre manera d'entrendre la vida, el vostre suport, els valors i l'educació rebuda, no hauria tingut la força per a completar aquest repte.

Finalment vull donar-li gràcies a l'Àuria. Gràcies per estar sempre al meu costat durant tots aquests anys en els bons i mals moments. Al teu costat tot és sempre més senzill.

Abbreviations

ATR-FTIR	Attentuated total reflectance fourier transform infrared spectroscopy
CIGS	$CuIn_{1-x}Ga_xS_2$
CIGSe	$CuIn_{1-x}Ga_xSe_2$
CIS	$CuInS_2$
CZTS	Cu_2ZnSnS_4
CZTSe	$Cu_2ZnSnSe_4$
CZTSSe	$Cu_2ZnSn(S,Se)_4$
DDT	1-dodecanethiol
EA	Elemental analysis
EQE	External quantum efficiency
FF	Fill factor
GB	Grain boundary
HR-TEM	High resolution transmission electron microscopy
ITO	Indium tin oxide
i-ZnO	Intrinsic ZnO
J_{sc}	Short circuit current density
MMC	Molecular metal chalcogenide
Mo	Molybdenum
NP	Nanoparticle
ODE	Octadecene
ODPA	Octadecyl phosphonic acid
OLA	Oleylamine
PV	Photovoltaic
SEM-EDX	Scanning electron microscopy – energy dispersive X-ray spectroscopy
SIMS	Secondary ion mass spectroscopy
SLG	Soda lime glass
SPS	Spark plasma sintering
TCO	Transparent conductive oxide

TEM	Transmission electron microscopy
TGA	Thermo gravimetric analysis
THF	Tetrahydrofuran
TOPO	Trioctylphosphine oxide
UV	Ultraviolet
UV-Vis	Ultraviolet-visible
UV-Vis-NIR	Ultraviolet-visible-near infrared
V_{oc}	Open circuit voltage
XPS	X-ray photoelectron spectroscopy
XRD	X-ray diffraction
AZO	ZnO:Al

Curriculum Vitae

Àlex Carreté Bello

Barcelona, 7th November 1984

acarrebe890@gmail.com

656 99 79 21

Education

INSTITUTION AND LOCATION	DEGREE	MM/YY	FIELD OF STUDY
Universitat de Barcelona	Bachelor's	07/09	Chemistry
Universitat de Barcelona	Master thesis	09/10	Nanotechnology

Positions and Employments

October 2009 - September 2010	Master student, Department of Physical Chemistry, Universitat de Barcelona.
June 2009 - September 2009	Intern, Organic Analysis Laboratory, Agència Catalana de l'Aigua.
January 2009 - June 2009	Intern, Quality Assurance Unit, Scientifics and Technological Centers Of University Of Barcelona.
June 2008 - September 2008	Intern, Wastewater and Drinking Water Laboratory, Mina Pública d'Aigües de Terrassa S.A.

Publications

M. Dimitrievska, G. Gurieva, H. Xie, A. Carrete, A. Cabot, E. Saucedo, A. Pérez-Rodríguez, S Schorr, and V. Izquierdo-Roca. "Raman scattering quantitative analysis of the anion chemical composition in kesterite Cu2ZnSn(SxSe1-x)4 solid solutions" Journal of Physical Chemistry C, **DOI:10.1016/j.jallcom.2014.12.175**.

A. Carrete, M. Placidi, A. Shavel, A. Pérez-Rodríguez, and A. Cabot. "Spray-deposited CuIn1-xGaxSe2 solar cell absorbers: Influence of spray deposition parameters and crystallization promoters" Physica status solidi (a), **2014**, 212, pp 67-71.

A. Carrete, A. Shavel, X. Fontané, J. Montserrat, J. Fan, M. Ibáñez, E. Saucedo, A. Pérez-Rodríguez, and A. Cabot. "Antimony-Based Ligand Exchange To Promote Crystallization in Spray-Deposited Cu2ZnSnSe4 Solar Cells." Journal of the American Chemical Society, **2013** 135 (43), pp 15982-15985.

J. Fan, C. Fábrega, R. Zamani, A. Shavel, F. Güell, A. Carrete, T. Andreu, A. M. López, J. R. Morante, J. Arbiol and A. Cabot. "*Solution-Growth and Optoelectronic Properties of ZnO:Cl@ZnS Core-Shell Nanowires with Tunable Shell Thickness".* Journal of Alloy and Compounds, **2013,** 555, pp 213–218.

A. Shavel, D. Cadavid, M. Ibáñez, A. Carrete, and A. Cabot. "*Continuous Production of Cu_2ZnSnS_4 Nanocrystals in a Flow Reactor".* Journal of the American Chemical Society, **2012**, *134* (3), pp 1438–1441.

J. Fan, F. Guell, C. Fabrega, A. Shavel, A. Carrete, T. Andreu, J. R. Morante, and A. Cabot. "*Enhancement of the photoelectrochemical properties of Cl-doped ZnO nanowires by tuning their coaxial doping profile".* Applied Physics Letters*,* **2011,** 99, pp 262102 - 262102-4.

J. Fan, A. Shavel, R. Zamani, C. Fábrega, J. Rousset, S. Haller, F. Güell, A. Carrete, T. Andreu, J. Arbiol, J. R. Morante and A. Cabot. "*Control of the doping concentration, morphology and optoelectronic properties of vertically aligned chlorine-doped ZnO nanowires"*. Acta Materialia, **2011,** 59, pp 6790–6800.

M. Ibáñez, J. Fan, W. Li, D. Cadavid, R. Nafria, A. Carrete, and A. Cabot. "*Means and Limits of Control of the Shell Parameters in Hollow Nanoparticles Obtained by the Kirkendall Effect".* Chemistry of Material, **2011,** *23*, pp 3095–3104.

Conference and seminars

A. Carrete, J. Montserrat, A. Shavel, J. Fan, A. Cabot. Solution processing of CZTS solar cells: Organic carbon removal by inorganic ligand exchange. EMRS Spring meeting, 2013. Strasbourg

A. Shavel, A. Carrete, J. Fan, A. Cabot. Solution processing of CZTS solar cells: Organic carbon removal by inorganic ligand exchange. 3rd European Kesterite Workshop, 2012. Luxembourg.

A. Shavel, A. Carrete, J. Fan, A. Cabot. Solution-processed CZTS for PV applications. EMRS Spring meeting, 2011. Nice.

A. Carrete, A. Shavel, J. Fan, E. Saucedo, V.Izquierdo-Roca, X. Fontané, A. Pérez-Rodriguez, J.R. Morante, Andreu Cabot. Soltution-processing of CZTS nanoparticles and layer for PV applications. XVII Trobades científiques de la mediterrania, 2011. Maó.

F. Caballero-Briones, A. Carrete, J.L. Peña, O. Calzadilla and F. Sanz. Mg-doped cadmium sulfide thin films: Chemical structural, optical and nanoelectrical characterization. Photovoltaic Technical Conference – Thin film and advanced solutions, 2011. Aix-en-Provenze.

Annex

Wiley Online Library
Early View publication on www.wileyonlinelibrary.com
(issue and page numbers not yet assigned;
citable using Digital Object Identifier – DOI)

Phys. Status Solidi A, 1–5 (2014) / DOI 10.1002/pssa.201431425

Part of Topical Section on
Advanced Materials and Nanotechnology for Photovoltaics

physica status solidi a
www.pss-a.com
applications and materials science

Spray-deposited $CuIn_{1-x}Ga_xSe_2$ solar cell absorbers: Influence of spray deposition parameters and crystallization promoters

Alex Carrete[1], Marcel Placidi[1], Alexey Shavel[1], Alejandro Pérez-Rodríguez[1,2], and Andreu Cabot*[,1,3]

[1] Catalonia Institute for Energy Research – IREC, Jardins de les Dones de Negre 1, Sant Adrià del Besòs, Barcelona, Spain
[2] IN2UB, Departament d'Electrònica, Universitat de Barcelona, C. Martí i Franquès 1, Barcelona, Spain
[3] Institució Catalana de Recerca i Estudis Avançats – ICREA, Barcelona, Spain

Received 10 June 2014, revised 30 September 2014, accepted 9 October 2014
Published online 6 November 2014

Keywords chalcopyrites, crystallization, $CuInGaS_2$, nanoparticles, spray deposition

* Corresponding author: e-mail acabot@irec.cat, Phone: +34 933 562 615, Fax: +34 933 563 802

To produce smooth, crack-free, and highly crystalline absorber layers are the main challenges in the fabrication of thin film solar cells using nanoparticle-based solution-processing technologies. In this work, we report on the optimization of the spray deposition parameters to produce highly homogeneous $CuIn_{1-x}Ga_xS_2$ thin films with controlled thickness using nanoparticle-based inks. We further explore the use of inorganic ligand exchange strategies to introduce metal ions able to promote crystallization during the selenization of the layers, removing structural defects and grain boundaries that potentially act as recombination centers.

1 Introduction Thin film solar cells based on direct band gap semiconductors are already at industrial stage and display record power conversion efficiencies up to 20.9% [1, 2]. To implement this technology, the most promising absorber material is $CuIn_{1-x}Ga_xSe_2$ (CIGSe), a strong light absorber with a direct bandgap in the range 1.0–1.7 eV, depending on the Ga content, and which holds the record efficiency for thin film photovoltaics (PV).

CIGSe thin films can be prepared by vacuum and non-vacuum technologies [1–4]. On the one hand, vacuum deposition methods allow achieving the highest device efficiencies, but they require large capital and operation costs, and are characterized by relatively low material yields and throughputs. These drawbacks compromise their potential to substantially reduce the current cost of the PV modules. On the other hand, non-vacuum technologies, such as printing or electrodeposition, require lower capital investments and have associated lower maintenance costs. They also provide higher material yields and production rates, what make them highly appropriate for large-scale industrial production. While solution-based approaches have reached efficiencies up to 15.2% with CIGSe [4], their main limitation is the lower device efficiencies generally obtained when compared with vacuum-based technologies.

Among the different solution-based technologies, the printing or spraying of colloidal nanoparticles is particularly interesting to produce layers of quaternary materials with unmatched composition and phase homogeneity at the nanometer scale [5–8]. Such unparalleled control over material properties at the atomic scale is a result of the high level of control in the growth of these compounds recently reached by colloidal synthesis routes [9–12]. Nevertheless, efficient PV devices require not only compositionally homogeneous absorbers, but also continuous and dense layers made of large and defect-free crystal domains [13, 14]. To properly crystallize CIGSe absorber layers, an annealing treatment at a temperature close to 550 °C in a chalcogen atmosphere is generally used. A chalcogen exchange during the crystallization process usually promotes the formation of larger grains and denser layers [15]. However, the proper crystallization of the absorber layer is still one of the main challenges involved in the fabrication of PV devices by solution-based approaches. Several strategies to promote grain growth and to reduce the process temperature have been attempted. These strategies include the incorporation of sodium [8], copper selenide nanocrystals [16], or antimony [17, 18] in the absorber layer and the use of a multi-step selenization process [19, 20].

In this work, we systematically optimized the ink formulation and spray deposition conditions to produce highly homogeneous, smooth, and crack-free $CuIn_{1-x}Ga_xS_2$ (CIGS) layers from nanoparticle-based inks. We further describe here the potential of crystallization promoters to achieve CIGSe absorbers with improved crystalline quality.

2 Experimental details

2.1 CIGS nanoparticle synthesis CIGS nanoparticles were obtained following a previously reported procedure [21]. Briefly, $Cu(acac)_2$ (1 mmol), $In(acac)_3$ (0.75 mmol), $Ga(acac)_3$ (0.25 mmol), trioctylphosphine oxide (TOPO; 3.35 mmol), and oleylamine (OLA; 10 ml) were mixed under argon in a three-neck flask connected to a Schlenk line. The mixture was kept under vacuum for 30 min at room temperature to purify it from low boiling point impurities. Afterward, temperature was increased to 155 °C and 1-dodecanethiol (DDT; 7.7 mmol) was injected. The solution was maintained at this temperature for 15 min. Then, temperature was raised to 270 °C, and nanocrystals were allowed to grow for 30 min. CIGS nanoparticles were finally purified by multiple precipitation and re-dispersion steps using a mixture of toluene and ethanol in a ratio 2:1 for precipitation and toluene for re-dispersion.

2.2 CIGS nanoparticle-based ink formulation Dimethyl sulfoxide (DMSO) was used as a solvent due to its very low toxicity and its suitable boiling point and surface tension. To minimize the final carbon content of the film, no binder was used during ink formulation. The CIGS nanoparticle load was varied in the range between 1 and 60 $g\,L^{-1}$ to investigate the inorganic load on the final layer quality.

2.3 CIGS nanoparticle films A fully automated pulsed spray deposition system operated in open air conditions was used to produce the CIGS films from CIGS nanoparticle-based inks. Figure 1 displays the custom-made pulsed spray deposition system used in this work. The system used a pneumatic spray nozzle that employed nitrogen as the carrier gas and was controlled through an electrovalve. The substrate was vertically supported on a heated plate. The plate temperature and spray parameters, such as pulse time, number of spray pulses, and time between pulses, were monitored and controlled through a computer. CIGS nanoparticles were deposited over $2 \times 2\,cm^2$ Mo-coated soda-lime glass (SLG) substrates. The Mo layer was prepared by DC-magnetron sputtering using an Alliance Concepts AC450 system. Deposition conditions were selected to obtain 800 nm thick Mo layers with $R_s = 0.35\,\Omega\,sq^{-1}$.

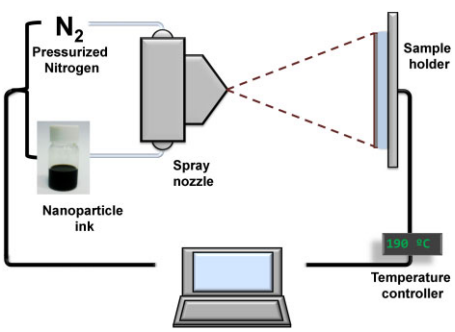

Figure 1 Schematic view of the pulsed spray deposition system used to produce CIGS nanoparticle films onto Mo-coated soda-lime glass substrates.

2.4 CIGS film crystallization/selenization Crystallization–selenization processes were carried out in the temperature range from 450 to 550 °C in a Se-rich atmosphere using a tubular furnace. The Se atmosphere was created by introducing 120 mg of elemental Se powder within the graphite box containing the sample.

3 Results and discussion

3.1 CIGS nanoparticles CIGS nanoparticles obtained by the above described procedure had an average particle size of 20 ± 5 nm as observed from transmission electron microscopy (TEM) characterization (Fig. 2). Composition could be adjusted in the whole range from $CuInS_2$ to $CuGaS_2$ by controlling the amounts of the different precursors. For the present work, we set the composition to $CuIn_{0.75}Ga_{0.25}S_2$. Single particle analysis showed all nanoparticles to contain the four elements, with a minor composition variation from particle to particle.

CIGS crystal structure was identified with wurtzite by X-ray diffraction (XRD) analysis (Fig. 2). We selected a synthesis procedure that yields wurtzite CIGS because the use of nanoparticles with metastable crystal structures has been reported to provide an additional driving force for film crystallization during the selenization process [22].

3.2 Ink formulation To create device-grade films from colloidal nanoparticles, one unavoidable step is to remove the long organic ligands that were used to control nanocrystal growth during its synthesis in solution. Nanoparticle ligands not only strongly compromise the film crystallization during the selenization treatment, but also result in relatively large amounts of carbon that accumulate

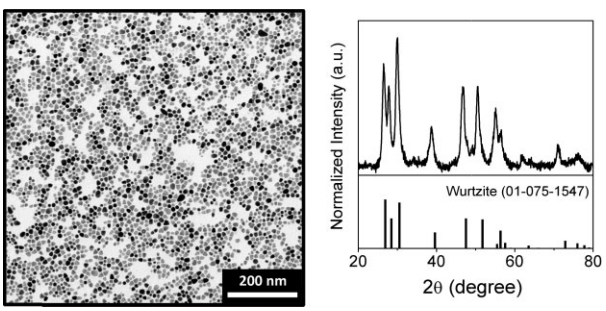

Figure 2 Representative TEM micrograph and XRD pattern of wurtzite CIGS nanoparticles.

between the absorber layer and the back electrode. To overcome this limitation, organics can be removed after deposition by treating the film with compounds such as hydrazine [23]. For this treatment to be effective, the thickness of the film to be treated is strongly limited. Therefore, this treatment would need to be implemented after each spray pulse, what strongly complicates the layer growth process. The use of highly toxic compounds is another important limitation of the organic removal after deposition.

Due to the unsolved limitations involved in the organic removal after nanoparticle deposition, a suitable alternative to get rid of surface ligands is to displace them from the nanoparticle surface while in solution. The main challenge of this strategy, especially for spray deposition, is to remove the surface ligands without compromising the ink stability. Thus, when removing the surface ligands that keep nanoparticles apart by steric repulsive forces, an electrostatic repulsion need to be introduced to prevent aggregation. This process is generally assisted by a change to a more polar solvent.

We displaced OLA from the nanoparticles surface using $(NH_4)_2S$, which is a particularly suitable compound to prepare sulfide-based inks [24, 25]. After ligand displacement, nanoparticles were dispersed in DMSO. The final ink was stable for long periods of time, above months.

3.3 Spray deposition Several spray deposition conditions, such as substrate temperature, pulse duration, pulse number, and time between spray pulses were carefully adjusted to obtain high quality CIGS thin films with a proper morphology, homogeneity, and thickness (Fig. 3).

To produce homogeneous films, substrate temperature needs to be high enough to ensure the solvent removal upon contact with the substrate surface. Too low substrate temperatures resulted in the formation of ink droplets on the substrate, which strongly compromised the film homogeneity. Too high temperatures were also detrimental as the evaporation of the solvent before reaching the film resulted in the deposition of rough layers formed by particle aggregates. In the present work, the substrate temperature was set to 190 °C, which is very close to the boiling point of the used solvent, DMSO.

As the nanoparticle ink was at ambient temperature when sprayed, to maintain the substrate temperature constant during deposition of the whole layer thickness, the pulse duration and the time between pulses had to be carefully adjusted. With each spray pulse, the substrate temperature decreased a magnitude proportional to the spray pulse duration. Therefore, too long pulses resulted in the formation of ink droplets, which translated in the growth of inhomogeneous films. Another important parameter was the time between pulses. Long enough times were needed to recover the substrate temperature. However, to increase the time between pulses would be obviously detrimental in terms of cost and productivity in an industrial scenario. The minimum time required depended on the duration of the pulse, the substrate temperature, the thermal inertia of the support, and the power of the heater. In our set-up, pulse duration was set to 400 ms and the time between pulses to 30 s.

The ink inorganic load was another key parameter determining the final quality of the layer. As shown in Fig. 2, the more concentrated the solution sprayed, the smoother the films obtained. A limit was found in the ink stability, associated with the nanoparticles solubility within the selected solvent. An unstable ink easily clogged the nozzle, which was an obvious limitation. We finally set the inorganic load of inks prepared from CIGS nanoparticles to 10 g L^{-1}.

Finally, all other parameters being the same, the number of pulses determined the film thickness. This is shown in Fig. 4, where a series of samples with thickness between 1.5 and 5.5 μm obtained by increasing the number of pulses from 10 to 40 are displayed. Notice after the crystallization/selenization treatment a factor 2 reduction of the film thickness was obtained. All the following characterizations have been performed on 1–2 μm thick films after annealing treatment.

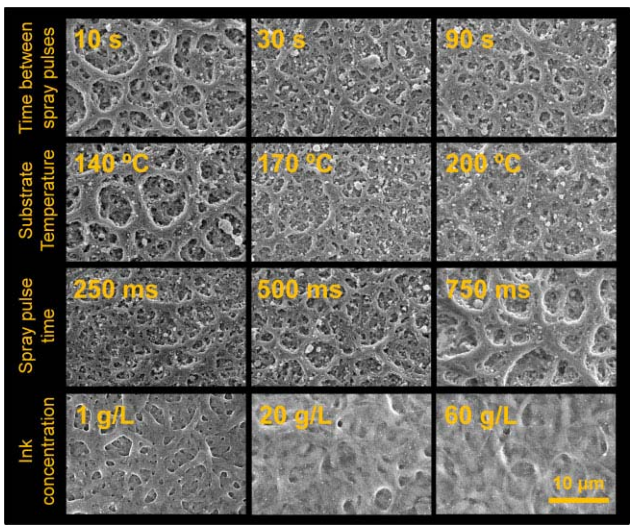

Figure 3 Top view SEM images of CIGS thin films obtained using different spray conditions: time between spray pulses (10–90 s), substrate temperatures (140–200 °C), spray pulse times (250–750 ms), and ink concentrations (1–60 g L^{-1}).

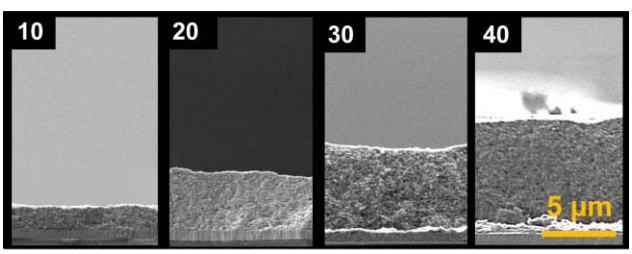

Figure 4 Cross-section SEM images of CIGS thin films prepared using a number of spray pulses between 10 and 40, as noted.

3.4 Film crystallization/selenization Films were crystallized in a tubular furnace in the presence of elemental selenium at temperatures in the range from 450 to 550 °C during 30 min. A complete replacement of the sulfur by selenium, transforming the precursor CIGS wurtzite film into CIGSe chalcopyrite film took place even at 450 °C as observed from XRD measurements (Fig. 5). In terms of chemical composition, the relative content of Ga and In was preserved during the selenization process as observed from energy dispersive X-ray spectroscopy (EDX). No significant amounts of carbon were detected in the CIGS nanoparticle-based films after the crystallization/selenization treatment.

Homogeneous films composed of a small-grained layer close to the back contact and covered with a top region with larger and more crystalline grains, were obtained after crystallization at 500 and 550 °C (Fig. 6, left column). This bi-layer structure is commonly observed in sintered ink-based absorbers.

To further promote the nanoparticle-based film crystallization, a boost of the ionic diffusion and atomic reorganization was required. In this direction, we assessed the potential of extrinsic metal ions to promote crystallization. Bi and Sb have been proposed as crystallization inducers in thin films of CIGS and related compounds [17, 18, 24]. While the crystallization induction mechanism is not understood in detail, it is accepted to be based on the local formation of a low melting point Bi/Sb-based alloy at the grain surface. The decrease of the ion diffusion energy associated with the external metal ion incorporation ultimately promotes the diffusion-controlled crystallization process.

In CIGS films grown by vacuum-based techniques, external impurities can be co-deposited or introduced at the film surface using an additional step. When producing CIGS thin films from nanoparticle-based inks, one very suitable strategy to introduce external crystallization promoters is to take advantage of the ligand exchange step required to remove the ligands used in the nanoparticle synthesis. Thus, instead of $(NH_4)_2S$, we used $BiCl_3$ and $SbCl_3$ to displace the long aliphatic chains and at the same time introduce Bi or Sb ions on the nanoparticle surface.

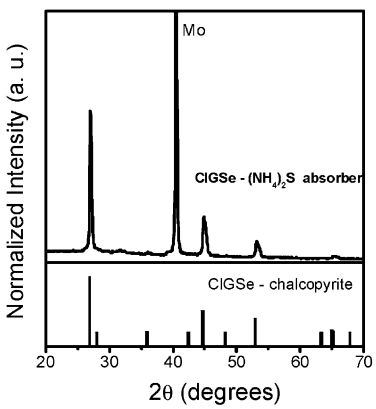

Figure 5 XRD pattern of the crystallized/selenized CIGSe absorber.

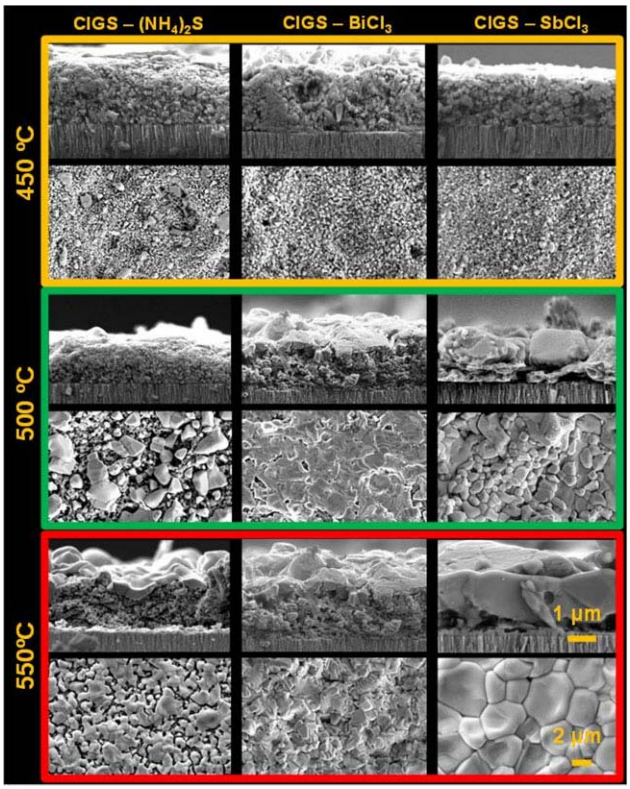

Figure 6 Cross-section and top-view SEM images of CIGS-$(NH_4)_2S$, CIGS-$BiCl_3$, and CIGS-$SbCl_3$ thin films after selenization at 450, 500, and 550 °C.

After ligand exchange, the initial CIGS inks contained a percentage of around 5% of Bi or Sb, as determined by inductively coupled plasma optical emission spectroscopy (ICP). To investigate the effect of the Bi and Sb incorporation, we annealed CIGS-$(NH_4)_2S$, CIGS-$BiCl_3$, and CIGS-$SbCl_3$ nanoparticle-based films in the temperature range from 450 to 550 °C in a Se atmosphere during 30 min. Figure 6 displays cross-section and top view SEM images of the films produced after the crystallization/selenization of the CIGS-$(NH_4)_2S$, CIGS-$BiCl_3$, and CIGS-$SbCl_3$ nanoparticle-based films. While small-grained layers were obtained from CIGS-$(NH_4)_2S$ samples processed at temperatures between 450 and 550 °C, the introduction of Bi slightly promoted the crystal growth at low temperatures (450 and 500 °C). However, the incorporation of Bi did not allow the formation of fully crystalline layers even after sintering at 550 °C. In contrast, highly crystalline films, showing crack free and well crystallized surfaces, were obtained from the CIGS-$SbCl_3$ precursors after sintering at 500 and 550 °C, demonstrating the large potential of Sb to promote crystal growth. The introduction of Sb ions at the nanoparticles surface resulted in the formation of a low melting point Sb-based chalcogenide, which locally increased ionic mobility and thus the material capacity for mass transfer and reorganization. As crystallization proceeded and crystal domains grew, Sb was accumulated at the crystal surface.

After the annealing treatment at 500 °C or above, no Bi or Sb was detected within the CIGSe film. These results suggest that Bi and Sb did not incorporate to the bulk CIGSe crystals but evaporated during the selenization process. The elimination of the external element from the final layer is important to ensure it does not negatively influence the final optoelectronic properties of the device.

4 Conclusions To produce smooth and highly homogeneous nanoparticles films using pulsed spray deposition, short spray pulses, large enough times from pulse to pulse, substrate temperatures close to the solvent boiling point, and inks with inorganic loads as high as possible are necessary. These films crystallize forming a bi-layer structure, with small grains close to the back contact and a top region with larger crystal domains. The use of crystallization promoters such as Sb, allows to fully crystalline the films at temperatures as low as 500 °C.

Acknowledgement This work has been funded by the Scalenano project (NMP4-LA-2011-284486) from the FP7 program.

References

[1] P. Jackson, D. Hariskos, E. Lotter, S. Paetel, R. Wuerz, R. Menner, W. Wischmann, and M. Powalla, Prog. Photovolt.: Res. Appl. **19**, 894 (2011).
[2] http://www.solar-frontier.com/eng/news/2014/C031367.html.
[3] D. Lee and K. Yong, Korean J. Chem. Eng. **30**, 1347 (2013).
[4] T. K. Todorov, O. Gunawan, T. Gokmen, and D. B. Mitzi, Prog. Photovolt.: Res. Appl. **21**, 82 (2013).
[5] V. A. Akhavan, B. W. Goodfellow, M. G. Panthani, C. Steinhagen, T. B. Harvey, C. J. Stolle, and B. A. Korgel, J. Solid State Chem. **189**, 2 (2012).
[6] V. A. Akhavan, B. W. Goodfellow, M. G. Panthani, D. K. Reid, D. J. Adachi, and B. A. Korgel, Energy Environ. Sci. **3**, 1600 (2010).
[7] T. K. Todorov, K. B. Reuter, and D. B. Mitzi, Adv. Mater. **22**, E156 (2010).
[8] Q. Guo, G. M. Ford, R. Agrawal, and H. W. Hillhouse, Prog. Photovolt.: Res. Appl. **21**, 64 (2013).
[9] M. Ibáñez, R. Zamani, A. LaLonde, D. Cadavid, W. Li, A. Shavel, J. Arbiol, J. R. Morante, S. Gorsse, G. J. Snyder, and A. Cabot, J. Am. Chem. Soc. **134**, 4060 (2012).
[10] A. Shavel, D. Cadavid, M. Ibáñez, A. Carrete, and A. Cabot, J. Am. Chem. Soc. **134**, 1438 (2012).
[11] M. Ibáñez, D. Cadavid, R. Zamani, N. García-Castelló, V. Izquierdo-Roca, W. Li, A. Fairbrother, J. D. Prades, A. Shavel, J. Arbiol, A. Pérez-Rodríguez, J. R. Morante, and A. Cabot, Chem. Mater. **24**, 562 (2012).
[12] M. Ibáñez, R. Zamani, W. Li, A. Shavel, J. Arbiol, J. R. Morante, and A. Cabot, Cryst. Growth Des. **12**, 1085 (2012).
[13] C. N. Bucherl, K. R. Oleson, and H. W. Hillhouse, Curr. Opin. Chem. Eng. **2**, 168 (2013).
[14] C. J. Stolle, T. B. Harney, and B. A. Korgel, Curr. Opin. Chem. Eng. **2**, 160 (2013).
[15] Q. Guo, G. M. Ford, H. W. Hillhouse, and R. Agrawal, Nano Lett. **9**, 3060 (2009).
[16] B. Walker and R. Agrawal, 38th IEEE Photovoltaic Specialists Conference (PVSC), 002654, June (2012).
[17] Y. Xiang, X. Zhang, and S. Zhang, J. Solid State Chem. **204**, 278 (2013).
[18] M. Yuan, D. B. Mitzi, W. Liu, A. J. Kellock, S. Jay Chey, and V. R. Deline, Chem. Mater. **22**, 285 (2010).
[19] T. B. Harvey Isao Mori, C. Jackson Stolle, T. D. Bogart, D. P. Ostrowski, M. S. Glaz, J. Du, D. R. Pernik, V. A. Akhavan, H. Kesrouani, D. A. Vanden Bout, and B. A. Korgel, ACS Appl. Mater. Interfaces **5**, 9134 (2013).
[20] Z. Z. Fang, Sintering of Advanced Materials: Fundamentals and Processes (Oxford, Woodhead Publishing, 2010).
[21] C. Coughlan, A. Singh, and K. M. Ryan, Chem. Mater. **25**, 653 (2013).
[22] R. Mainz, A. Singh, S. Levcenko, M. Klaus, C. Genzel, K. M. Ryan, and T. Unold, Nature Commun. **5**, 3133 (2014).
[23] D. V. Talapin and C. B. Murray, Science **310**, 86 (2005).
[24] A. Carrete, A. Shavel, X. Fontané, J. Montserrat, J. Fan, M. Ibáñez, E. Saucedo, A. Perez-Rodriguez, and A. Cabot, J. Am. Chem. Soc. **135**, 15982 (2013).
[25] X. Yu, X. An, A. Shavel, M. Ibañez, and A. Cabot, J. Mater. Chem. A **2**, 12317 (2014).

JACS
JOURNAL OF THE AMERICAN CHEMICAL SOCIETY

Communication

pubs.acs.org/JACS

Continuous Production of Cu_2ZnSnS_4 Nanocrystals in a Flow Reactor

Alexey Shavel,[‡] Doris Cadavid,[‡] Maria Ibáñez,[†] Alex Carrete,[‡] and Andreu Cabot*[,†,‡]

[†]Departament Electronica, Universitat de Barcelona, Barcelona 08028, Spain

[‡]Catalonia Institute for Energy Research (IREC), Jardí de les Dones de Negre 1, Planta 2, 08930 Sant Adrià del Besós, Barcelona, Spain

Supporting Information

ABSTRACT: A procedure for the continuous production of Cu_2ZnSnS_4 (CZTS) nanoparticles with controlled composition is presented. CZTS nanoparticles were prepared through the reaction of the metals' amino complexes with elemental sulfur in a continuous-flow reactor at moderate temperatures (300−330 °C). High-resolution transmission electron microscopy and X-ray diffraction analysis showed the nanocrystals to have a crystallographic structure compatible with that of the kesterite. Chemical characterization of the materials showed the presence of the four elements in each individual nanocrystal. Composition control was achieved by adjusting the solution flow rate through the reactor and the proper choice of the nominal precursor concentration within the flowing solution. Single-particle analysis revealed a composition distribution within each sample, which was optimized at the highest synthesis temperatures used.

Copper-based quaternary chalcogenides have recently attracted a great deal of attention as low-cost alternatives to conventional absorber materials in photovoltaics.[1,2] Among them, Cu_2ZnSnS_4 (CZTS), which has a 1.45−1.51 eV band gap and a high optical absorption coefficient (>10^4 cm^{-1}), is specially suited for this application.[1] Surprisingly, solution-processed CZTS absorber layers have recently provided photovoltaic efficiencies of up to 10%,[1] much higher than those obtained by vacuum-deposition techniques. This unprecedented goal is probably related to better control of the composition and crystal-phase homogeneity obtained in such a complex quaternary material by solution processing techniques in comparison with vacuum-based ones. At the same time, CZTS shows promising thermoelectric properties, with ZT values of up to 0.36 at 700 K.[3] In this field, control of the materials composition has also been shown to be fundamental for optimization of its functional properties.[3]

CZTS layers have previously been prepared by the decomposition of drop-cast solutions of metal salts[4] or of the constituent binary semiconductors in hydrazine.[1a] Nevertheless, the preparation of CZTS inks from quaternary CZTS nanoparticles is still the method that potentially can yield layers with superior compositional homogeneity.[5−7]

The classical colloidal synthesis procedure based on the decomposition of organometallic precursors is well-established and widely used. Variations of this basic procedure allow the preparation of high-quality nanocrystals of a plethora of different materials.[8] However, these synthetic routes have usually been developed and optimized for the production of small amounts of material, which are insufficient for most practical applications. This synthetic strategy is also too labor-intensive to provide a sufficient amount of material by multiple small-scale batch production. Moreover, batch-to-batch repetitivity may also become an unsolvable problem in a potential attempt to produce large amounts of materials by this method. The obvious scale-up procedure derived from classical colloidal synthesis routes is to maintain the synthetic conditions and concentrations optimized for small batches but to increase the total volume of solvent and thus the size of the reaction receptacle to the required production amount. This simple scale-up technique inevitably results in a degradation of the product homogeneity because of the reduced thermal and compositional uniformity of large volumes of solution, especially in the need of a hot injection step.

Maximization of the solution homogeneity, in terms of composition and temperature, is key for producing nanomaterials with highly uniform and well-controlled characteristics. While a proper escalation of the homogenizing and heating mechanisms is indispensable, the heating and mixing volumes used also must be minimized because of the insufficient thermal and mass transport properties of the solvent. Thus, the natural scale-up procedure for obtaining large amounts of high-quality nanomaterials consist of using a very high frequency of identical and automated batch-to-batch events with relatively small volume batches. In the high-frequency limit, this procedure translates into an automated continuous-flow synthesis procedure.

Several groups have developed microfluidic systems for continuous production of nanoparticles. These previous works focused on the degree of control over the nanoparticle properties offered by this technology but ignored its scale-up potential.[7−11] In spite of all its advantages, very few reports have been devoted to the large-scale synthesis of nanoparticles in macroscopic flow reactors. Among them, the synthesis of silver nanoparticles[9] and of CdSe[10] and SnTe nanorods[11] in stainless steel reactors and in relatively thick polymeric (1/16 in) and silica glass capillaries (0.2−0.5 mm) should be mentioned, though authors referred to this last system as microfluidic.

Here we report a successful continuous production method to obtain relatively large amounts of quaternary chalcogenide

Received: October 20, 2011
Published: January 2, 2012

dx.doi.org/10.1021/ja209688a | J. Am. Chem.Soc. 2012, 134, 1438−1441

nanoparticles, in particular CZTS, with controlled composition. The procedure was used for the preparation of grams of this material with controlled composition under open-air conditions.

Figure 1A shows a scheme of the experimental setup used. The precursor solution for the continuous-flow process was

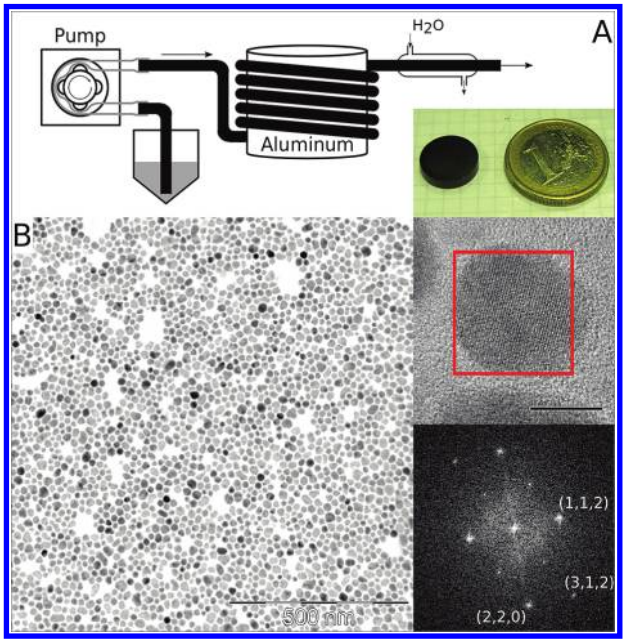

Figure 1. (A) Scheme of the flow reactor setup and image of a 1 g pellet made of CZTS nanoparticles. (B) TEM micrograph of cleaned CZTS nanoparticles prepared inside the flow reactor at 300 °C at a flow rate of 2.0 mL/min. The inset shows an HRTEM image of a CZTS nanocrystal and the corresponding SAED pattern.

prepared by dissolving tin(IV) and copper(II) chlorides and zinc oxide in an oleylamine (OAm, 70%, Aldrich)/octadecene (ODE) mixture. In a typical preparation, 2.0 mmol of $CuCl_2{\cdot}H_2O$ (98%, Aldrich) and 1.0 mmol of $SnCl_4{\cdot}5H_2O$ (98%, Aldrich) were initially dissolved in a small amount of tetrahydrofuran (THF) to enhance the solubility of the tin(IV) chloride in OAm. After complete dissolution, 1.0 mmol of ZnO and a certain amount of OAm were added into the solution. The mixture was heated to 50−80 °C in a rotary evaporator. After complete dissolution of the ZnO, the pressure inside the evaporator was reduced to 5−10 mbar to remove THF and any other light products present in the reaction mixture. Just before the synthesis, specific amounts of sulfur and ODE were added to the solution containing the metal complexes. To purify the solution further from any low-boiling-point impurities (e.g., water or light-hydrocarbon impurities from ODE), the mixture was kept at 50 °C and 10 mbar until the sulfur was completely dissolved. The prepared precursor solution was pumped through a 1 m long bronze tube having a 3 mm internal diameter and kept at a temperature in the range 300−320 °C. The flow rate was typically set within the range 1−5 mL/min. The reaction product was collected and washed several times by precipitation with isopropanol and redispersion in chloroform. The final product was readily soluble in various organic solvents (e.g., chloroform, THF, hexane).

A representative transmission electron microscopy (TEM) image of the CZTS nanoparticles produced at 300 °C is shown in Figure 1B. While the nanoparticle size distribution was fairly narrow, full shape and size control is still not available by this method for such complex quaternary materials. In the inset, a high-resolution TEM (HRTEM) image of a few selected particles and a selected-area electron diffraction (SAED) image of a single nanocrystal are also displayed to show the crystallinity of the obtained products.

The X-ray diffraction (XRD) patterns and Raman spectra of the nanoparticles before and after a sintering treatment at 500 °C (Figure 2) confirmed the crystallographic structure of the

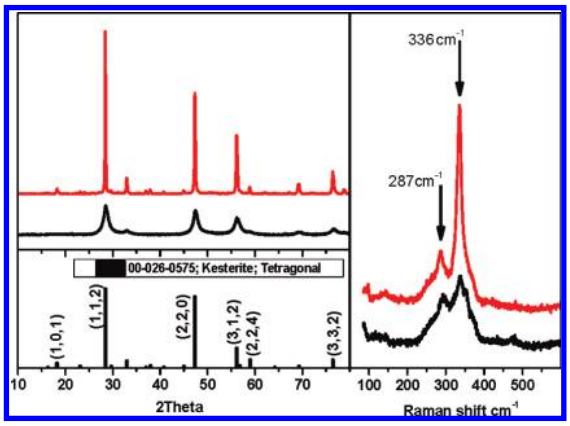

Figure 2. (left) XRD patterns and (right) Raman spectra of the prepared nanoparticles before (black) and after (red) annealing at 500 °C for 1 h. As a reference, the diffraction pattern of Cu_2ZnSnS_4 (JCPDS no. 00-026-0575) is shown. The lattice parameters for the heated sample were $a = b = 5.40$ Å and $c = 10.40$ Å.

nanocrystals to be compatible with that of CZTS (JCPDS no. 00-026-0575; tetragonal kesterite). CZTS typically crystallizes in a kesterite-type structure (space group $I\bar{4}2m$) with two tetrahedral structural units, $[Cu_2S]$ and $[SnZnS_4]$,[12] although CZTS with a wurzite-type crystal structure has recently been reported.[13] This structure can be derived from zinc blende ZnS by partial substitution of Zn with Cu and Sn.[14] The Raman peaks at 336 and 287 cm^{-1} are the main features of the kesterite-type structure, as previously reported for CZTS.[15]

The materials composition was analyzed by scanning electron microscopy−energy-dispersive X-ray spectroscopy (SEM−EDX). For SEM−EDX characterization, the nanoparticles were drop-cast on a silicon substrate. Quite conveniently, the different reaction kinetics of Cu, Zn, and Sn with S allowed us to control the nanoparticle composition over a relatively wide range by appropriately adjusting the precursor concentrations, the reaction temperature, and the flow rate (i.e., the reaction time). Figure 3A shows how the nanoparticles composition depends on the synthesis conditions [see the Supporting Information (SI) for details]. In particular, increasing the flow rate of the solution through the reactor afforded nanoparticles with higher Cu content. From our results, it became evident that the kinetics of the reaction of each element with the sulfur precursor is the fastest for Cu and the slowest for Zn. We believe that initially Cu_2S nanocrystals may nucleate, while first Sn ions and then Zn gradually enter into the nanocrystal structure as the solution advances inside the reaction tube. Lower reaction temperatures extended the time spread needed for the complete incorporation of Zn and Sn ions inside the CZTS crystal structure, thus reducing the possible flow rates available for the formation of stoichiometric nanoparticles.

dx.doi.org/10.1021/ja209688a | J. Am. Chem.Soc. 2012, 134, 1438−1441

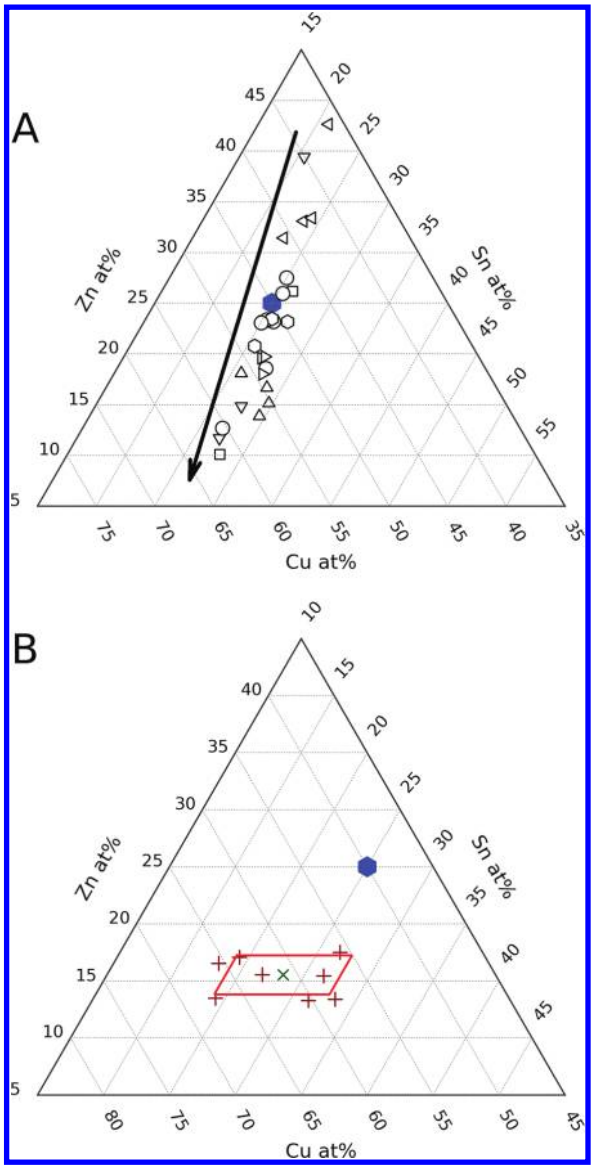

Figure 3. (A) CZTS cationic ratios obtained from SEM–EDX. The arrow points the direction of increasing flow rate. Different symbols denote different reaction conditions (see the SI). (B) Single-particle composition (red +) obtained by HRTEM–EDX analysis of a number of CZTS nanoparticles synthesized at 315 °C. The green × shows the mean composition obtained by averaging the values obtained from several nanoparticles. The blue hexagon in each graph shows the nominal composition of the precursor solution.

It is worth mentioning that although quite a broad range of CZTS compositions were accessible by this procedure, only compositions close to the stoichiometric one were stable after annealing treatments above 500 °C, confirming the narrow stability spot of the CZTS phase.[16] Phase segregation was observed during the annealing treatment for nanoparticles with compositions far from the stoichiometric one (see the SI).

Single-particle HRTEM–EDX analysis confirmed that all of the nanoparticles contained all four elements. However, these analyses also demonstrated the existence of a distribution of nanoparticle compositions within each sample. In this regard, a previous publication demonstrated that while the average composition of a sample of $Cu_2ZnSnSe_4$ nanoparticles produced at relatively low temperature (230 °C) by a heating-up procedure was close to the stoichiometric one, large particle-to-particle compositional variations existed.[17] Figure 3B shows the compositions of several single CZTS nanoparticles prepared at 315 °C. It was experimentally observed that the nanoparticle composition distribution was strongly dependent on the reaction temperature; the lower the reaction temperature, the broader the nanoparticle composition distribution within each sample. As an example, samples prepared at 300 °C showed much larger particle-to-particle compositional differences than those obtained at 315 °C, which showed a fairly good composition homogeneity (see the SI). Notably, no particle with elemental, binary, or ternary composition was found among the several tens of particles checked within each sample.

To measure the thermoelectrical properties of the obtained CZTS nanoparticles, several grams of material were prepared. For these measurements, the CZTS nanoparticles were treated with a formamide solution of $[NH_4]_2S$ (20% in water) to remove long-chain organic stabilizers[18] (see the SI for details of the ligand-exchange procedure). The resulting nanoparticles were dried, and the obtained nanopowders were pressed into 13 mm pellets by applying 5 tons of force with a hydraulic press. The materials were then heated to 500 °C in a N_2 atmosphere and maintained at this temperature for 1 h.

The Seebeck coefficient (S) and electrical resistivity of a stoichiometric CZTS sample were characterized over the temperature range 50–350 °C using static direct-current and standard four-probe methods, respectively (Figure 4). Measurements were simultaneously carried out under a He atmosphere in an LSR-3 system (LINSEIS). While the Seebeck coefficients obtained for the CZTS nanoparticles were fairly good, the sample resistivity was relatively high. The low electrical conductivities obtained resulted in moderated power factors in the range 0.01–0.1 mW m^{-1} K^{-2}.

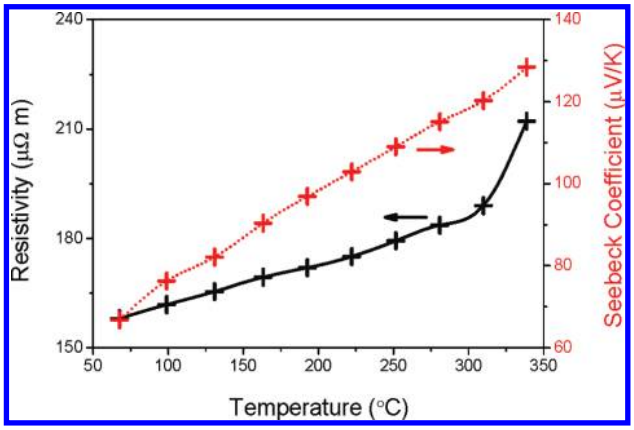

Figure 4. Resistivity and Seebeck coefficient of CZTS nanoparticles pressed into a pellet.

In conclusion, a successful route for the continuous production of Cu_2ZnSnS_4 (CZTS) nanoparticles has been presented. The preparation procedure allows simple and efficient control of the nanoparticle composition over a wide range. The route was used for the preparation of several grams of CZTS nanoparticles, which were used for the thermoelectric characterization of this material in a nanocrystalline form. Single-particle HRTEM–EDX analysis confirmed the presence of all four elements within each nanocrystal and demonstrated a narrow compositional distribution among nanoparticles within

dx.doi.org/10.1021/ja209688a | J. Am. Chem.Soc. 2012, 134, 1438–1441

each sample. The nanoparticle composition distribution was minimized at the highest reaction temperatures used.

■ ASSOCIATED CONTENT

Supporting Information

XRD pattern of the Sn-rich CZTS sample, distribution of the elements in nanoparticles synthesized at 300 °C, and details of the synthesis parameters used and the ligand-exchange procedure. This material is available free of charge via the Internet at http://pubs.acs.org.

■ AUTHOR INFORMATION

Corresponding Author

acabot@irec.cat

■ ACKNOWLEDGMENTS

This work was supported by the Spanish MICINN Projects MAT2008-05779, MAT2008-03400-E/MAT, CDS2009-00050, CSD2009-00013, and ENE2008-03277-E/CON. M.I. thanks the Spanish MICINN for her Ph.D. grant. A.C. is thankful for financial support through the Ramón y Cajal Program.

■ REFERENCES

(1) (a) Todorov, T. K.; Reuter, K. B.; Mitzi, D. B. *Adv. Mater.* **2010**, *22*, E156. (b) Guo, Q.; Ford, G. M.; Yang, W.-C.; Walker, B. C.; Stach, E. A.; Hillhouse, H. W.; Agrawal, R. *J. Am. Chem. Soc.* **2010**, *132*, 17384. (c) Mitzi, D. B.; Gunawan, O.; Todorov, T. K.; Wang, K.; Guha, S. *Sol. Energy Mater. Sol. Cells* **2011**, *95*, 1421.

(2) Shavel, A.; Arbiol, J.; Cabot, A. *J. Am. Chem. Soc.* **2010**, *132*, 4514.

(3) Liu, M.-L.; Chen, I.-W.; Huang, F.-Q.; Chen, L.-D. I. *Adv. Mater.* **2009**, *21*, 3808.

(4) Fischereder, A.; Rath, T.; Haas, W.; Amenitsch, H.; Albering, J.; Meischler, D.; Larissegger, S.; Edler, M.; Saf, R.; Hofer, F.; Trimmel, G. *Chem. Mater.* **2010**, *22*, 3399.

(5) Riha, S. C.; Parkinson, B. A.; Prieto, A. L. *J. Am. Chem. Soc.* **2009**, *131*, 1205.

(6) Guo, Q.; Hillhouse, H. W.; Agrawal, R. *J. Am. Chem. Soc.* **2009**, *131*, 1167.

(7) Steinhagen, C.; Panthani, M. G.; Akhavan, V.; Goodfellow, B.; Koo, B.; Korgel, B. A. *J. Am. Chem. Soc.* **2009**, *131*, 12554.

(8) (a) Ibáñez, M.; Guardia, P.; Shavel, A.; Cadavid, D.; Arbiol, J.; Morante, J. R.; Cabot, A. *J. Phys. Chem. C* **2011**, *115*, 7947. (b) Li, W.; Shavel, A.; Guzman, R.; Rubio-Garcia, J.; Flox, C.; Fan, J.; Cadavid, D.; Ibáñez, M.; Arbiol, J.; Morante, J. R.; Cabot, A. *Chem. Commun.* **2011**, *47*, 10332.

(9) (a) Lin, X. Z.; Terepka, A. D.; Yang, H. *Nano Lett.* **2004**, *4*, 2227. (b) Huang, J.; Lin, L.; Li, Q.; Sun, D.; Wang, Y.; Lu, Y.; He, N.; Yang, K.; Yang, X.; Wang, H.; Wang, W.; Lin, W. *Ind. Eng. Chem. Res.* **2008**, *47*, 6081.

(10) (a) Nakamura, H.; Yamaguchi, Y.; Miyazaki, M.; Maeda, H.; Uehara, M.; Mulvaney, P. *Chem. Commun.* **2002**, 2844. (b) Kawa, M.; Morii, H.; Ioku, A.; Saita, S.; Okuyama, K. *J. Nanopart. Res.* **2003**, *5*, 81.

(11) Jin, H. D.; Chang, C.-H. *J. Mater. Chem.* **2011**, *21*, 12218.

(12) Liu, M. L.; Huang, F. Q.; Chen, L. D.; Chen, I. W. *Appl. Phys. Lett.* **2009**, *94*, No. 202103.

(13) Lu, X.; Zhuang, Z.; Peng, Q.; Li., Y. *Chem. Commun.* **2011**, *47*, 3141.

(14) Chen, S.; Gong, X.; Walsh, A.; Wei, S. *Phys. Rev. B* **2009**, *79*, No. 165211.

(15) (a) Mitzi, D. B.; Gunawan, O.; Todorov, T. K.; Wang, K.; Guha, S. *Sol. Energy Mater. Sol. Cells* **2011**, *95*, 1421. (b) Shi, L.; Pei, C.; Xu, Y.; Li, Q. J *.J. Am. Chem. Soc.* **2011**, *133*, 10328.

(16) Olekseyuk, I. D.; Dudchak, I. V.; Piskach, L. V. *J. Alloys Compd.* **2004**, *368*, 135.

(17) Haas, W.; Rath, T.; Pein, A.; Rattenberger, J.; Trimmel, G.; Hofer, F. *Chem. Commun.* **2011**, *47*, 2050.

(18) Nag, A.; Kovalenko, M. V.; Lee, J.-S.; Liu, W.; Spokoyny, B.; Talapin, D. V. *J. Am. Chem. Soc.* **2011**, *133*, 10612.

JACS
JOURNAL OF THE AMERICAN CHEMICAL SOCIETY
Communication
pubs.acs.org/JACS

Antimony-Based Ligand Exchange To Promote Crystallization in Spray-Deposited $Cu_2ZnSnSe_4$ Solar Cells

Alex Carrete,[†] Alexey Shavel,[†] Xavier Fontané,[†] Joana Montserrat,[‡] Jiandong Fan,[†] Maria Ibáñez,[†] Edgardo Saucedo,[†] Alejandro Pérez-Rodríguez,[†,‡] and Andreu Cabot*[,†,‡]

[†]Catalonia Energy Research Institute - IREC, Jardí de les Dones de Negre 1, Sant Adria del Besos, Barcelona, 08930, Spain
[‡]Departament d'Electrònica, Universitat de Barcelona, Barcelona 08028, Spain

Supporting Information

ABSTRACT: A multistrategy approach to overcome the main challenges of nanoparticle-based solution-processed $Cu_2ZnSnSe_4$ thin film solar cells is presented. We developed an efficient ligand exchange strategy, using an antimony salt, to displace organic ligands from the surface of Cu_2ZnSnS_4 nanoparticles. An automated pulsed spray-deposition system was used to deposit the nanoparticles into homogeneous and crack-free films with controlled thickness. After annealing the film in a Se-rich atmosphere, carbon-free and crystalline $Cu_2ZnSnSe_4$ absorber layers were obtained. Not only was crystallization promoted by the complete removal of organics, but also Sb itself played a critical role. The Sb-assisted crystal growth is associated with the formation of a Sb-based compound at the grain boundaries, which locally reduces the melting point, thus promoting the film diffusion-limited crystallization.

Cu_2ZnSnS_4 (CZTS) and $Cu_2ZnSnSe_4$ (CZTSe), composed of abundant and low-toxicity elements, are the main alternative to conventional absorber materials in thin film solar cells. CZTS and CZTSe thin films can be produced by conventional vacuum-based technologies, such as sputtering, evaporation or pulsed laser deposition. However, these technologies are neither particularly low-cost nor versatile for the production of large area devices, because of the relatively high energies and controlled atmospheres they require and the low growth rates and material yields they have associated. Alternative low cost solution-processing methods allow the preparation of large area thin film semiconductors at low temperatures and at high production rates and yields. Unprecedentedly, for CZTS/CZTSe solar cells, solution-processing technologies have also achieved significantly higher device efficiencies than conventional vacuum-based technologies.[1] This improved performance is associated with the excellent compositional and phase control achieved by solution-based methods in such complex quaternary materials.[2]

Nevertheless, solution-based technologies are not without limitations. The main challenges still encountered when producing large area thin films by solution-processing methods based on the deposition of nanoparticles are the following: (i) The formation of cracks due to the high deposition rates and the volume reduction associated with the organics removal. (ii) The poor crystallinity of the as-deposited precursor films, which require a posterior thermal treatment. (iii) The organics used during material synthesis and ink formulation and the residual carbon left after their thermal decomposition strongly deteriorate the film electronic properties and block its crystallization.

A multistrategy approach to overcome these limitations is presented here. We used a custom-made automated pulsed spray deposition system to produce CZTS films from colloidal CZTS nanoparticles having carefully adjusted compositions and organic free surfaces. Organic ligands used during nanoparticle synthesis were displaced by an antimony salt. We demonstrate here the effectiveness of these approaches to produce highly homogeneous, organic- and crack-free films. These films were annealed in a Se atmosphere to obtain CZTSe absorber layers. We further demonstrate that the Sb-based ligand exchange strategy not only eliminates carbon from the final film, thus improving electrical conductivity, but also strongly promotes crystal growth before Sb is completely removed from the film.

CZTS nanoparticles were prepared by the reaction of copper, tin and zinc salts with tetraethylthiouram disulfide in the presence of octadecylphosphonic acid (ODPA) and oleylamine (OLA). We believe OLA controls the nanoparticle growth and its stability. On the other hand, ODPA allows a better control of composition by coordinating with the precursor salts and facilitating their incorporation into the final crystal structure. ODPA does not remain attached to the nanoparticle surface, thus it was easily removed during the purification process and only OLA remained as an organic impurity.

Figure 1 shows representative TEM and HRTEM micrographs of the ~25 ± 5 nm CZTS nanoparticles produced by this procedure (see Supporting Information, SI). Composition could be tuned by changing the amount of precursors in the initial solution. Taking into account that highest CZTSe solar cell efficiencies were obtained from copper-poor and zinc-rich CZTSe,[1,3] to study ligand exchange procedures, crystallization and selenization processes and to fabricate CZTSe solar cells, we produced CZTS nanoparticles with the composition $Cu_{1.9}Zn_{1.1}Sn_{1.0}S_{4.0}$, as measured by EDX.

Even when organic ligands can be decomposed by an annealing process, their carbon footprint still limits the device performance and blocks the crystal growth.[4] Furthermore, cracks are usually formed when removing organics after deposition. Therefore, to produce solar cell grade thin films,

Received: July 5, 2013

   dx.doi.org/10.1021/ja4068639 | J. Am. Chem. Soc. XXXX, XXX, XXX–XXX

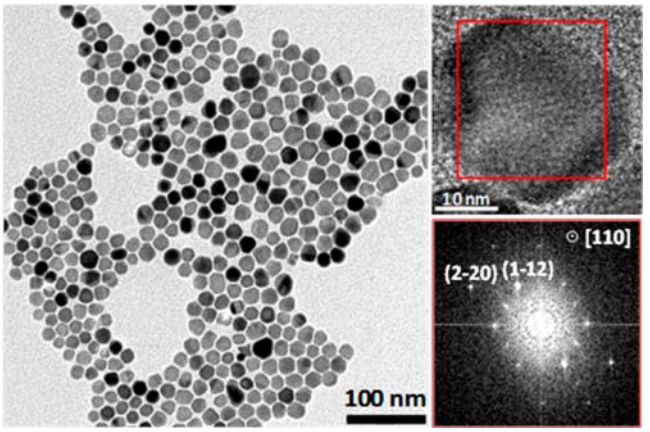

Figure 1. TEM and HRTEM micrograph, and power spectrum analysis of CZTS nanoparticles.

organics need to be displaced from the nanoparticle surface before deposition.

However, to process the materials in solution and to obtain homogeneous films, nanoparticles need to be soluble in a liquid carrier. Thus, either we use thick solvents and binders that keep nanoparticles dispersed during long enough times, which will again leave large amounts of carbon after decomposition, or we replace the organic ligands used during the synthesis by shorter but still effective stabilizers.[5] In this last direction, inorganic salts are excellent candidates to displace organic ligands and render the nanoparticles soluble in low boiling point solvents that after deposition can be easily evaporated without a carbon footprint. The use of inorganic salts gives also the opportunity to tune the final film composition or to introduce external dopants that control the material electronic properties.[6] While we chose to control the film composition at the nanoparticle synthesis stage, we tested multiple ligand exchange agents looking for the one that did not change the film composition but helped its crystallization. Among the different salts tested, best results were obtained for $SbCl_3$.

OLA displacement with $SbCl_3$ was carried out using a biphase system (Figure 2). We mixed in a 2:1 ratio a 0.1 M

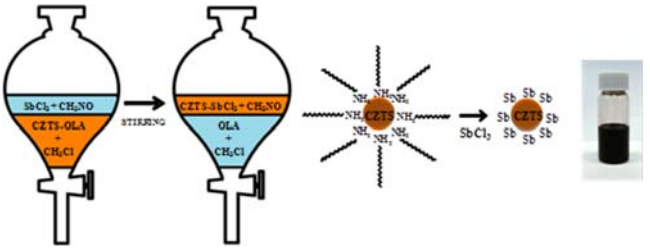

Figure 2. Schematized view of the procedure followed for the OLA displacement with $SbCl_3$.

$SbCl_3$ solution in formamide with a 10 g/L solution of nanoparticles in chloroform. Then, the solution was vigorously shaken until nanoparticles transferred to the formamide phase. The formamide solution was afterward washed several times with chloroform to drag all remaining organic ligands. Nanoparticles were finally precipitated with acetonitrile and redispersed in *N*,*N*-dimethylformamide (DMF) at a 5 g/L concentration. As a reference, we also replaced OLA with a relatively more conventional species, $(NH_4)_2S$, using a similar procedure. $(NH_4)_2S$ ligand exchange was performed by adding 1 mL of a 20 wt % $(NH_4)_2S$ solution in water and 10 mL of formamide into a 10 mL of a 10 g/L solution of CZTS nanoparticles in chloroform.

Figure 3b shows the mass loss as a function of temperature for CZTS-OLA, CZTS-$SbCl_3$ and CZTS-$(NH_4)_2S$ nano-

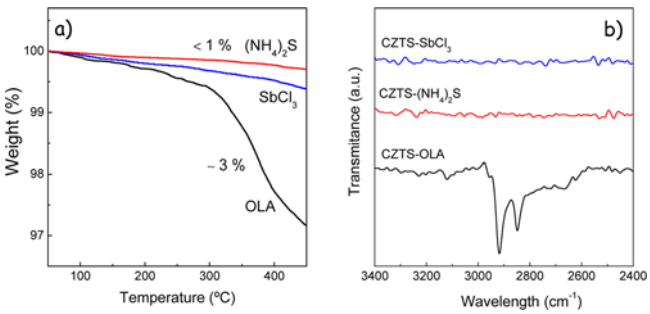

Figure 3. (a) TGA and (b) ATR-FTIR spectra from CZTS-OLA, CZTS-$SbCl_3$ and CZTS-$(NH_4)_2S$ nanoparticles.

particles. A relative mass decrease of a 3% was measured for purified CZTS-OLA nanocrystals when heated to 450 °C under a nitrogen flow. On the other hand, after $(NH_4)_2S$ and $SbCl_3$ ligand exchange, nanocrystals showed a mass loss of less than 1% associated to the evaporation of S, Sb and probably Sn. The higher mass loss measured for CZTS-OLA nanoparticles was consistent with the thermal decomposition of the bulky OLA molecules, which were not present at the surface of CZTS-$SbCl_3$ and CZTS-$(NH_4)_2S$ nanoparticles.

Figure 3c shows the ATR-FTIR spectra of dried CZTS-OLA, CZTS-$SbCl_3$ and CZTS-$(NH_4)_2S$ nanoparticles. The CZTS-OLA spectrum showed the C−H vibration modes in the high-frequency region (2800−3000 cm^{-1}) characteristic of OLA. This feature disappeared from the CZTS-$SbCl_3$ and CZTS-$(NH_4)_2S$ spectra.

The carbon left after annealing CZTS nanoparticles in a nitrogen atmosphere was measured by CHN quantitative elemental analysis. A 3% of carbon was obtained from the analysis of annealed CZTS-OLA nanoparticles. On the other hand, the carbon percentage measured from annealed CZTS-$SbCl_3$ and CZTS-$(NH_4)_2S$ nanoparticles was below the detection limit of our system: ~ 0.1%.

After organic ligand displacement and purification, CZTS-$SbCl_3$ and CZTS-$(NH_4)_2S$ nanoparticles were stable in solution during times long enough to allow their spray deposition.

A custom-made pulsed spray-deposition system was used to produce CZTS nanoparticle-based thin films from a 5 g/L CZTS solution in DMF. The system consisted of a heated sample holder and a nozzle that used nitrogen as the carrier gas. A computer-controlled electrovalve was used to create the spray pulses. The number of pulses, the pulse time, the time between pulses, and the substrate temperature were precisely controlled through a computer. The optimized process to produce homogeneous 2 μm-thick CZTS films was 40 cycles of 0.5 s pulses with a pulse-to-pulse time of 60 s, and a substrate temperature of 160 °C. For the crystallization analysis and to fabricate solar cells, CZTS nanoparticles were sprayed onto 2 × 2 cm^2 molybdenum-coated soda-lime glass substrates in air.

To produce solar cell grade layers, CZTS films were annealed for 60 min in a Se and Sn-rich atmosphere. A complete substitution of S by Se took place during selenization, transforming the precursor kesterite CZTS film (JCPDS 00-026-0575, Figure 4a) into kesterite CZTSe (JCPDS 01-070-

dx.doi.org/10.1021/ja4068639 | J. Am. Chem. Soc. XXXX, XXX, XXX−XXX

8930, Figure 4b). A partial selenization of the Mo bottom layer was also observed.

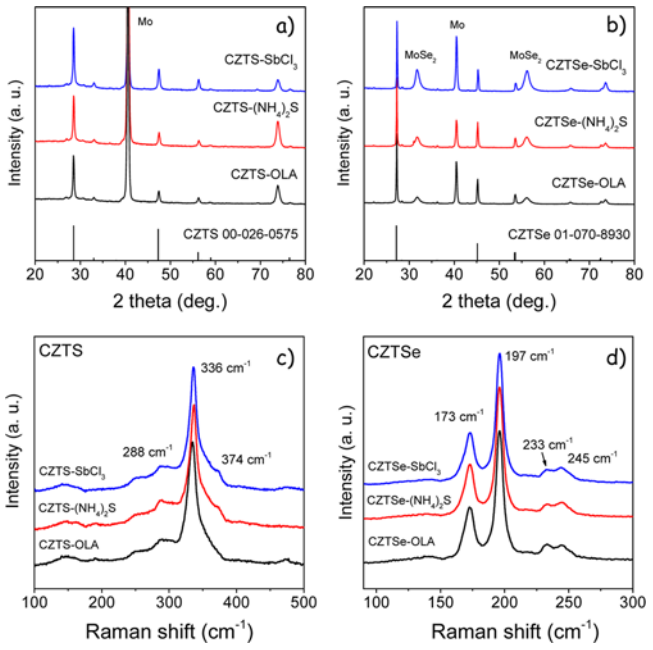

Figure 4. XRD patterns (a,b) and Raman spectra (c,d) of as-deposited (a,c) and 550 °C selenized (b,d) films prepared from CZTS-OLA, CZTS-$SbCl_3$ and CZTS-$(NH_4)_2S$ nanoparticles.

Raman spectra were measured with 514.5 nm excitation wavelength having a penetration depth of backscattered light below 100 nm (Figure 4c,d). The precursor film exhibited the typical Raman spectrum of CZTS nanocrystalline layers with broad peaks (fwhm of 13−14 cm^{-1}) at 288 and 336 cm^{-1} and a shoulder at 374 cm^{-1} corresponding to the two main A symmetry modes and likely to a B symmetry mode of the CZTS kesterite structure.[7,8] After annealing, and independently of the ligand, the crystalline quality of the films was largely improved (fwhm of main A peak = 5.5−6.5 cm^{-1}). CZTSe films showed a peak at 173 cm^{-1} which has been recently attributed to two A modes, the main A mode at 197 cm^{-1}, and two weaker peaks at around 233 cm^{-1} related to E/B symmetry modes.[7] No secondary phases were detected by either XRD or Raman measurements. Raman characterization using UV excitation (λ = 325 nm) also discarded the presence of ZnS.

Figure 5 shows cross-sectional SEM images of the precursor films and the films selenized at different temperatures, from 475 to 575 °C. Absorbers crystallized from CZTS-OLA and CZTS-$(NH_4)_2S$ films exhibited a typical bilayer structure formed by a bottom layer with fine grains and a top layer with larger crystals. Conversely, the absorbers crystallized from CZTS-$SbCl_3$ nanoparticles showed a single layer structure with large crystals covering from the substrate to the surface. Films obtained from CZTS-$SbCl_3$ nanoparticles systematically showed significantly larger crystal domain sizes than the ones produced from CZTS-$(NH_4)_2S$ and CZTS-OLA nanoparticles and even at temperatures below 500 °C relatively large crystal domains, in the micrometer range, were obtained.

Surprisingly, no Sb was detected after crystallization at temperatures above 500 °C. No peak shift or additional band was observed in the Raman spectra or the XRD patterns and no Sb was detected in the composition analysis performed by

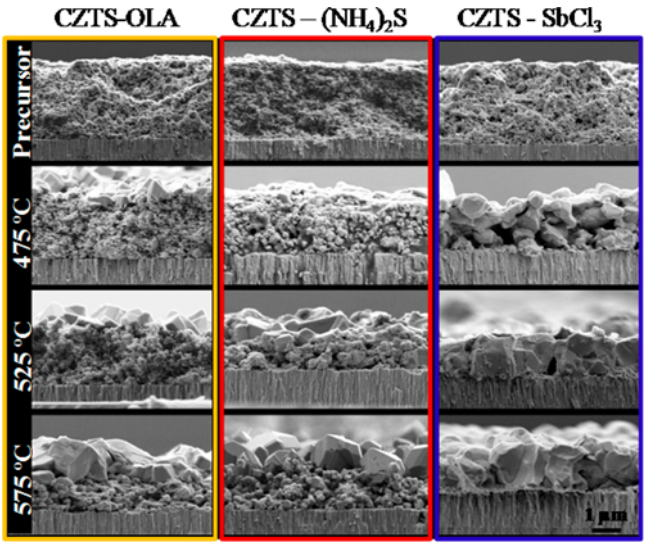

Figure 5. Cross-sectional SEM images of the CZTS precursor and CZTSe films prepared from CZTS-OLA, CZTS-$SbCl_3$ and CZTS-$(NH_4)_2S$ nanoparticles and annealed at temperatures from 475 to 575 °C.

EDX, ICP and XPS. EDX and ICP analyses showed the films to be copper-poor and zinc-rich, conserving the nanoparticles composition, both before (Cu/(Zn + Sn) = 0.85 and Zn/Sn = 1.09) and after crystallization (Cu/(Zn + Sn) = 0.81 and Zn/Sn = 1.01). Additionally, EDX showed an Sb content of about 5% for the CZTS-$SbCl_3$ thin films before selenization, but no Sb was detected on the CZTSe-$SbCl_3$ films after the heat treatment. ICP analyses showed an 8% by mass of Sb in the CZTS-$SbCl_3$ film before selenization, but no Sb after selenitzation. As-deposited CZTS-$SbCl_3$ films showed intense XPS Sb $3d_{5/2}$ and $3d_{3/2}$ peaks, corresponding to an atomic 20% Sb composition, but the crystallized CZTSe-$SbCl_3$ films showed no Sb-related peak (Figure SI3). Just an oxygen peak corresponding to a slight surface oxidation of the materials was detected by XPS in the crystallized but air exposed layers (Figure SI3). These results suggest that Sb did not incorporate to the bulk CZTSe crystals but it evaporated during the selenization process.

The use of Sb to promote crystal growth in Cu(In,Ga)Se_2 films was previously reported, but its role remains unclear.[9] We hypothesize that Sb incorporated to the CZTSe structure at the crystal surface locally forming a low melting point Sb-based chalcogenide. Various are the Sb-containing compounds with diamond-like phases that could be locally formed, e.g. Cu_3SbSe_4 with a melting temperatures of 425 °C[10] or even the quinary phase $CuZnSn_2Sb_3Se$,[11] although none of these were detected by XRD or Raman. Even in a substoichiometric ratio, the incorporation of Sb to the crystal structure could locally reduce the material's melting point, increasing its ionic mobility and its capacity for mass transfer and reorganization. We believe the decrease of the ion diffusion energy associated with Sb chemical incorporation ultimately promoted the diffusion-controlled crystallization process. As crystals domains grew, Sb was displaced to their surface where it accumulated. As crystallization proceeded, Sb evaporated and after 1 h at temperatures above 500 °C, no Sb was left within the CZTSe film.

Solar cells were fabricated from CZTS-$SbCl_3$ films deposited on 2 × 2 cm^2 soda-lime glass substrates with 800 nm of magnetron-sputtered Mo and selenized at 575 °C. A 60 nm

dx.doi.org/10.1021/ja4068639 | J. Am. Chem. Soc. XXXX, XXX, XXX−XXX

thick CdS buffer layer was deposited by chemical bath deposition. To complete the device, a 50 nm layer of i-ZnO and a 250 nm layer of In_2O_3:Sn were grown by pulsed DC-magnetron sputtering.[3] Finally, samples were scribed to 3 × 3 mm^2 cells. Figure 6a shows a characteristic $J-V$ curve obtained

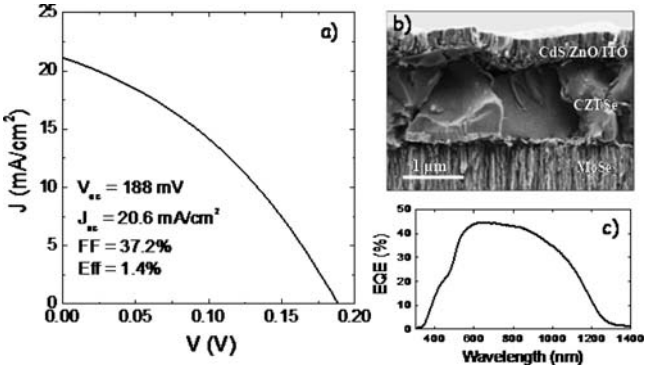

Figure 6. (a) Photovoltaic performance of a CZTSe solar cell prepared from the spray deposition of CZTS-$SbCl_3$ nanoparticles. (b) Cross-sectional SEM image of the device. (c) External quantum efficiency spectral response of the same device.

under AM1.5 illumination from one of the devices. In a first optimization, devices with relatively high current density of 20 mA/cm^2 were systematically achieved. However, rather low open circuit voltages close to 200 mV and fill factors below 40% were measured. This translated into power conversion efficiencies of 1.4% that although modest are encouraging for this low-cost and high-yield technology that allows the absorber material deposition in air and with the use of no hazardous chemicals, nor high vacuum equipment.

The device spectral response showed external quantum efficiencies up to 45% and allowed to calculate a band gap of 0.97 eV (Figure 6c). EQE showed a relatively high degree of recombination at the space charge region, suggesting that the improvement of the junction could help to increase efficiency. Indeed, we believe the moderate performances measured could be related with a poor CZTSe-CdS interface, which also reduced the device open circuit voltage and fill factor.

In summary, a ligand exchange strategy to remove organics, introduce antimony and render CZTS nanoparticles in solution and an automated pulsed spray deposition system to produce homogeneous and crack-free thin films were presented. Their combination allowed obtaining carbon-free thin films with controlled thickness and composition. The incorporation of Sb to the crystal surfaces locally reduced the material melting point promoting the diffusion-controlled crystallization. While thus-prepared CZTSe devices require optimization, our results demonstrate that the multistrategy approach presented here has a high potential to produce low-cost photovoltaic grade CZTSe layers.

■ ASSOCIATED CONTENT

Ⓢ Supporting Information

Synthesis and characterization details, complementary SEM micrographs, solar cell performance results and XPS spectra. This material is available free of charge via the Internet at http://pubs.acs.org.

■ AUTHOR INFORMATION

Corresponding Author

acabot@irec.cat

Notes

The authors declare no competing financial interest.

■ ACKNOWLEDGMENTS

This work was supported by the European Regional Development Funds and the Framework 7 program under project SCALENANO (FP7-NMP-ENERGY-2011-284486). E.S. thanks the Spanish government for the "Ramon y Cajal" fellowship (RYC-2011-09212).

■ REFERENCES

(1) (a) Todorov, T. K.; Reuter, K. B.; Mitzi, D. B. *Adv. Mater.* **2010**, *22*, E156. (b) Todorov, T. K.; Tang, J.; Bag, S.; Gunawan, O.; Gokmen, T.; Zhu, Y.; Mitzi, D. B. *Adv. Energy Mater.* **2013**, *3*, 34. (c) Guo, Q.; Ford, G. M.; Yang, W.-C.; Walker, B. C.; Stach, E. A.; Hillhouse, H. W.; Agrawal, R. *J. Am. Chem. Soc.* **2010**, *132*, 17384.

(2) (a) Shavel, A.; Arbiol, J.; Cabot, A. *J. Am. Chem. Soc.* **2010**, *132*, 4514. (b) Shavel, A.; Cadavid, D.; Ibáñez, M.; Carrete, A.; Cabot, A. *J. Am. Chem. Soc.* **2012**, *134*, 1438. (c) Ibáñez, M.; Zamani, R.; Li, W.; Shavel, A.; Arbiol, J.; Morante, J. R.; Cabot, A. *Cryst. Growth Des.* **2012**, *12*, 1085. (d) Ibáñez, M.; Zamani, R.; Lalonde, A.; Cadavid, D.; Li, W.; Shavel, A.; Arbiol, J.; Morante, J. R.; Gorsse, S.; Snyder, G. J.; Cabot, A. *J. Am. Chem. Soc.* **2012**, *134*, 4060. (e) Ibáñez, M.; Cadavid, D.; Zamani, R.; García-Castelló, N.; Izquierdo-Roca, V.; Li, W.; Fairbrother, A.; Prades, J. D.; Shavel, A.; Arbiol, J.; Pérez-Rodríguez, A.; Morante, J. R.; Cabot, A. *Chem. Mater.* **2012**, *24*, 562. (f) Singh, A.; Geaney, H.; Laffir, F.; Ryan, K. M. *J. Am. Chem. Soc.* **2012**, *134*, 2910. (g) Aldakov, D.; Lefrancois, A.; Reiss, P. *J. Mater. Chem. C* **2013**, *1*, 3756.

(3) Fairbrother, A.; García-Hemme, E.; Izquierdo-Roca, V.; Fontané, X.; Pulgarín-Agudelo, F. A.; Vigil-Galán, O.; Pérez-Rodríguez, A.; Saucedo, E. J. *Am. Chem. Soc.* **2012**, *134*, 8018.

(4) Ibáñez, M.; Zamani, R.; Li, W.; Cadavid, D.; Gorsse, S.; Katcho, N. A.; Shavel, A.; López, A. M.; Morante, J. R.; Arbiol, J.; Cabot, A. *Chem. Mater.* **2012**, *24*, 4615.

(5) (a) Kovalenko, M. V.; Scheele, M.; Talapin, D. V. *Science* **2009**, *324*, 1417. (b) Nag, A.; Kovalenko, M. V.; Lee, J.-S.; Liu, W.; Spokoyny, B.; Talapin, D. V. *J. Am. Chem. Soc.* **2011**, *133*, 10612.

(6) Cadavid, D.; Ibáñez, M.; Shavel, A.; Dura, O. J.; Lopez de la Torre, M. A.; Cabot, A. *J. Mater. Chem. A* **2013**, *1*, 4864.

(7) (a) Khare, A.; Himmetoglu, B.; Johnson, M.; Norris, D. J.; Cococcioni, M.; Aydil, E. S. *J. Appl. Phys.* **2012**, *111*, 083707. (b) Gürel, T.; Sevik, C.; Çağın, T. *Phys. Rev. B* **2011**, *84*, 205201. (c) Fontané, X.; Izquierdo-Roca, V.; Saucedo, E.; Schorr, S.; Yukhymchuk, V. O.; Valakh, M. Y.; Pérez-Rodríguez, A.; Morante, J. R. *J. Alloys Compd.* **2012**, *539*, 190. (d) Fontané, X.; Calvo-Barrio, L.; Izquierdo-Roca, V.; Saucedo, E.; Pérez-Rodriguez, A.; Morante, J. R.; Berg, D. M.; Dale, P. J.; Siebentritt, S. *Appl. Phys. Lett.* **2011**, *98*, 181905. (e) Djemour, R.; Redinger, A.; Mousel, M.; Gütay, L.; Fontané, X.; Izuierdo-Roca, V.; Pérez-Rodríguez, A.; Siebentritt, S. *Opt. Express* **2013**, *21*, A695.

(8) Espindola-Rodriguez, M.; Placidi, M.; Vigil-Galán, O.; Izquierdo-Roca, V.; Fontané, X.; Fairbrother, A.; Sylla, D.; Saucedo, E.; Pérez-Rodríguez, A. *Thin Solid Films* **2013**, *535*, 67.

(9) (a) Zhang, S.; Wu, L.; Yue, R.; Yan, Z.; Zhan, H.; Xiang, Y. *Thin Solid Films* **2013**, *527*, 137. (b) Yuan, M.; Mitzi, D. B.; Gunawan, O.; Kellock, A. J.; Chey, S. J.; Deline, V. R. *Thin Solid Films* **2010**, *519*, 852. (c) Yuan, M.; Mitzi, D. B.; Liu, W.; Kellock, A. J.; Chey, S. J.; Deline, V. R. *Chem. Mater.* **2010**, *22*, 285.

(10) Berger, L. I.; Prochukhan, V. D. *Ternary Diamond-like Semiconductors*; Consultants Bureau: New York, 1969, 64.

(11) Pamplin, B. *Prog. Cryst. Growth Charact.* **1981**, 3.